SAPIENZA
UNIVERSITÀ DI ROMA

Experimental characterization of tritium extraction systems and tritium anti-permeation barriers in heavy liquid metal systems

Facoltà di Ingegneria Civile e Industriale

Energia e Ambiente - Scuola di Dottorato in Scienze e Tecnologie per l'Innovazione Industriale (XXXV cycle)

Francesca Papa

ID number 1647229

Advisors

Prof. Gianfranco Caruso

Dr. Marco Utili

Dr. Alessandro Tassone

Academic Year January 2023

Thesis defended on 25th January 2023
in front of a Board of Examiners composed by:

Prof. Fulvio Palmieri (chairman)

Prof. Lucia Fontana

Prof. Marco Sabatini

Experimental characterization of tritium extraction systems and tritium anti-permeation barriers in heavy liquid metal systems

Sapienza University of Rome

This thesis has been typeset by LaTeX and the Sapthesis class.

Version: 8th of January 2023

Author's email: f.papa@uniroma1.it

To my betrothed

Abstract

This work lies within the framework of the development of advanced nuclear reactors, dealing with the research on tritium technologies, such as extraction systems for the Water Cooled Lithium-Lead Breeding Blanket (WCLL BB) of the EU DEMO fusion reactor and anti-permeation coatings for IV generation fission Lead-cooled Fast Reactors (LFR). On the first topic, the aims of this thesis are to provide the first characterization of the Permeator Against Vacuum (PAV) technology and to contribute to the research on the Gas-Liquid Contactor (GLC). Instead, the characterization at ALFRED LFR relevant conditions of the Pulsed Laser Deposition (PLD) coatings is the aim of the second part of the thesis.

The two parts of the thesis are joined together by the common theoretical background of tritium transport.

The first part took advantage of the experimental facility TRIEX-II, located at ENEA Brasimone R.C., which has been refurbished and intensively operated to contribute to the characterization of the PAV and GLC technologies.

The PAV has been often considered as the reference technology to extract tritium from LiPb, but it has never been tested in relevant conditions, nor a sizeable mock-up has ever been completed before. In this thesis, the engineering design and fabrication of a niobium-based PAV are shown, with particular attention paid on the manufacturing processes and on the selected equipment. The mock-up has been integrated in TRIEX-II and tested at different hydrogen partial pressures and LiPb temperatures, demonstrating that a PAV can be manufactured and operated at relevant conditions. The experiments showed that the permeated flux was in the order of 10^{-9} mol/s at 350 °C and increased, at 450 °C, to about 10^{-8} mol/s.

The activity on PAV is complemented by data on the compatibility of niobium in flowing LiPb, obtained by exposing samples at 0.5 m/s and 500 °C in IELLLO facility, also located at ENEA Brasimone R.C., for about 4000 hours. Vanadium, the other PAV candidate material, was also exposed in the same campaign. The samples of both materials withstood the aggressive environment but a tendency was noted to form ternary compounds with nickel, already dissolved in LiPb.

A complementary experimental campaign aimed at providing new data on the GLC operation and showed low extraction efficiencies, caused by the strong corrosion of the packings. The lessons learnt in this campaign on instrumentation and packings were useful for the PAV experiments and are being used to prepare a new GLC campaign that will be performed during Fall 2022.

The second part of the thesis deals with the fusion-fission cross-cutting subject of alumina coatings, which have the double task of reducing corrosion of structural materials and minimizing tritium permeation towards the coolant in the WCLL BB and in the primary loop of ALFRED lead fast reactor. In this field, the main achievement has been the design and construction of an innovative experimental apparatus, named APRIL, also located at ENEA Brasimone R.C., that is capable of testing permeation from a gas phase towards water in relevant conditions for fusion and fission reactors. This facility has been used to measure the Permeation Reduction Factor (PRF) of 3 µm alumina coatings made by PLD with deuterium concentration of 0.5% and water at ALFRED conditions. The evaluated PRF is

about 13.5.

A second activity on coatings has been devoted to test their effectiveness in reducing the corrosion rate of EUROFER and their resistance in flowing LiPb by exposing samples in the same IELLLO campaign mentioned above. While PLD-made coatings protected the EUROFER samples and resisted to the LiPb corrosive attack, those made by Atomic Layer Deposition showed a tendency to detach from the substrate, leaving EUROFER exposed to the LiPb flow. Finally, both coatings revealed a grainy appearance related to the formation of LiAl-oxides.

Sommario

Questa tesi si colloca nel contesto dello sviluppo di reattori nucleari avanzati, in particolare nell'ambito della ricerca sulle tecnologie del trizio, come i sistemi di estrazione per il Water Cooled Lithium-Lead Breeding Blanket (WCLL BB) del reattore a fusione EU DEMO e le barriere anti-permeazione per i reattori a fissione di IV generazione Lead-cooled Fast Reactors (LFR). Riguardo il primo campo, gli obiettivi di questa tesi sono di fornire la prima caratterizzazione della tecnologia Permeator Against Vacuum (PAV) e di contribuire alla ricerca sul Gas-Liquid Contactor (GLC). Invece, la caratterizzazione in condizioni rilevanti per ALFRED LFR dei coatings realizzati tramite Pulsed Laser Deposition (PLD) costituisce l'obiettivo della seconda parte di tesi.

Le due parti di questa tesi sono collegate dalle fondamenta teoriche in comune riguardanti il trasporto del trizio.

La prima parte sfrutta l'impianto sperimentale TRIEX-II, installato presso il C.R. ENEA Brasimone, a cui è stata fatta manutenzione e che è stato successivamente esercito per testare le tecnologie del GLC e del PAV.

Il PAV è stato spesso considerato come la tecnologia di riferimento per estrarre il trizio dal PbLi, ma non era ancora mai stato realizzato né testato in condizioni rilevanti per il reattore DEMO europeo. La progettazione ingegneristica e la realizzazione di un primo PAV con tubi in niobio sono illustrate in questa tesi, ponendo particolare attenzione ai processi di fabbricazione e alla strumentazione selezionata. Il mock-up è stato integrato in TRIEX-II e caratterizzato a diverse pressioni parziali dell'idrogeno e temperature del PbLi, andando a dimostrare che un PAV può effettivamente essere realizzato ed esercito in condizioni rilevanti. Durante gli esperimenti è stato misurato un flusso permeato dell'ordine di 10^{-9} mol/s a 350 °C e di circa 10^{-8} mol/s a 450 °C.

L'attività sulla caratterizzazione del PAV è stata integrata da una campagna sperimentale sulla compatibilità del niobio in PbLi fluente, effettuata esponendo dei campioni a 500 °C e 0.5 m/s per circa 4000 ore nell'impianto IELLLO. Nella stessa campagna sperimentale sono stati caratterizzati anche dei provini di vanadio, l'altro materiale candidato come membrana per il PAV. Entrambi i materiali hanno resistito all'ambiente aggressivo ma si è notata una tendenza alla formazione di composti ternari con il nichel che era già dissolto nel PbLi, essendo le tubazioni nell'impianto in acciaio inossidabile.

Il GLC, invece, è stato caratterizzato in un'altra campagna e ha mostrato basse efficienze di estrazione, che si è scoperto successivamente essere state causate dalla severa corrosione dei packings. Gli insegnamenti tratti da questa esperienza sull'uso della strumentazione e sui packings si sono rivelati utili per gli esperimenti sul PAV e stanno venendo attualmente utilizzati per preparare una nuova campagna sul GLC, che verrà svolta nell'autunno 2022.

La seconda parte della tesi riguarda un argomento trasversale fra fusione e fissione, quello dei rivestimenti in allumina che hanno il duplice compito di ridurre la corrosione dei materiali strutturali e di minimizzare la permeazione del trizio verso il refrigerante nel WCLL BB e nel primario del reattore veloce ALFRED. Il principale risultato in quest'ambito è stata la progettazione e la costruzione di un

impianto sperimentale innovativo, chiamato APRIL, in cui è possibile caratterizzare la permeazione dalla fase gas all'acqua, a temperature e pressioni rilevanti sia per la fusione che per la fissione. APRIL è stata usata per la prima volta per misurare il Permeation Reduction Factor (PRF) di un rivestimento di allumina spesso 3 µm realizzato tramite PLD con una concentrazione di deuterio di 0.5% e acqua alle condizioni dello scambiatore di calore di ALFRED. Il PRF così valutato è stato di circa 13.5.

Anche questa attività è stata integrata dalla campagna di IELLLO per la valutazione della capacità del rivestimento di ridurre anche il rateo dil corrosione dell'EUROFER e la sua resistenza in PbLi fluente. Mentre i rivestimenti fatti con PLD hanno protetto l'acciaio e hanno resistito all'attacco del PbLi, quelli realizzati tramite la tecnica dell'Atomic Layer Deposition hanno mostrato una tendenza a distaccarsi dal sostrato, esponendo l'EUROFER all'azione del PbLi. Entrambi i rivestimenti hanno rivelato una superficie granulosa, che è stata motivata con la formazione di ossidi misti litio-alluminio.

Contents

List of Figures

List of Tables

Part I

Introduction

Chapter 1

Research framework and motivation

Hydrogen is the lightest chemical element and it has 3 isotopes: protium, deuterium and tritium. The first one is the most common isotope in nature, with one proton, one electron, and no neutrons; while deuterium has a natural abundance of 0.001%-0.028%. Tritium, the radioactive isotope of hydrogen, has several peculiar characteristics that make it worth of special attention when dealing with safety in nuclear facilities. It decays emitting a beta particle with a maximum energy of 18.6 keV and with a half-life of about 12.3 years. It is colorless, odorless and tasteless.

It chemically behaves almost as protium, even if the tritium reaction rates are slightly different from the protium ones because of the different atomic masses, and its decay energy can provide the activation energy for some reactions that would not occur otherwise. Tritium forms the same, very common and very frequent in nature, compounds than protium does. It is extremely difficult to confine it and it has several environmental pathways to the human body, by swapping with hydrogen atoms in the biosphere and hydrosphere. Once in the body, it behaves very differently depending on the intake form: if inhaled in gaseous phase, it is not absorbed apart from a small portion that is dissolved in the blood and exhaled after some minutes; instead, if ingested or absorbed through the skin as tritiated water, it is retained in the body with a biological half-life of about 10 days and, therefore, it represents a much bigger hazard to human life [1].

Tritium Derived Air Concentration (DAC) * is higher compared with that of other isotopes that represent common radiological hazards in the nuclear industry: indeed, the DAC of tritium is $9 \cdot 10^9$ Bq/m^3 in gaseous form and $7 \cdot 10^5$ Bq/m^3 as tritiated water while, for example, that of iodine-131 is $5 \cdot 10^2$ Bq/m^3, caesium-137 is $3 \cdot 10^3$ Bq/m^3 and polonium-210 is $9 \cdot 10^0$ Bq/m^3 [2]. However, the unique combination of the above-mentioned properties has to be considered with DAC parameter for tritium for the deployment of fusion plants and fourth generation fission reactors alike.

Focusing for the moment on fusion device, tritium represents one of the two fuels

*The DAC is defined in the ICRP Publication 60 (ICRP, 1991b, paragraph S30) as: "Derived air concentration equals the annual limit on intake, ALI, (of a radionuclide) divided by the volume of air inhaled by a Reference Person in a working year (i.e., 2.2×103 m^3). The unit of DAC is Bq/m^3.

of the reaction and, therefore, it has to be adequately produced in the Breeding Blanket (BB) and used in the plasma of the tokamak reactor. On the other hand, tritium is an undesired byproduct in fission reactors, where of course the amount of produced tritium is kept as low as reasonably achievable. Therefore, a precise definition of tritium inventory is critical to the safety demonstration of both types of reactors, but it is also a challenging matter because of the uncertainties in the retention, transport and outgassing properties in coolants, breeders and structural materials (e.g., Sieverts' constant, diffusivity, ...). Furthermore, the anti-permeation barriers and the technologies adopted by fusion reactors to remove tritium from the breeder and to handle it in the fuel cycle have a low degree of maturity, but may have a relevant impact in the definition of tritium inventories.

This chapter aims at introducing the fusion and IV Generation fission reactors and explains the structure, the motivation and the objectives of the thesis.

1.1 Advanced nuclear reactors

The research in the field of nuclear energy has been focused along two main lines: the successful exploitation of the fusion reaction, to recreate, in a controlled environment, the same conditions that power the Sun and the other stars [3] and the development of a new generation of fission reactors, generally known as the fourth generation, or GEN-IV [4].

The fusion reaction is a process that allows two nuclei to collide and join between them to create a heavier nucleus, releasing energy and some particles. It is a reaction characteristic of small nuclei, such as the hydrogen isotopes. There are many nuclear fusion reactions, however the reaction more suitable for a fusion reactor is the deuterium-tritium one. The reason behind this choice is that this reaction has the highest cross section σ at the lowest temperature (i.e. energy, below 100 KeV), as shown in Figure 1.1. The so-called D-T reaction is:

$$\mathrm{D} + \mathrm{T} = {}^{4}\mathrm{He} + n + 17.586 MeV \tag{1.1}$$

This reaction uses tritium, the heavy isotope of hydrogen containing two neutrons in the nucleus. It is radioactive and decays in ^{3}He by releasing a pair composed of an electron and an antineutrino together with a release of energy (beta decay):

$$T \rightarrow {}^{3}\mathrm{He} + \beta^{-} + \overline{\nu} + 18.6 keV \tag{1.2}$$

where $\overline{\nu}$ is the symbol of the antineutrino.

Given its short half-life (12.3 years), tritium is present in nature only in traces, originating from the transmutation of nitrogen due to interaction with so-called cosmic rays [6]. Moreover, being tritium radioactive and so hazardous to human health, it has to be contained during all the phases of the fuel cycle. Tritium chemical and physical properties make it particularly dangerous and difficult to be handled or retained. Indeed, tritium atoms are chemically equivalent to hydrogen, meaning that tritium can substitute it in molecules, and equally chemically reactive by donating or accepting an electron to form chemical bonds [1]. This high tritium reactivity, together with its light weight and small size, allows it to have the fastest diffusion

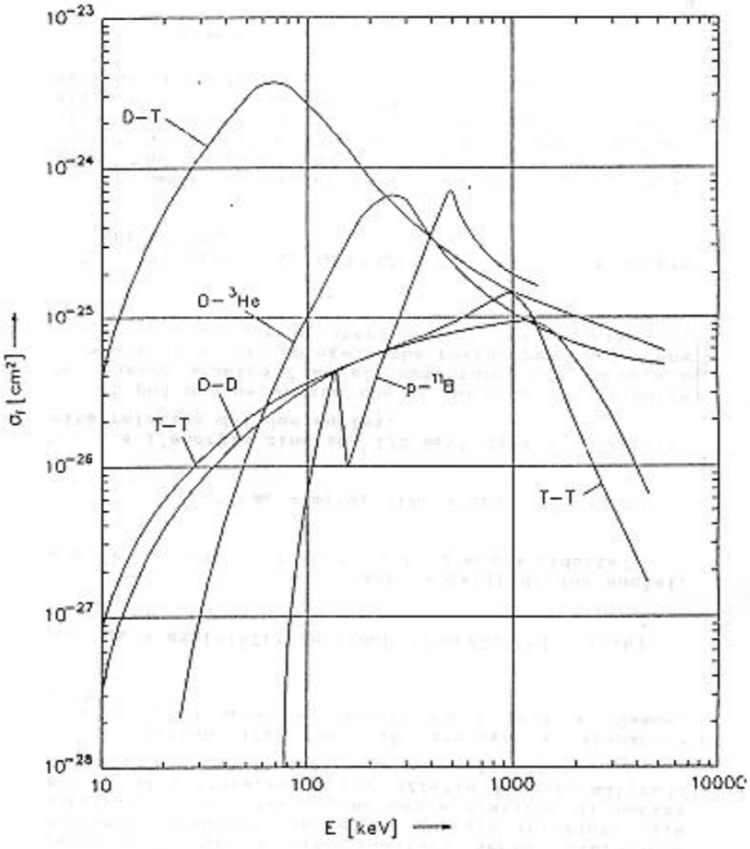

Figure 1.1. Fusion reaction cross-section (taken from [5])

rate through solid materials. Materials permeability to tritium is strictly related to their lattice structure, as well as to the presence of lattice defects, and to hydrogen reactivity with them.

Emitting low energy beta particles (maximum 18.6 keV), tritium is dangerous only if inhaled or ingested, in fact, tritium beta particles cannot even penetrate the dead skin layer which is able to stop particles up to 70 keV. If ingested, 1 mg of tritium would lead to a dose of about 15 mSv.

In the fusion field, the large amount of tritium is required as fuel in the future power-producing tokamak reactor so, due to the small amount in nature, it will be produced in situ. To this end, one may exploit lithium transmutation with fusion neutrons:

$$^{6}\mathrm{Li} + n \rightarrow {}^{4}\mathrm{He} + T + 4.86MeV \tag{1.3}$$

$$^{7}\mathrm{Li} + n \rightarrow {}^{4}\mathrm{He} + T + n^{'} - 2.5MeV \tag{1.4}$$

The former reaction channel has a much higher cross-section and can happen with any neutron energy, while the latter has a 2.5 MeV threshold.

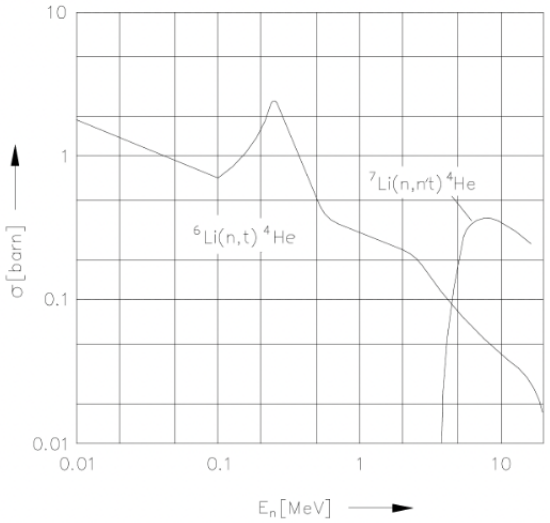

Figure 1.2. Lithium cross-sections for tritium generating reactions

Being the calculated tritium consumption in fusion remarkable (about 0.4 kg/d for EU DEMO reactor [6]) it is going to be necessary to carefully design the reactor to achieve a satisfactory tritium generation rate. To this end, lithium is enriched up to 90% in ^{6}Li [7]. For the same purpose, lithium is mixed with neutron multipliers, such as lead or beryllium. The material that is used to produce tritium is named breeder and it is contained in the Breeding Blanket (BB), a component that surrounds the plasma chamber. BB concepts are usually named after their coolant and breeder.

This thesis is conceived in support to the development of the Water-Cooled Lithium Lead Breeding Blanket (WCLL BB) [8], which uses the eutectic liquid alloy of lead and enriched lithium as breeder (LiPb). The eutectic concentration (15.7%

at. of Li [9]) has been chosen as it has the lowest melting point (about 235 °C [10]) in the binary phase diagram and as a compromise between a low lithium chemical activity and a lithium content high enough for tritium breeding. Once that tritium is generated in the breeder, it has to be extracted and stored to be later used as fuel in the reactor.

Tritium extraction from LiPb occurs in a component, the Tritium Extraction Unit (TEU), which is part of a bigger system, the WCLL TER (Tritium Extraction and Removal). The WCLL TER has several tasks in addition to the tritium extraction including ensuring the LiPb circulation through the BB and purifying the alloy from impurities such as:

- helium [11], a by-product of the reaction that breeds tritium;
- corrosion products [12], for example iron, chromium and manganese removed from structural materials by the corrosive-erosive action of LiPb;
- activated products, mainly thallium, mercury and polonium, generated by the transmutation of lead under neutron irradiation.

Regarding the tritium extraction, three technologies are currently under investigation for the WCLL TER [13] within EUROfusion (the European consortium that supports and funds research activities towards the development of EU DEMO reactor [14]): the Gas-Liquid Contactor (GLC) [15], the Permeator Against Vacuum (PAV) [16] and the Liquid-Vacuum Contactor (LVC) (in the Free Surface or Vacuum Sieve Tray (VST) [17] configuration). The first and the latter of these technologies rely on the direct tritium transport across an interface, between LiPb and a "stripping" gas, in the GLC, or between LiPb and vacuum, for the case of LVC. Instead, the Permeator Against Vacuum uses, between LiPb and vacuum, membranes made of a material with high permeability to tritium, such as iron [18], niobium, tantalum or vanadium [19]. In this thesis, the first Permeator Against Vacuum was manufactured, installed and tested.

The characteristics of tritium, as said before, imply that tritium can easily permeate from the breeder into the BB structural material, coolant or directly into the tokamak building. Hampering this process is necessary both to avoid radioactive contamination and to limit the tritium losses, thus improving the self-sustainability of the machine. One of the main technological solutions currently being studied for this purpose is the use of anti-permeation barriers, commonly known as coatings [20]. These are thin layers deposited on components and pipes that are made of materials that are characterized by low tritium permeability. Alumina (Al_2O_3) is the coating material being under investigation within EUROfusion for a prospective deployment in the WCLL BB [21]. The Permeation Reduction Factor (PRF) is used to characterize the performance of anti-permeation coatings and is defined as the flux that permeates without the coating compared with the flux that is going to permeate with a coating applied:

$$PRF = \frac{i_{without\ coating}}{i_{with\ coating}} \tag{1.5}$$

Tritium is also generated in fission reactors due to the ternary fissions and the neutron interaction with elements such as lithium and boron. Following the ternary

fissions in the reactor fuel and the neutron interaction with the boron carbide rods, generation of tritium is expected in some of the fourth generation reactors under investigation. The so-called fourth generation relies on four pillars to progress with respect to the reactors that are currently on the market [22]:

- safety and reliability;
- proliferation resistance and physical protection;
- economic competitiveness;
- sustainability.

A total of six reactor concepts are under development around the world to achieve these four goals: Sodium-cooled Fast Reactors (SFR), Lead-cooled Fast Reactors (LFR), Gas-cooled Fast Reactors (GFR), Molten Salt Reactors (MSR), SuperCritical Water Reactors (SCWR) and Very High Temperature Reactors (VHTR). At least three of them plan to take advantage of the fast neutron spectrum to meet the required criteria, but also some designs of MSR, SCWR and VHTR adopt a fast spectrum [23], even though thermal-spectrum designs exist as well. Fast spectrum reactors have a number of advantages over thermal ones, among which the possibility of a more effective utilization of uranium resources, by breeding ^{239}Pu from ^{238}U (the most abundant but not fissile isotope of uranium) and then using it to produce energy, and the possibility to convert the minor actinides and other long-lived radioisotopes to short lived ones, thus reducing or eliminating *tout court* the need for geological disposal [24].

However, in a fast reactor, tritium can be generated by ternary thermal fissions of ^{235}U and, to a larger extent, ^{239}Pu (about 0.2% of all the fissions are ternary [25]), but also from fast fissions of fertile nuclides. The most common reaction of boron with neutrons generates helium and ^{7}Li. However, there is also the possibility that a neutron capture reaction forms tritium, above 1.2 MeV [26]:

$$^{10}\mathrm{B} + n \rightarrow 2\,^{4}\mathrm{He} + T \tag{1.6}$$

Moreover, the lithium from the main reaction of boron can build up at high burnup and generate additional tritium by means of the chain of reactions:

$$^{10}\mathrm{B} + n \rightarrow {}^{4}\mathrm{He} + {}^{7}\mathrm{Li} \tag{1.7}$$

$$^{7}\mathrm{Li} + n \rightarrow {}^{4}\mathrm{He} + T + n' \tag{1.8}$$

The research of this thesis is focused on the tritium issue for the LFR. It is important to confine tritium in the lead pool, not allowing it to permeate towards the Primary Heat Transfer System, the reactors water cooling loops. For this reason, also in the fission field, alumina coatings are under development within the activities devoted to the development of ALFRED reactor [27]. ALFRED (Advanced Lead-cooled Fast Reactor European Demonstrator) is a European LFR developed by Ansaldo Nucleare, ENEA and RATEN-ICN with a nominal thermal power of 300 MW and lead temperatures in the range 390-520°C. ALFRED design and

related R&D activities are mainly supported by the FALCON (Fostering ALfred CONstruction) consortium, but fission-fusion cross-cutting activities found space also in different projects and consortia. This is the case of tritium-related research efforts which are the subjects of the TRANSAT (TRANSversal Actions for Tritium) project [28].

Within ALFRED, the use of alumina coatings is currently mainly envisaged to withstand the harsh corrosive environment and Pulsed Laser Deposition (PLD) is the reference deposition technology for every surface of the core [29], at least during the final reactor stage. Indeed, the deployment of ALFRED foresees a total of 4 stages, from stage 0 to stage 3, in which the power, and thus the temperatures, is gradually increased. This approach has been conceived to gain operational experience and validate technologies and design [27].

However, as explained in the above paragraph, PLD-made alumina coatings also have the possibility to be used to reduce tritium permeation, enhancing the safety of the reactor without the need for a separate technology or a dedicated system. This aspect has been investigated within the TRANSAT project.

1.2 Document outline

The thesis is organized in four parts: Introduction, Tritium Extraction Systems, Anti-permeation Coatings and Compatibility of Materials with LiPb and Final remarks.

The first part is divided in three chapters: the first one, that you are reading, introduces the research motivation and the context in which the work is set, the second one explains the basis of the tritium transport theory, fundamental for understanding the topic (Chapter 2), and the third one presents the main technologies studied during the PhD (Chapter 3).

The second part is dedicated to tritium extraction technologies for fusion reactor. Firstly, the experimental facility TRIEX-II (Chapter 4), used to characterize the tritium extraction systems, is introduced; then, its test sections are described and analyzed: PAV-ONE, the first Permeator Against Vacuum (PAV) mock-up with niobium membrane to be manufactured, installed and tested (Chapter 5); and the Gas-Liquid Contactor (GLC) mock-up, in 1:1 scale of ITER component (Chapter 6).

The third part of the document is dedicated to the activities on the characterization of alumina PLD coatings from the point of view of tritium permeation reduction and to the activities carried out on materials compatibility with LiPb. Firstly, a section describes the design and manufacturing of a new facility, named APRIL (Section 7.1), and then the experimental campaign at ALFRED operative conditions is illustrated (Section 7.2). Afterwards, the results of an experimental campaign with IELLLO facility are described. The campaign was devoted to study the behavior in flowing high-temperature LiPb of niobium and vanadium, two materials candidate as membranes of the Permeator Against Vacuum technology (Section 8.2), of EUROFER samples coated with alumina by PLD and ALD (Atomic Layer Deposition) techniques, two of the deposition techniques most studied within EUROfusion (Section 8.4), and of P22 ferritic steel, currently the reference material for the WCLL TER (Section 8.3).

At the end, a conclusive chapter resumes the main outcomes of the PhD thesis and illustrates the future perspectives of the work (Chapter 9).

1.3 Motivation and aims

This thesis has followed two main research lines, tritium extraction and anti-permeation barriers, and consequently has two slightly different, but connected, aims. The first one is to support the development of tritium extraction technologies from LiPb, with a particular effort on the PAV technology, but also a contribution to the GLC. The second aim is to contribute to the research on anti-permeation/anti-corrosion barriers, by performing experiments on tritium permeation from gas phase towards water.

The tritium extraction system is likely the most important component of the WCLL TER, having the task to make LiPb-solubilized tritium available for the fuel cycle. The performances of this system will be a key factor in the choice of the driver BB, i.e.the main BB concept that will be adopted for EU DEMO reactor, between the WCLL and the Helium Cooled Pebble Bed (HCPB). For this reason, a large effort is underway within EUROfusion Framework Programme 9 (FP9) on the characterization of the extraction technologies and on the measurement of fundamental properties required for the modelling and for the design of these systems (the Sieverts' constant of tritium in LiPb, the tritium transport parameters of many functional materials, such as niobium and vanadium, the trapping sites and trapping densities). Three technologies are currently under investigation within FP9: the GLC, the PAV and the Liquid-Vacuum Contactor (LVC), a component where the flowing LiPb surface is directly exposed at vacuum, without membrane.

In 2019, ENEA Brasimone R.C. designed and built a facility, named TRIEX-II (TRItium EXtraction), to test GLC and PAV mock-ups. The first activity that I worked on during the PhD was dedicated to perform the engineering design of the PAV mock-up and to the experimental activities on this facility. These activities started with the refurbishment of the facility, with a special focus on the Hydrogen Permeation Sensors that are among the most important instruments to ensure a good outcome to the tests. This was followed by the experimental campaign on the GLC mock-up, developed into different phases:

1. design of the experiments,
2. definition of the test procedure,
3. commissioning tests to check the correct operation of the instruments and components,
4. execution of the tests,
5. data analysis and uncertainty analysis.

After the campaign was concluded, the focus was shifted towards the PAV mock-up, even though a part of the activity was developed in parallel to the GLC campaign. The research on PAV can be divided into:

1. engineering design, with particular attention to the integration in the facility and the required interfaces,
2. selection of instrumentation and equipment and support to the manufacturing of the mock-up,
3. support to the installation of the mock-up in TRIEX-II,
4. design of the experiments and definition of the test procedure,
5. commissioning tests to check the correct operation of the instruments and components,
6. execution of the tests, data analysis and uncertainty analysis.

Regarding the second objective of the thesis, the development of anti-permeation coatings is deemed as a fundamental milestone towards the possibility to achieve sustainable energy production from fusion nuclear reactors and reduce tritium wastes in fission reactors. As a matter of fact, without high performance tritium barriers, tritium would permeate outside of the primary loop and would be a risks for the operators and for the environment.

Indeed, coatings will reduce the tritium permeation through the structural material of nuclear power plants in order to avoid high tritium concentrations in the water and in the work areas. Moreover, the permeation barriers allow to minimize tritiated wastes and possible structural material embrittlement. Therefore, chemically inert coatings are needed to reduce the permeation and alumina is one of the most promising materials to be used as a permeation barrier.

In addition, alumina coatings are conceived as a way to reduce corrosion of the structural materials, enhancing the durability of the reactor components and the mobilization of activated materials.

Alumina coatings can be deposited on surfaces by many manufacturing techniques. In order to select the most suitable one, a list of high-level requirements has been drafted:

- to deposit the alumina coating on the structural material in the required metallurgical state;
- to produce coatings with acceptable performances in terms of PRF (Permeation Reduction Factor);
- compatibility of the technique with the component geometry, also considering the dimensions and the fabrication sequence;
- to provide a consistent lifetime with that of the component to protect.

As a consequence, the most suitable coating technology deeply depends on the type of application. For WCLL BB and LFR, the most promising technology is the Pulsed Laser Deposition (PLD).

This thesis aimed at supporting this field of research with the ambition of being relevant for both fission and fusion because the facility that was designed and

manufactured at ENEA Brasimone R.C., called APRIL (Alumina-coating for tritium Permeation Reduction for Innovative LFR), will allow to characterize one of the reference coating technologies for DEMO and ALFRED reactors. Moreover, and here stands the innovative nature of this project, the APRIL facility will allow to test for the first time these coatings in relevant operative conditions. From a recent literature review, even though some studies do exist that tested coating technologies with relevant parameters, no coating technique has still been simultaneously tested at relevant operative conditions (temperature, deuterium partial pressure), and considering relevant geometries (diameter, shape, thickness etc.) and media (water, steel and alumina).

Therefore, the results of this project are expected to have a positive impact in the tritium permeation barrier research field by providing the researchers an unique and pioneering facility that will hopefully allow to select the most suitable coating techniques for both the DEMO-WCLL BB concept and ALFRED LFR.

The activity on APRIL was divided into the following phases:

1. in-depth analysis of the state of the art on the subjects involved in this activity,
2. definition of the operating conditions, the test matrix and the test procedure,
3. definition of the facility layout, the needed instrumentation and components and realization of the preliminary P&ID of the facility,
4. preliminary thermo-mechanical analysis of the thicknesses of the pipes and of the chamber,
5. integration of the instrumentation and components and final P&ID of the facility,
6. support to the facility installation and execution of the commissioning tests,
7. experimental campaign.

The activity on coatings is also complemented by the investigation of coatings-LiPb compatibility performed with a campaign in IELLLO facility at ENEA Brasimone R.C.. The exposure of coated EUROFER samples to flowing LiPb was important to characterize the alumina corrosion behavior in dynamic conditions, i.e. the resistance of the coatings and their capability to protect the substrate material, as previous tests on PLD and ALD coatings were only performed in stagnant conditions.

The same experimental campaign tested also the corrosion behavior of niobium, vanadium and P22 ferritic steel. Niobium and vanadium are the two most important candidates as membrane materials for the PAV and their compatibility with LiPb was only characterized in static conditions, so far. Instead, P22 ferritic steel is considered the reference material for the WCLL TER pipework but no data were available on its resistance to high temperature flowing LiPb before this thesis. Moreover, these activities nicely complement the work on PAV, giving a well-rounded structure to the thesis.

The activity on IELLLO experimental campaign on materials compatibility included the support to the sample and test section design, the support to the

installation of the test section, the campaign execution and the support to the post-test analyses.

Chapter 2

Elements of tritium transport theory

This chapter aims to present a basic knowledge of tritium transport phenomena that will help to better comprehend the results presented in this thesis. In this chapter, the term "hydrogen" is used to talk generally about the "hydrogen isotopes", while "protium" is used to refer to the lightest one. This chapter presents only the theory of single layer permeation in one-dimension, as it is relevant to the activities described in this thesis.

The permeation of hydrogen through structures can be defined as the migration of hydrogen atoms from one side of a membrane to the other side. However, permeation is not a basic phenomenon, but the resultant of various interrelated processes. Indeed, hydrogen transport through a membrane occurs in 7 stages [30] [31]: adsorption, dissociation, absorption, diffusion (in the bulk and onto subsurface), recombination and desorption, as shown in Figure 2.1.

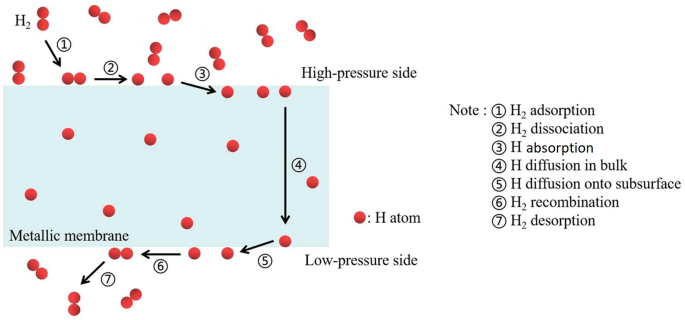

Figure 2.1. Scheme of hydrogen permeation through solid material [32]

Firstly, hydrogen molecules are attracted by the metal membrane (adsorption), which tends to complete its valence orbitals, and after the molecule dissociates, the adsorbed hydrogen atoms occupy the interstitial sites of the membrane lattice. Then, hydrogen atoms move from the surface to the bulk of the metal membrane (absorption). Later, hydrogen diffuses between the interstitial sites due to the concentration gradient (diffusion). When hydrogen reaches the other side of the membrane, recombination and desorption processes occur, allowing hydrogen to

leave the membrane in a molecular form.

Adsorption, desorption, dissociation and recombination are called "surface processes" because they take place in the "surface layer", that is the layer just below the solid surface, different from the bulk of the solid. Instead, absorption and diffusion are known as "bulk processes". It is useful to specify the differences between absorption and adsorption: the first one is an accumulation of particles throughout the another substance while the second is an accumulation of particles onto the substance surface.

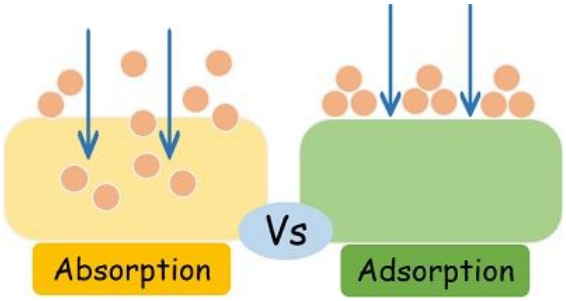

Figure 2.2. Schematic difference between absorption and adsorption

In LiPb, hydrogen solubilizes in atomic form so, when hydrogen transport starts from the liquid metal, the process of dissociation does not occur.

Thermomigration (or Soret effect) and trapping at defects are other "bulk processes". In particular, internal trapping is a process that consists in a capture and release of hydrogen atoms by different sites with respect to the normal solution ones. Indeed, Soret effect is a phenomenon that explain the different behavior of light and heavy atoms with respect to a thermal gradient: light molecules tend to move to hot regions while heavy molecules to cold regions.

2.1 Brief excursus on chemical kinetics and thermodynamics

This introductory section has been conceived to systematically approach the subject, as many sources available in literature discuss it in a not extensive or incomplete manner. This section is based on [33] and [34].

2.1.1 Equilibrium constant in reaction kinetics

When a substance A reacts, it disappears with a rate v expressed by:

$$v = -\frac{dc}{dt} \tag{2.1}$$

where c is the concentration that diminishes by an infinitesimal factor dc in the infinitesimal time dt. The reaction rate is experimentally determined, and its trend can depend on concentration in various ways.

If v is directly proportional to the concentration of the reactant A through a constant (called the rate constant k), the reaction is said to be of the first order:

$$v = k \cdot [A]^1 \tag{2.2}$$

Instead, if v is directly proportional to the square of the concentration, the reaction is said to be of the second order:

$$v = k \cdot [A]^2 \tag{2.3}$$

Indeed, the dimensions of k depend on the reaction kinetics and have to be determined case by case.

Generalizing, the reaction rate of a general reaction:

$$\alpha A + \beta B \rightleftarrows \rho R + \sigma S \tag{2.4}$$

is equal to:

$$v = k \cdot [A]^n \cdot [B]^m \tag{2.5}$$

where n and m are the reaction orders with respect to the reactants A and B, which have to be experimentally determined.

However, in a *diluted solution*, an elementary reaction, which means a reaction in which the reactants react directly in a single step and with a single transition state, obeys to the *law of mass action* (or *law of chemical equilibrium*): the reaction rate is given by the reactant concentrations, each raised to the corresponding stoichiometric coefficients.

$$v = k \cdot [A]^\alpha \cdot [B]^\beta \tag{2.6}$$

So, at equilibrium, the reaction Equation (2.4) proceeds with the same rate in both directions and so it is possible to define a direct rate constant, k_d, and an inverse one, k_i:

$$v = k_d \cdot [A]^\alpha \cdot [B]^\beta \tag{2.7}$$

$$v = k_i \cdot [R]^\rho \cdot [S]^\sigma \tag{2.8}$$

By equaling them:

$$k_d \cdot [A]^\alpha \cdot [B]^\beta = k_i \cdot [R]^\rho \cdot [S]^\sigma \tag{2.9}$$

$$\frac{k_d}{k_i} = \frac{[R]^\rho \cdot [S]^\sigma}{[A]^\alpha \cdot [B]^\beta} = K_{eq} \tag{2.10}$$

This ratio is numerically equal to the equilibrium constant K_{eq}, as shown in the following. Equation (2.10) is important from a conceptual point of view as it represents the link between chemical kinetics and thermodynamics.

The rate constant dependence on temperature can be expressed by means of an Arrhenius equation:

$$k = A \cdot \exp\left(-\frac{E_a}{RT}\right) \tag{2.11}$$

where A is called pre-exponential factor, E_a is the activation energy, R in J/(mol K) is the gas constant and T is the temperature. The pre-exponential factor takes into account the activation entropy, the total number of molecular collisions and the *steric factor* (also known as the probability factor). In order for two molecules to react, they have to bump into each other, and the collision has to be effective, which means that the molecules must have a sufficient energy for the reaction to happen and the collision must happen with proper orientation. The latter condition is mathematically expressed by the *steric factor*, which is the ratio of the cross section for reactive collisions to the total collision cross section.

Using Equation (2.10) and Equation (2.11), it is possible to write:

$$K_{eq} = \frac{k_d}{k_i} = \frac{A_d \cdot \exp\left(-\frac{E_{a,d}}{RT}\right)}{A_i \cdot \exp\left(-\frac{E_{a,i}}{RT}\right)} = A \cdot \exp(-\frac{\Delta E_a}{RT}) \tag{2.12}$$

This is called the *Van't Hoff equation*, that is better described in the following Section 2.1.2.

The *law of mass action*, mentioned above Equation (2.6), is fundamental to quantitatively study chemical reactions. Let's consider a generic homogeneous reaction in *gas phase* and in *chemical equilibrium*:

$$\alpha A + \beta B \rightleftarrows \rho R + \sigma S \tag{2.13}$$

It is possible to define an equilibrium constant (K) in terms of molar concentrations (K_c) or partial pressures (K_p):

$$K_c = \frac{[R]^\rho \cdot [S]^\sigma}{[A]^\alpha \cdot [B]^\beta};\ K_p = \frac{p_R^\rho \cdot p_S^\sigma}{p_A^\alpha \cdot p_B^\beta} \tag{2.14}$$

These quantities are constant at fixed temperature. The two constants are related by:

$$K_p = K_c \cdot (RT)^\omega \tag{2.15}$$

where ω is defined as:

$$\omega = (\rho + \sigma) - (\alpha + \beta) \tag{2.16}$$

Therefore, K_p and K_c are equal when the reaction does not lead to a variation of the total number of gaseous moles.

The above-defined formulas Equation (2.14)for the equilibrium constants (K_c and K_p) are valid for calculations but are not dimensionally exact (K is, by definition, a dimensionless constant). Indeed, the factors $(1/c_0)^\omega$ and $(1/p_0)^\omega$, included in the original definition Equation (2.23), are generally omitted being equal to 1 (c_0 being the standard concentration and p_0 the standard pressure, i.e. 1 mol/L and 1 atm at 25 °C).

K_c is generally used for liquid solutions, while K_p for gaseous ones. Another important thing to notice is that the value of K depends on the way the reaction is written, so it is important to remember that normally the stoichiometric coefficients must be the smallest integers that balance the reaction.

2.1.2 Equilibrium constant in thermodynamics

The section is divided in two cases: the homogeneous and the non-homogeneous solution.

Homogeneous solutions

The equilibrium constant is originally introduced in the estimation of the Gibbs free energy of a reaction.

Gibbs free energy G is defined, for a homogeneous solution, as:

$$G = H - T \cdot S = U - TS + pV \tag{2.17}$$

where H is the enthalpy, S the entropy, V the volume, T the temperature and U the internal energy.

Being the Gibbs free energy a state function, it is always given with respect to a reference state, which is the standard one (25 °C, 1 atm).

By differentiating Equation (2.17) and knowing that $dU \coloneqq TdS - pdV$, we obtain:

$$dG = (dU) - TdS - SdT + Vdp + pdV = (\cancel{TdS} - \cancel{pdV}) - \cancel{TdS} - SdT + Vdp + \cancel{pdV} = Vdp - SdT \tag{2.18}$$

Remembering the ideal gas equation for 1 mol ($pV = RT$), by substitution of V:

$$dG = \frac{RT}{p} dP \tag{2.19}$$

By integration between the standard state and the pressure p_A (partial pressure of species A in the equilibrium Equation (2.13)), considering α moles of gas with respect to Equation (2.13), the following equation is obtained:

$$\Delta G_A = \alpha G_A - \alpha G_A^0 = \alpha RT \cdot \ln\left(\frac{p_A}{p_0}\right) \tag{2.20}$$

and so

$$\alpha G_A = \alpha G_A^0 + \alpha RT \cdot \ln\left(\frac{p_A}{p_0}\right) \tag{2.21}$$

where G_A^0 is the standard Gibbs free energy of the species A, considered pure and in equilibrium at 1 atm, and 25 °C. It depends on the physical state of the chemical elements.

For a reaction the variation of the Gibbs free energy is given by:

$$\Delta G = \sum \Delta G_{prod} - \sum \Delta G_{reag} \tag{2.22}$$

Being $\Delta G = 0$ at equilibrium, after some math, the following equation can be found:

$$\Delta G_0 = -RT \cdot \ln\left[\frac{(p_R^\rho \cdot p_S^\sigma)}{p_A^\alpha \cdot p_B^\beta} \cdot \left(\frac{1}{p_0^\omega}\right)\right] \tag{2.23}$$

The argument of the logarithm is the equilibrium constant of the reaction in terms of partial pressures K_{p0} (dimensionless), as defined in Equation (2.15):

$$\Delta G^0 = -RT \cdot \ln(K_{p_0}) \tag{2.24}$$

Also in this case, it is important to notice that the numerical value of ΔG changes if K is calculated with respect to the pressure or the concentration.

For a liquid solution, the osmotic pressure π is introduced: the minimum pressure which needs to be applied to a solution to prevent the inward flow of its pure solvent across a semipermeable membrane. It can be found, for a diluted solution, that $\pi = cRT$ with $c = \frac{n}{V}$. This equation is formally equal to the ideal gas law. With a mental experiment, it is possible to imagine extracting the solute moles from the solution of volume V at osmotic pressure π and temperature T and putting them in gas phase in a container also of volume V and temperature T. The solute moles will exert a pressure p on the container. By equaling the ideal gas law and the equation for a diluted solution it is possible to obtain that $\pi = p$. Therefore, ΔG can be also expressed in terms of concentrations.

Remembering that in an omogeneous solution $\Delta G^\circ = \Delta H^\circ - T\Delta S^\circ$ and with some math it is simple to see that Equation (2.24) is equivalent to *Van't Hoff equation* (2.12).

Let's now talk about the correlation between the equilibrium constant, the pressure and the temperature. The equilibrium constant depends only on the temperature and the relation is expressed by the *Van't Hoff equation* 2.12 for small temperature variations, so that it is possible to consider ΔH° and ΔS°constant

Regarding the effect of pressure on the equilibrium, if the elements are gases, the pressure does not affect K but rather the composition of the equilibrium, i. e. the ratio between reagents and products. For example, in a reaction where the total amount of mole decreases, a pressure increase promotes the reaction, and vice versa.

Non-homogeneous solutions

In non-homogeneous solutions, ΔG has an additional term that is related with the increasing of free energy of a phase due to the addition of a mole of a species i (atomic, molecular or nuclear), when p, T and the quantities (moles) of the other components ($n_{j\neq i}$) are constant. This term is named *chemical potential*:

$$\mu_i = \left(\frac{\partial G}{\partial n_i}\right)_{T,p,n_{j\neq i}} \tag{2.25}$$

In differential terms:

$$dG = \cancel{TdS} - \cancel{pdV} - \cancel{TdS} - SdT + \cancel{pdV} + VdP + \sum \mu_i \partial n_i \tag{2.26}$$

Being $dG = 0$ at the equilibrium and if T and p are constant, the following equation can be derived (where 1 and 2 are different phases of the solution):

$$\sum \mu_i \partial n_i = 0 \tag{2.27}$$

And if the number of mole is kept constant:

$$\mu_{i1} = \mu_{i2} \tag{2.28}$$

The chemical potential of an ideal gas, when T is constant, can be written as:

$$\mu = \mu^{\circ}(g) + RT \cdot \ln\left(\frac{p}{p^{\circ}}\right) \tag{2.29}$$

where p° and μ° are the pressure and the chemical potential in standard conditions.

2.1.3 Solubility

To conclude this section, it is important to introduce the solubility S that is defined as the maximum amount of solute that can be dissolved into a solvent. A more detailed definition is:

$$S = \left[\frac{n\ (moles\ of\ solute)}{V \cdot (1\ liter\ of\ saturated\ solution\ at\ equilibrium)}\right]_{T=cost} \tag{2.30}$$

So, at a particular pressure in Pa and temperature in K, the solubility of a gas in a material is the concentration of gas dissolved in it at the equilibrium: $S = c_{ee}$ in mol/m^3.

2.2 Surface processes

This section is based on [34] and [35]. As said in the introduction of this chapter, adsorption is a surface process that occurs at the interface between the gas and the solid.

The substance that adsorbs is named adsorbate while the underlying material is the adsorbent or substrate. The reverse process of adsorption is desorption.

Two kinds of adsorption exist: the physical and the chemical one. The former, also called physisorption, is caused by the attractive *Van der Waals forces* and consists in the first interaction between the gas and the solid. Being the *Van der Waals forces* long-ranged but weak, the bond energy (also called heat of physisorption) is generally small, of the same order of magnitude as the enthalpy of condensation (about 8 kJ/mol). This energy can be absorbed by the lattice as vibrations and dissipated as thermal motion. A molecule slowly loses its energy and is finally adsorbed in the surface (accommodation).

Chemical adsorption (or chemisorption), instead, present a higher heat, more than 48 kJ/mol. This process, in fact, consists in the formation of covalent bonds between the gas atoms and the surface solid ones, which have not a closed-shell configuration (that is when low-lying energy levels are full and higher energy levels are empty). Chemisorption has an activation energy which depends on the surface conditions: if impurities are present this energy increases. In this process, the hydrogen molecule, previously physically adsorbed, dissociates.

Adsorption phenomenon is rapid at the beginning and slows down near the equilibrium; it is an exothermic reaction and it is favored by low temperature. The concentration on the surface of adsorbent is different from that in bulk.

2.2.1 Langmuir adsorption equation

The simplest physically plausible isotherm adsorption reaction is named after the American scientist Langmuir and it is based on 3 assumptions:

- Adsorption cannot proceed beyond monolayer coverage.
- All sites are equivalent and the surface is uniform (that is, the surface is perfectly flat on a microscopic scale).
- The ability of a molecule to adsorb at a given site is independent of the occupation of neighboring sites (that is, there are no interactions between adsorbed molecules).

As said, adsorption can occur with or without dissociation, giving two different isotherms. When one or more of the above-mentioned assumptions is not met, other isotherms can be found (i.e. BET (Brunauer, Emmett & Teller), when the first layer can foster further adsorption, Temkin or Freundlich isotherms, when the sites are not equivalent or independent). We discuss both cases in the following.

Adsorption without dissociation

Considering the following reaction:

$$A_g + M_{surface} \rightleftarrows A_{ad}M_{surface} \tag{2.31}$$

where A is the gaseous adsorbate, A_g when is gas phase and A_{ad} when it adsorbated, and $M_{surface}$ are the vacancies on the adsorbent surface that allow adsorption to occur, it is possible to write the reaction rate for adsorption and desorption as:

$$v_{ad} = k_{ad} \cdot [A_g] \cdot [M_{surface}] \tag{2.32}$$

$$v_{des} = k_{des} \cdot [A_g M_{surface}] \tag{2.33}$$

Defining θ the fraction of sites that are filled, that can be expressed as follows:

$$\theta = \frac{V_{ad}}{V_{available}} \tag{2.34}$$

with V_{ad} the number of adsorption sites occupied and $V_{available}$ the number of adsorption sites available, the following equations can be written:

$$v_{ad} = k_{ad} \cdot [A_g] \cdot (1 - \theta) \tag{2.35}$$

$$v_{des} = k_{des} \cdot \theta \tag{2.36}$$

At the equilibrium:

$$k_{ad} \cdot [A_g] \cdot (1 - \theta) = k_{des} \cdot \theta \tag{2.37}$$

Remembering Equation (2.10) and, after some rearranging, the following equation can be obtained:

$$\theta = \frac{[A_g] \cdot K_{eq}}{1 + [A_g] \cdot K_{eq}} \tag{2.38}$$

This equation is known as the *Langmuir adsorption equation* for the case without dissociation. When the concentration of the gas is much lower than 1, the Langmuir isotherm can be find:

$$\theta = [A_g] \cdot K_{eq} \tag{2.39}$$

Adsorption with dissociation

An example of adsorption with dissociation is the behavior of hydrogen in metals. When dissociation happens, a molecule of hydrogen must find two simultaneously free vacancies to be chemisorbed. Therefore, considering the reaction as a single step and elementary, the reaction can be written as:

$$H_2 + 2M_{surface} \rightleftarrows 2H_{ad}M_{surface} \tag{2.40}$$

Being that an elementary reaction, the reaction rates are:

$$v_{ad} = k_{ad} \cdot [A_g] \cdot [M_{surface}]^2 \tag{2.41}$$

$$v_{des} = k_{des} \cdot [A_g M_{surface}]^2 \tag{2.42}$$

Using the definition of θ introduced in Equation (2.34), reaction rates become:

$$v_{ad} = k_{ad} \cdot [A_g] \cdot (1 - \theta)^2 \tag{2.43}$$

$$v_{des} = k_{des} \cdot \theta^2 \tag{2.44}$$

At the equilibrium:

$$k_{ad} \cdot [A_g] \cdot (1 - \theta)^2 = k_{des} \cdot \theta^2 \tag{2.45}$$

Remembering Equation (2.10) and with some math the following equation can be obtained:

$$\theta = \frac{\sqrt{[A_g] \cdot K_{eq}}}{1 + \sqrt{[A_g] \cdot K_{eq}}} \tag{2.46}$$

This equation is known as the Langmuir adsorption equation for the case with dissociation. With respect to the case without dissociation, the surface coverage has now a weaker dependence on the gas concentration and so also on the gas pressure.

Figure 2.3 shows the shape of Langmuir isotherms as a function of gas partial pressure (and thus concentration) for different values of K_{eq}. The plot on the left shows that in absence of dissociation approach $\theta \to 1$ at lower pressures for the same

values of K_{eq}. A θ equal to 1 is only approached at very high pressure, when the gas is forced to enter in every available site of the surface.

It is worth noting that, when the product of the gas partial pressure and K_{eq} is small (i.e. on the bottom left corner of the two plots of Figure 2.3, the isotherm is linear).

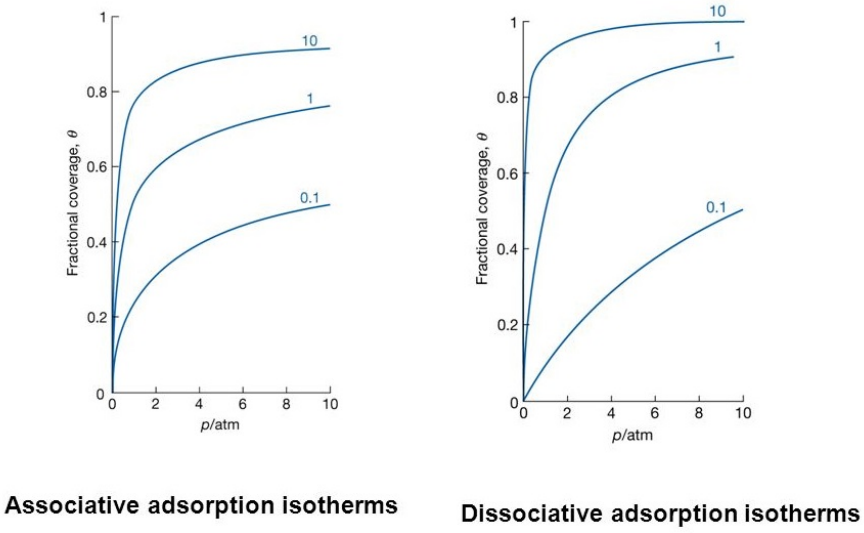

Figure 2.3. Langmuir isotherms [34]

2.3 Bulk processes

2.3.1 Absorption

After being adsorbed, the element crossed the outer surface of a solid moves into the subsurface and occupies a solution site of the host lattice. This process is the absorption and it is an endothermic reaction, generally not affected by temperature and occurs at uniform rate. The concentration tend to become the same throughout the material.

Atomic absorption of monoatomic gas by a solid

The pressure and the temperature are considered constant in the following. The absorption reaction for a atomic gas in a solid is:

$$A_g \leftrightarrow A_{abs} \tag{2.47}$$

whose equilibrium requires the chemical potential to be equal in the two phases:

$$\mu_g = \mu_{abs} \tag{2.48}$$

where μ_g is the chemical potential of gas per molecule and μ_{abs} is the chemical potential of the gas in solid solution per atom. These chemical potentials can be written as:

$$\mu_g = \mu_g^\circ + RT \cdot \ln\left(\frac{p}{p^\circ}\right) \tag{2.49}$$

$$\mu_{abs} = \mu_{abs}^\circ + RT \cdot \ln\left(\frac{\frac{C_{eq}}{z}}{1-\frac{C_{eq}}{z}}\right) \tag{2.50}$$

where

- z is the number of solution sites per host atom
- C_{eq} is the hydrogen concentration in atomic fraction
- T it the temperature in K
- R is the gas constant (8.314 J/(K mol)

By equaling these two equations, the following one can be obtained:

$$\frac{\frac{C_{eq}}{z}}{1-\frac{C_{eq}}{z}} = \exp\left(\frac{\mu_g^\circ - \mu_{ads}^\circ}{RT}\right) \cdot \left(\frac{p}{p^\circ}\right) \tag{2.51}$$

Substituting $\mu_g^\circ - \mu_{abs}^\circ$ with $-\Delta G^\circ$, having considered the temperature and the pressure constant 2.27:

$$\frac{\frac{C_{eq}}{z}}{1-\frac{C_{eq}}{z}} = \exp\left(\frac{-\Delta G^\circ}{RT}\right) \cdot \left(\frac{p}{p^\circ}\right) \tag{2.52}$$

When the hydrogen concentration is low (i.e. $C_{eq} << 1$), the following equation can be written as:

$$\frac{C_{eq}}{z} = \exp\left(\frac{-\Delta G^\circ}{RT}\right) \cdot \left(\frac{p}{p^\circ}\right) \tag{2.53}$$

Remembering Equation (2.24), Equation (2.53) becomes:

$$\frac{C_{eq}}{z} = K_{p0} \cdot \left(\frac{p}{p^\circ}\right) \tag{2.54}$$

From this, being $p_0 = 1$ atm, it is possible to derive the *Henry's law* by simply evaluating the equilibrium constant of the reaction:

$$K_{p,0} = \frac{c_{eq}}{p} \tag{2.55}$$

where:

- $K_{p,0}$ is the Henry's constant (equilibrium constant)
- C_{eq} is the concentration of the dissolved hydrogen atoms into the metal
- p is the hydrogen partial pressure at the interface with the metal.

From this equation, it can be seen that, when the gas is monoatomic, C_{eq} is proportional to the pressure.

Atomic absorption of a diatomic gas by a solid

In this section, hydrogen will be used as archetype of diatomic gases, as it is the main focus of this thesis. The absorption reaction of molecular hydrogen in a solid is:

$$H_2(g) = 2H(ads) \tag{2.56}$$

The process involves a non-homogeneous solution and in the calculation of the *Gibbs Energy* it is important to take into account the term of chemical potential that is related with the increase of free energy of a phase due to the addition of a mole of a component i. At equilibrium:

$$(\mu_{H_2 g} - \mu_{H_{abs}})\, dn_i = 0 \tag{2.57}$$

$$\mu_{H_2 g} = 2 \cdot \mu_{H_{abs}} \tag{2.58}$$

The chemical potential of the hydrogen in gas is:

$$\mu_g = \mu_g^\circ + RT \cdot \ln\left(\frac{p}{p^\circ}\right) \tag{2.59}$$

where p° and μ° are the pressure and the chemical potential in standard conditions.

The chemical potential of the hydrogen adsorbed in a uniform lattice, if hydrogen does not interact, is [35]:

$$\mu_{abs} = \mu_{abs}^\circ + RT \cdot \ln\left(\frac{\frac{C_{eq}}{z}}{1 - \frac{C_{eq}}{z}}\right) \tag{2.60}$$

The hydrogen concentration expressed in atomic fraction can be expressed as:

$$C_{eq} = c_{eq} \cdot 2 \cdot \frac{N_A}{N} = c_{eq} \cdot 2 \cdot \frac{A_s}{\rho_s} \tag{2.61}$$

where:

- N is the number of lattice atoms per unit volume
- N_A is *Avogadro's number*
- A_s is the molar mass of the solid
- ρ_s its density in g/m^3

By introducing in Equation (2.58) the Equation (2.59) and Equation (2.60):

$$\mu_g^\circ + RT \cdot \ln\left(\frac{p}{p^\circ}\right) = 2 \cdot \mu_{abs}^\circ + 2 \cdot RT \cdot \ln\left(\frac{\frac{C_{eq}}{z}}{1 - \frac{C_{eq}}{z}}\right) \tag{2.62}$$

and with some math, the following expression can be obtained:

$$\frac{\frac{C_{eq}}{z}}{1-\frac{C_{eq}}{z}} = \exp\left(\frac{\mu_g^\circ - 2\mu_{ads}^\circ}{2RT}\right) \cdot \sqrt{\left(\frac{p}{p^\circ}\right)} \tag{2.63}$$

Substituting $\mu_g^\circ - 2\mu_{abs}^\circ$ with $-\Delta G^\circ$, having considered the temperature and the pressure constant 2.27:

$$\exp\left(\frac{-\Delta G^\circ}{2RT}\right) \cdot \sqrt{\left(\frac{p}{p^\circ}\right)} = \frac{\frac{C_{eq}}{z}}{1-\frac{C_{eq}}{z}} \tag{2.64}$$

When the hydrogen concentration is low (i.e. $C_{eq} << 1$), Equation (2.64) can be written as:

$$\frac{C_{eq}}{z} = \exp\left(\frac{-\Delta G^\circ}{2RT}\right) \cdot \sqrt{\left(\frac{p}{p^\circ}\right)} \tag{2.65}$$

Remembering Equation (2.24), Equation (2.65) becomes:

$$\frac{C_{eq}}{z} = \frac{K_p}{2} \cdot \sqrt{\left(\frac{p}{p^\circ}\right)} \tag{2.66}$$

From this equation, it can be seen that C_{eq} depend on the square root of the pressure. This relationship is expressed by *Sievert's law* as:

$$c = K_s\sqrt{p} \tag{2.67}$$

where:

- K_s is called the *Sieverts' constant* in $\mathrm{mol/(m^3 Pa^{1/2})}$
- p is the gas partial pressure in Pa.

Figure 2.4 shows the temperature dependence of the Sievert's constant of tritium for different materials.

2.3.2 Diffusion

The *Fick's first law* 2.68 describes diffusion, i.e. the phenomenon for which there is a net movement of matter within a mixture between two regions with different concentrations:

$$J = -D \cdot \nabla c \tag{2.68}$$

where

- J is the diffusion flux in $mol/(m^2 \cdot s)$,
- D is the diffusivity in m^2/s,
- c is the concentration in mol/m^3.

The minus sign is needed to express the physical direction of the movement, which goes from higher concentrations to lower ones. *Fick's law* is the rate equation for mass diffusion, which occurs in gases, liquids or solids and is due to random molecular motion.

In the following the 1D case is considered. The flux and the concentration are a function of the position (x) within the solid. Moreover, during transient, the flux varies also with time and, in this case, the *Fick's first law* 2.68 has to be combined with the continuity equation for mass 2.69:

$$\frac{\delta c}{\delta t} = -\frac{\delta J}{\delta x} \tag{2.69}$$

obtaining, when D is independent of concentration, i.e. when the system remain chemically homogeneous, the *Fick's second law* 2.70:

$$\frac{\delta c}{\delta t} = -D\frac{\delta^2 c}{\delta^2 x} \tag{2.70}$$

Diffusion, in microscopic point of view, consist in hydrogen jumps among interstitial sites and every jump is independent from the others. So, diffusion can also be studied as a stochastic phenomenon, for whose discussion please refer to [36].

In Figure 2.5, temperature dependence of the diffusivity of tritium in different materials is reported.

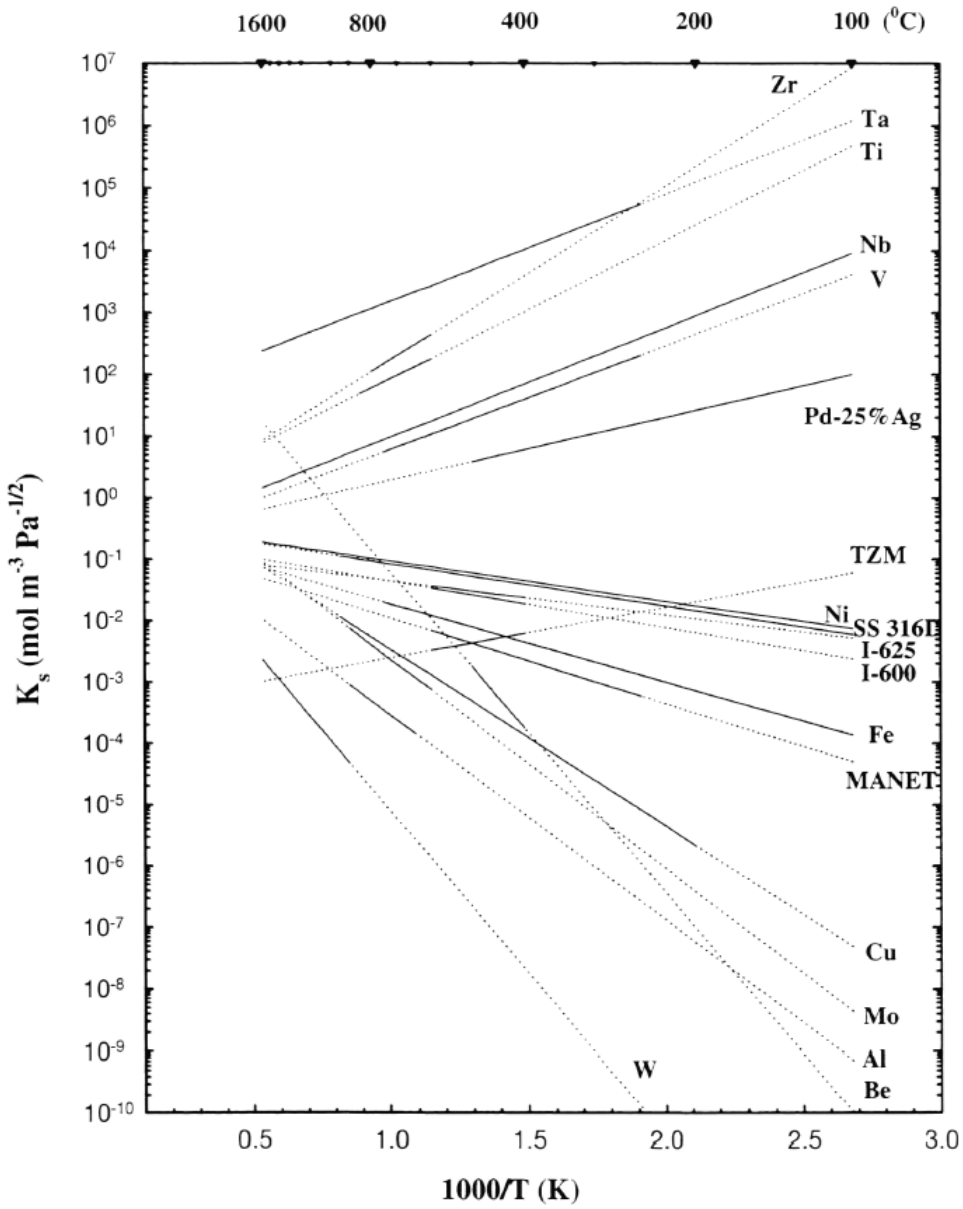

Figure 2.4. Temperature dependence of the Sievert's constant of tritium for different materials [35]

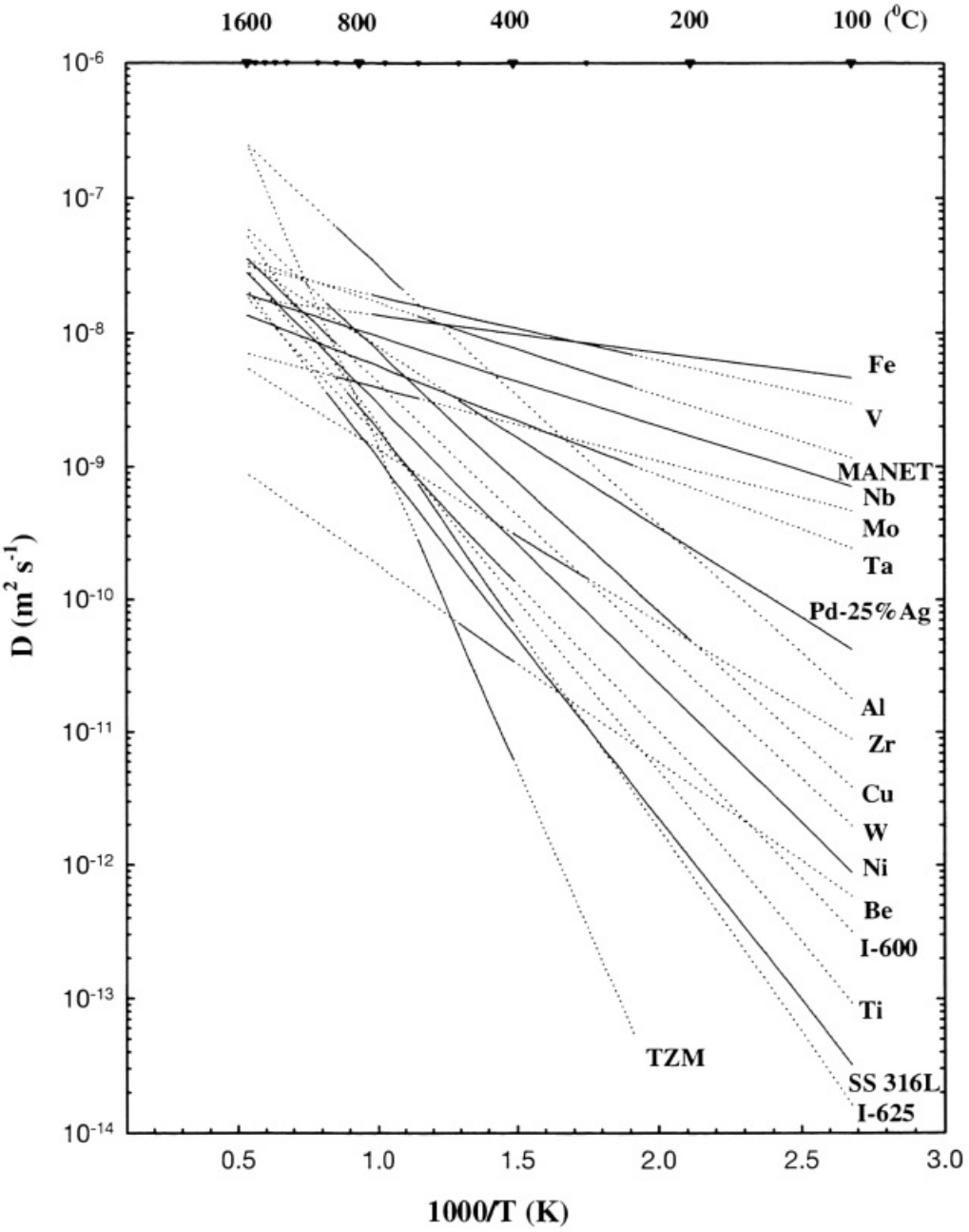

Figure 2.5. Temperature dependence of the diffusivity of tritium in different materials [35]

2.4 Brief excursus on permeation modelling

Experimental activities are the first step to reach a good basis towards an accurate modelling of the permeation phenomena. For this reason, an overview of the most common equations that can be found in modelling tools for hydrogen permeation is given in this section. For simplicity's sake, only one-dimensional problems are considered in this discussion.

The kinetics of the hydrogen transport can be limited by surface or by diffusion processes.

2.4.1 Diffusion Limited Regime

When the regime is diffusion limited, i.e. the slowest process is diffusion, Richardson's law can be applied. Richardson's law [37] describes the steady state behavior of a hydrogen flux permeating through a metallic membrane with a partial pressure difference between its sides:

$$J = \frac{DK_s}{d}\left(\sqrt{P_h} - \sqrt{P_l}\right) \tag{2.71}$$

where:

- J is the rate of gas permeation per unit area of material in mol/(m^2·s),
- D is the hydrogen diffusivity of the membrane material in m^2/s,
- K_s is the Sieverts' constant in the membrane material in mol/(m^3·$Pa^{1/2}$),
- d is the membrane thickness in m,
- p_h and p_1 are the hydrogen partial pressure in the high and low pressure sides in Pa.

The product of diffusivity and of the *Sieverts' constant* is usually called permeability and it is indicated with Φ in mol/($m \cdot s \cdot Pa^{1/2}$). Diffusivity, solubility and permeability follow, at low hydrogen concentrations, an *Arrhenius function* with temperature.

2.4.2 Surface Limited Regime

When surface process controls the permeation through a membrane and the concentration/pressure is low, for both surfaces of a slab there are two fluxes, one of adsorption/desorption and one of dissociation/recombination. The phenomenon that prevails depends on the species concentration close to the surfaces of the slab.

The adsorbed flux J_{ad} can be expressed as:

$$J_{ad} = \sigma \cdot k_{ad} \cdot p \tag{2.72}$$

where J_{ad} is expressed in mol/m^2s, p is the pressure close to the considered surface, σ is the roughness factor (ratio between the real area and the geometrical one) and k_{ad} is the adsorption constant in $m\,m^{-2}\,s^{-1}\,Pa{-}1$.

Similarly, the recombination rate J_r can be expressed as:

$$J_r = \sigma \cdot k_r \cdot c^2 \tag{2.73}$$

where k_r is the recombination constant and c is the concentration inside the slab, below the considered surface. In this case, the relationship with the concentration is quadratic do to the involvement of two atoms to form a molecule.

In steady-state conditions, it can be shown that, once the equilibrium has been reached, $k_a = k_r \cdot K_s^2$.

2.4.3 Mixed Regime

In general, if the steady state flux through a membrane of a gas is proportional to p the process is in a surface limited regime, while if the flux is proportional to $\sqrt{p}$ the process is a diffusion limited regime.

In the steady-state analysis of the intermediate regime, both the equations of diffusion and surface limited regime have to be applied, to consider molecular adsorption and desorption, surface dissociation and recombination and diffusion within the lattice. In the case of symmetrical membrane and downstream pressure negligible compared with the upstream pressure (which is the case of PAV), a dimensionless numbers can be introduced [38]:

$$W = \frac{\sigma \cdot k_{ad} \cdot d}{\Phi} \cdot \sqrt{p} = \frac{\sigma \cdot k_r \cdot K_s \cdot d}{D} \cdot \sqrt{p} \tag{2.74}$$

W^2 is named *reduced permeation flux density* and this parameter allows to know what kind of regime dominates the transport. If $W << 1$ it means that the permeation is limited by surface processes and J is proportional with p. Vice versa, if $W >> 1$ the permeation is limited by bulk processes and J is proportional with $\sqrt{p}$.

This parameter is used to write the general equation for the steady state permeation across a symmetrical membrane:

$$W^2 \cdot C^4 + 2W \cdot C^3 + 2C^2 = 1 \tag{2.75}$$

where C is the reduced concentration:

$$C = \frac{c}{c_{eq}} \tag{2.76}$$

These equations are valid for hydrogen transport from a gas phase through a membrane. However, this thesis deals mainly with hydrogen dissolved in atomic form in a liquid metal, LiPb. In this case, hydrogen has first to move in LiPb in order to reach the membrane. This process occurs following a concentration gradient in the LiPb and the flux can be written as:

$$J = K_t \cdot (c_{b,LiPb} - c_{m,LiPb}) \tag{2.77}$$

where $c_{b,LiPb}$ and $c_{m,LiPb}$ are the hydrogen concentration in the bulk of the LiPb flow and at the interface between LiPb and the membrane, while K_t is the mass transfer coefficient. K_t is the analogous of the heat transfer coefficient and, like it,

is usually determined by empirical correlations, which take into account the fluid properties and its motion.

To write the solution for the steady state flux through the entire system, i.e. liquid metal-membrane-vacuum in the case of a PAV, it is useful to introduce a second dimensionless parameter, firstly introduced by Humrickhouse [39]:

$$\zeta = \frac{D \cdot K_{s,m}}{K_t \cdot K_{s,LiPb} \cdot d} \tag{2.78}$$

where $K_{s,m}$ and $K_{s,LiPb}$ are the Sieverts' constants of the membrane and of the LiPb, respectively. ζ is sometimes referred to as the *partition parameter*, for instance in [40].

Introducing the dimensionless flux J^* (p_{LiPb} is the hydrogen partial pressure in LiPb):

$$J^* = J \cdot \frac{d}{D \cdot K_{s,m} \cdot \sqrt{p_{LiPb}}} \tag{2.79}$$

and using the definitions of W (eq. (2.74)) and ζ (eq. (2.78)), it is possible to write:

$$J^* = \frac{\left(\sqrt{1 + 4W \cdot (\zeta + 1)} - 1\right)^2}{4W \cdot (\zeta + 1)^2} \tag{2.80}$$

If $\zeta << 1$, the hydrogen transport is limited by the membrane and the expression of the flux becomes:

$$J^* = \frac{\left(\sqrt{1 + 4W} - 1\right)^2}{4W} \tag{2.81}$$

and, from there, it is possible to come back to the above-defined Diffusion Limited Regime ($W >> 1$, $J^* = 1$) or Surface Limited Regime ($W << 1$, $J^* = W$).

Vice versa, if $\zeta >> 1$, the mass transport in the LiPb is the limiting phenomenon only when combined with $W > 1$ ($J^* = 1/\zeta$), because when $W < 1$ the regime is mixed and the dimensionless flux is described by Equation (2.80).

Chapter 3

Overview of the technologies

This chapter describes the technologies whose development this thesis aims to support: the technologies for tritium extraction from LiPb (Gas-Liquid Contactor and Permeator Against Vacuum) and the technologies currently under investigation to deposit alumina coatings on structural materials (Pulsed Laser Deposition and Atomic Layer Deposition). In order to offer a more comprehensive overview of the research activities in these two fields within EUROfusion, the Liquid-Vacuum Contactor extraction technology and the Electrochemical Deposition are also described in this chapter, even if they are not part of this thesis' work.

3.1 Tritium Extraction Systems

Three Tritium Extraction technologies are currently under investigation within EUROfusion: the Gas-Liquid Contactor, the Permeator Against Vacuum and the Liquid-Vacuum Contactor. The latter is currently considered as a back-up option, but activities are on-going at CIEMAT to characterize its performances. The descriptions below are often based on the report on tritium extraction R&D [13].

3.1.1 Gas-Liquid Contactor

Starting with the Gas-Liquid Contactor, historically it has been the most studied among these technologies, with experiments performed at CEA with MELODIE facility in the late '90s and early 2000s [41],[15] and later at ENEA Brasimone with TRIEX [42] in 2006-2007 and TRIEX-II facilities, starting from 2019 [43]. Outside of Europe the GLC has received some attention especially in Japan [44].

In the Gas-Liquid Contactor, the extraction of the hydrogen isotopes from the LiPb is realized by using a purge gas (helium, or helium plus hydrogen) which is flushed in counter-current with a flow G with respect to the LiPb flow (L) in the column. Due to the low solubility of the hydrogen isotopes Q (Q=H,D,T) in LiPb and to its concentration gradient at the LiPb/gas interface, a mass transport with the passage of hydrogen isotopes from LiPb to the gas phase occurs (Figure 3.1).

The higher the LiPb/gas interface, the greater the total flow of extracted Q. Packed columns are used for increasing the interfacial area. The extraction process of Q from the LiPb is also determined by the thickness of the LiPb film on the surface

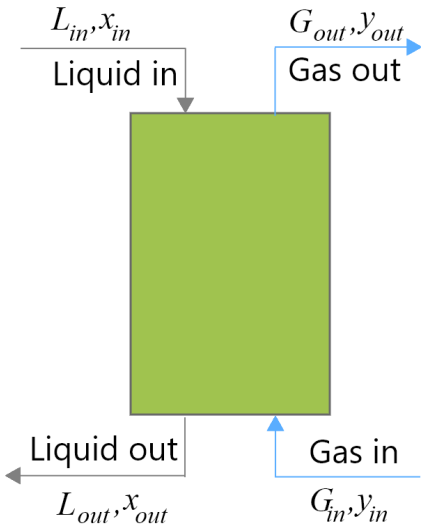

Figure 3.1. Sketch of the working principle of the Gas-Liquid Contactor

of the metal sheet forming the column filling: the lower the LiPb film thickness, the lower the time required for transporting Q into the LiPb and towards the gas interface through diffusion.

The main advantage of GLC is the larger experience with respect to the other technologies coming from years of tests and experiments and from its utilization in many conventional industrial fields.

GLCs require two auxiliary systems: a gas system that has to inject an appropriate flow rate of the stripping gas directly into the LiPb and a system to extract tritium from the stripping gas, so that it can be routed to the Tokamak Exhaust Processing.

Regarding the gas system, the two most challenging components are the compressor and, especially, the gas injector. The latter proved to have two operational problems from the experience gathered with the operation of TRIEX and TRIEX-II facilities:

- LiPb tends to enter in the helium injection line, especially if the helium flow rate is low. This complicates also the loading of the alloy into the facility, as a continuous flow of gas has to be maintained for the entire loading process to avoid the blockage of the injection line;
- GLC operates with a gas dome, complicating the level control in the expansion tank. For example, changing the pump speed can cause a dangerous increase of the level in the GLC or in the expansion tank (depending on their position in the loop). For the WCLL TER, this point is mainly relevant in case of a failure of the pumping system or of an abrupt change of its head (e.g. in case of an emergency draining).

These two points suggest that a careful design of the helium injection system, and of the system that spreads helium into the LiPb flow, is required to minimize the risks.

As far as the tritium extraction from helium is concerned, the GLC shares common R&D with the helium system of the HCPB (Helium Cooled Pebble Beds)

BB. The status of the R&D on this topic is summarized in [45]. Two processes for tritium extraction from helium have been studied for the HCPB BB: tritium removal by membrane separation and tritium removal by adsorption. The latter is currently considered as the reference technology, as the membrane separation did not demonstrate a sufficient maturity level to be further developed during the Conceptual Phase. Two types of adsorption processes are currently being investigated: Cryogenic Molecular Sieve Beds is considered the reference process with Q_2 adsorption on Getter Beds as the back-up.

Regardless of which process will prove to be the best for the needs of the HCPB BB, the GLC for the WCLL BB will require an additional system to remove tritium from helium in addition to the system which extracts it from LiPb. This drawback will be taken into consideration for the selection of the reference extraction technology for the WCLL BB.

3.1.2 Permeator Against Vacuum

The Permeator Against Vacuum has been mainly analysed from theoretical and modelling points of view, while the experiments have been devoted to the measurements of fundamental quantities, such as the diffusivity of materials of interest (e.g. [46]) or the surface effects on permeation (e.g. [47]). Design activities of a PAV for DEMO have also been carried out, especially at CIEMAT and Politecnico di Torino [31]. Experimental activities devoted to the characterization of the technologies have started both at CIEMAT [48] (made of vanadium, planar configuration) and at ENEA Brasimone [49] (made of niobium, U-tubes configuration), but no results have been made available before the experiments described in Chapter 5 of this thesis. Most recently, a new experimental facility, TEX, has been designed and built at Idaho National Laboratories to test a PAV made of vanadium [50]. The mock-ups of ENEA and CIEMAT are shown in Figure 3.2 and Figure 3.3.

PAVs are based on the phenomenon of tritium permeation through a membrane in contact with LiPb towards a secondary side where vacuum is pumped. Vacuum is needed to keep a partial pressure gradient between the two sides of the membrane, so that permeation can take place. The membrane has to be made with a tritium permeable material, such as α-iron [18], vanadium or niobium [19]. From a theoretical perspective, the PAV is the simplest of the extraction technologies and should offer a number of advantages, especially in comparison with the GLC:

- easy to operate as LiPb simply flows into some channels (no need to put two very different media in direct contact) and extraction happens by concentration gradient;
- extracted tritium is pure and can be directly transferred to the tritium processing plant. Instead, tritium extracted by GLCs is mixed with helium and, if a mix of helium and hydrogen is used as stripping gas, protium (H_2, T_2, HT). This avoids a processing step and, hence, simplifies the system and reduces the need for additional components, also minimizing the tritium residence time in the system [16];
- theoretical higher extraction efficiency with respect to GLC, implying lower dimensions of the overall component, paribus ceteris;

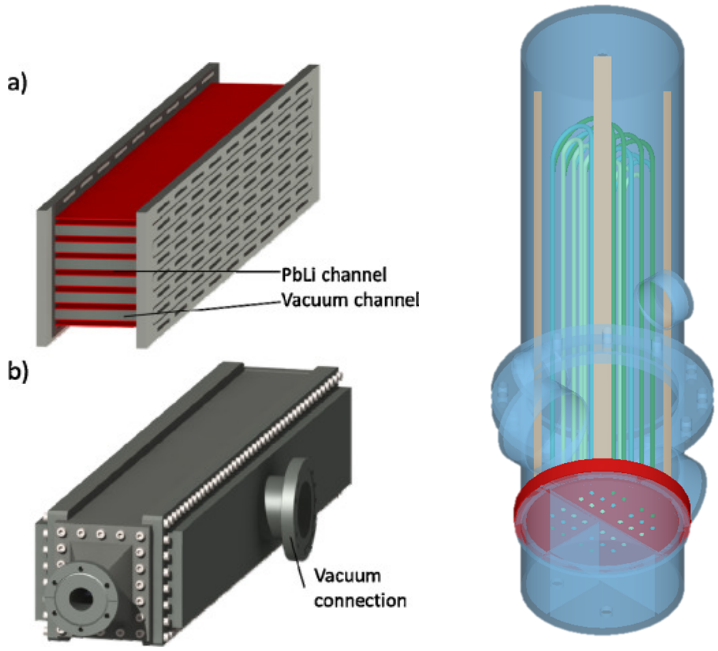

(a) (b)

Figure 3.2. Schematic drawings of the PAV mock-ups of CIEMAT (taken from [48]) and ENEA [49]

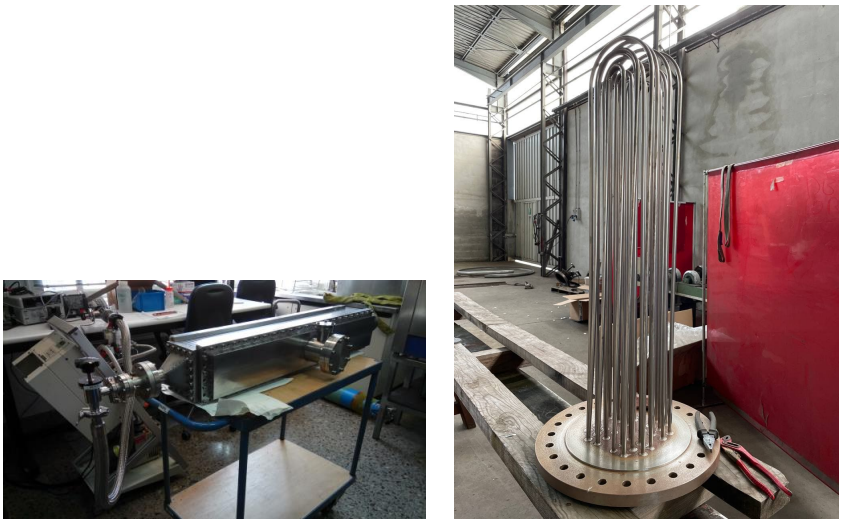

(a) (b)

Figure 3.3. Pictures of the PAV mock-ups of CIEMAT (taken from [51]) and ENEA (detail of the niobium tube bundle)[49]

- passive operation on the primary side;
- no residual hydrogen in the LiPb stream (only applicable in comparison with the GLC which operates with He+H2 as stripping gas).

However, GLCs are easier to be manufactured, also thanks to being a widely used technology in many industrial processes, and the technology has been tested in LiPb in several facilities, proving to be capable of extracting hydrogen isotopes from the alloy (but also confirming the many difficulties in operating a component where helium and LiPb have to flow in counter-current). Moreover, the secondary side of a PAV is a vacuum system, constituted by vacuum pumps and by appropriate fittings and flanges (e.g., any instrument installed inside the PAV would require vacuum connectors for signal and power cables). Moreover, these components must be compliant with the tritium regulamentory frames and safety protocols (e.g. oils cannot be used for sealings or pumps).

The biggest challenge in designing the vacuum system is the choice of the vacuum pumps. Generally, the minimum ratio between the tritium partial pressure at the LiPb side and at the vacuum side must be set to 10^{-2} and this is considered sufficient for proper PAV operation by establishing enough driving force for the tritium permeation. However, the precise vacuum requirement which corresponds to the value of that ratio is strongly dependent on the tritium solubility in LiPb. Large discrepancies exist in the values of the Sieverts' constant (K_s) available in literature. Usually, two correlations are considered during calculations, as they provide the lowest and the highest values of K_s: the one derived by Reiter [52] (about 10^{-8} at.fr.Pa$^{-0.5}$) and the one by Aiello [53] (about 10^{-6} at.fr.Pa$^{-0.5}$).

Unfortunately, the required vacuum pumping speed varies strongly with the adopted Sieverts' constant and some calculations have been performed in [54]. More details about the procedure followed in the calculation can be found in [55].

3.1.3 Liquid-Vacuum Contactor

Finally, the Liquid-Vacuum Contactor (LVC): this name comprehends two different technologies that takes advantage of the same working principle and which are called the Vacuum Sieve Tray and the Free Surface LVC. The former has been studied at Kyoto University by the group of Professor Okino [17],[56] and at KIT [57],[58]. The latter is a more recent concept that will be tested at CIEMAT in CLIPPER facility [59].

The Liquid-Vacuum Contactor is currently considered as a backup technology for the WCLL TER. In the LVC, the LiPb is brought into direct contact with high vacuum (in the order of 10^{-3} Pa [57]) in order to enhance the diffusive process of T solubilized in the liquid metal towards the vacuum.

In particular, the way in which the interface between LiPb and vacuum is created differentiates the Vacuum Sieve Tray (VST) and the Free Surface (FS). In the Vacuum Sieve Tray LiPb goes through a tray with calibrated nozzles that force LiPb to fall into vacuum as a liquid jet of droplets (Figure 3.4). This process should guarantee a high extraction efficiency, but the jet is highly unstable and can become intermittent if the velocity is reduced. The work by Prof. Okino has shown that frequent oscillations during the fall of the droplets can increase the hydrogen isotopes

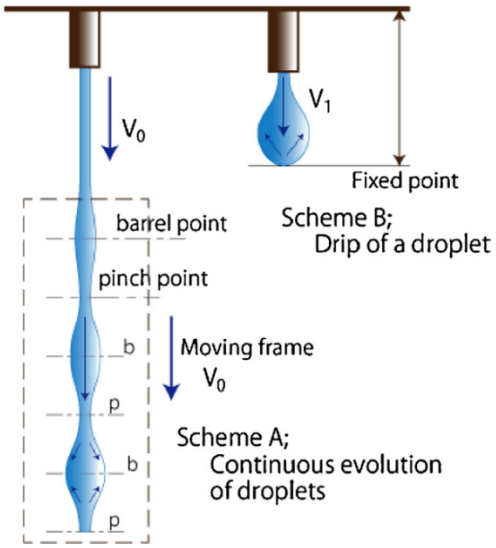

Figure 3.4. Sketch of the working principle of the Vacuum Sieve Tray: scheme A shows a continuous evolution of droplets; scheme B an intermittent droplet formation caused by the low velocity (taken from [17])

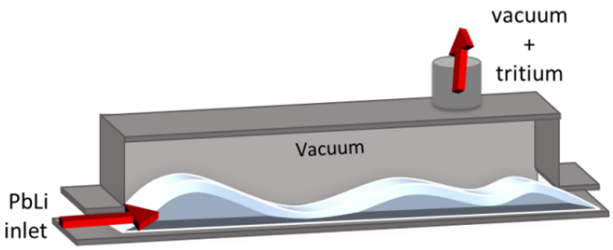

Figure 3.5. Sketch of the CIEMAT Free Surface LVC (taken from [60])

mass transport and, as a consequence, the extraction efficiency [17]. This concept is the less mature among the proposed technologies and the possibility to design, and then to operate, such a component at DEMO size has been questioned.

Differently from the VST, the interface between LiPb and vacuum in the Free-Surface LVC is created by forcing only a thin stream of LiPb to flow into the vacuum chamber. In the CIEMAT mock-up (Figure 3.5) that will be tested in CLIPPER facility the vacuum chamber is a rectangular box with a base area of 1x0.25 m, where a LiPb film of about 5 mm is generated [60]. In order to do so, a film generator is required at the inlet of the extractor, following an approach similar to that adopted in [61].

Both VST and FS LVCs would have similar requirements in terms of vacuum systems with respect to PAVs, with a more accurate estimation that will be possible only after a pre-conceptual design will be available. The only drawback of LVC on this matter is the need of a helium separation system, as helium will be present in the LiPb coming out from the BB (it is indeed a by-product of the lithium-neutron interaction) and will tend to be released towards vacuum because of its low solubility

in LiPb [11].

3.2 Coating technologies

The coating field is very wide in terms of both the materials that can be deposited and the techniques to perform the deposition. As it is not the objective of this thesis to analyse this subject in depth, this section will be limited to the three deposition techniques that are currently under investigation within EUROfusion for depositing alumina (Al_2O_3) in the WCLL BB and the TER. The techniques are the Pulsed Laser Deposition (PLD), the Atomic Layer Deposition (ALD) and the Electrochemical Deposition (ECX). One of them, the Pulsed Laser Deposition, is also the reference technique to coat the ALFRED internals. Many pieces of information in this section are taken from [21] and [62].

The goal of any coating fabrication technique is to produce a protective barrier on a structural material in the required metallurgical state. The requirements of any fabrication technique are:

- the compatibility with the components geometry and fabrication sequence;
- to produce coating with acceptable performances;
- lifetime on the basis of components application.

Therefore, the selection of the best coating fabrication technique is strictly related to the component application. To select the best option for each components is necessary to perform the characterisation of the coating at relevant environment. The qualification have to taking into account different aspects:

- Coating microstructure: metallographic aspect, intrinsic defects (interlayer porosity, surface roughness,...) and extrinsic defects (cracks), influence of heat treatment (intrinsic to the coating process or needed for the base material treatment, the weld relaxation, etc.);
- Coating mechanical proprieties: adhesion, scratch resistance, hardness, deformation resistance (bending tests, tensile tests, mechanical and thermal fatigue tests);
- Coating chemical resistance: corrosion;
- Corrosion resistance under ageing and irradiation;
- Mechanical coating characteristic;
- Industrial feasibility of the coating fabrication.

3.2.1 Electrochemical Deposition

The Electrochemical Deposition coats steel surfaces with aluminum that can later diffuse by means of heat treatment in argon (Figure 3.6). During the heat treatment a thin layer of α-alumina, the coating itself, is created on the steel surface [63]. More

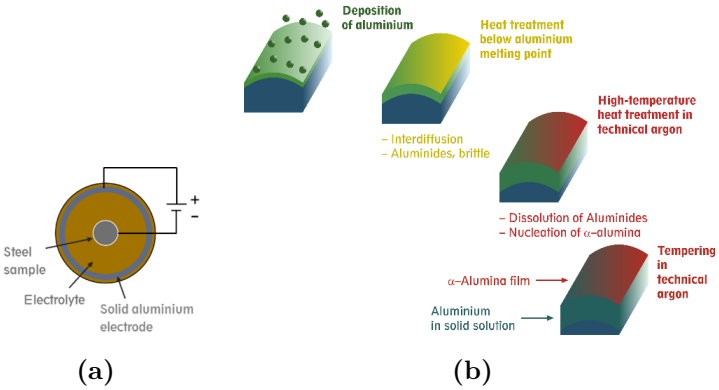

Figure 3.6. Illustration of the ECX process consisting of electroplating of aluminium on steel (a) and a three-step heat treatment (b), taken from [64]

specifically, the ECX is performed by electroplating, which is an industrial process widely used for components of different sized and geometries, with an ionic liquid as electrolyte.

ECX has several advantages, among which the fact that the aluminum reservoir (aluminum in solid solution) underneath the oxide layer can allow self-healing of the coating in case of local failures of the oxide layer. Moreover, the operative temperature of the ionic liquid is quite low, being around 100°C, and the request for dry atmosphere during the heat treatment not particularly challenging. Coating of components with complex geometry and internal coating are generally feasible. The tests performed within the EUROfusion FP8 focused on the characterization of anti-corrosion and anti-permeation properties. Tests performed in PICOLO loop at KIT showed that ECX coatings can sharply decrease the corrosion rate of EUROFER samples with respect to the bare ones [65]. Moreover, tests with RIPER facility at CIEMAT demonstrated that ECX coatings can reduce tritium permeation with respect to bare EUROFER of a factor 50-500 depending on the test temperature, but this is reduced of a factor 5 after irradiation with electrons [21].

Alumina coatings are also considered for MHD pressure drops reduction in the WCLL BB, by electrically insulating the LiPb from the BB structure. However, the ECX-made alumina layer in the course of the heat treatment in argon is currently too thin to satisfactorily reduce electrical conductivity, which has been measured in vacuum and argon (between 10^{-4} and 10^{-3} S/m).

After the performed tests, the ECX coatings are considered as a good solution for reducing corrosion of the the WCLL TER piping and the permeation towards the tokamak building, particularly as their easy fabrication makes them perfect to coat long pipelines. Instead, at the time of writing, they are seen only as a back-up option for the WCLL BB, where higher performances are requested, being outclassed by of ALD and especially PLD coatings [21].

3.2.2 Pulsed Laser Deposition

In the Pulsed Laser Deposition, as shown in Figure 3.7, a high-power pulsed laser beam is focused inside a vacuum chamber to strike an aluminum target. Part of

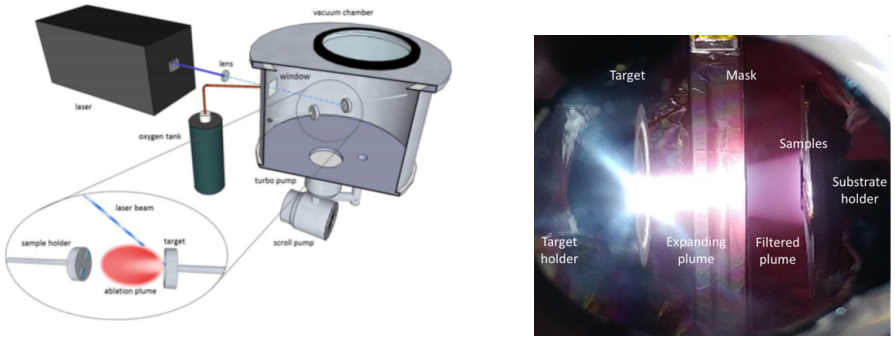

(a) (b)

Figure 3.7. Illustration of the PLD process, taken from [62], and picture of a deposition run, taken from [62]

the aluminum is vaporized and, as result, a high homogeneous layer of alumina is deposited on the surface to be coated. This technique has the capability to coat on open surfaces and the coating process occurs at room temperature, so that also cold-worked steels can be coated. The coatings realized with this technique have a quasi-metal mechanical behavior, meaning that the coating properties are similar to those of the steel substrate [66].

After the characterization, alumina coatings deposited by PLD demonstrated to be able to fulfill their tasks as anti-permeation and anti-corrosion barriers at laboratory level (separated effects). PLD-made coatings reached PRFs higher than 10^5 [67] and demonstrated to be able to protect EUROFER both in stagnant and flowing PbLi.

Resistance to thermal cycling and small doses of radiation has also been demonstrated (irradiation with ions [68] and electrons [69] and also with neutrons at very low dpa). After irradiation with neutrons in LVR-15 reactor up to 0.04 dpa, combined with exposure to slowly flowing PbLi, PLD coatings maintained a PRF higher than 250, while not showing signs of wear [21].

The possibility of using PLD coatings as electrical insulators to reduce MHD pressure drops has also been demonstrated (electrical conductivity between 10^{-12} S/m in vacuum and 10^{-8} S/m in argon) [21].

PLD coatings have the intrinsic limitation of being able to coat only external surfaces, but they are currently considered as the reference for being deposited on the Double Wall Tubes (the water pipes that will cool the WCLL BB).

3.2.3 Atomic Layer Deposition

The Atomic Layer Deposition is a type of Chemical Vapour Deposition with the peculiarity of reaching the desired coating thickness by a sequential deposition of many monoatomic layers. As shown in Figure 3.8, each layer is deposited by a process divided in 4 phases: first, trimethylaluminum (TMA) is injected in the vacuum chamber and it reacts with the surface to be coated, producing gaseous byproducts and preparing the surface for the second injection; secondly, nitrogen is purged into the chamber to remove the gases; thirdly, water is injected and alumina

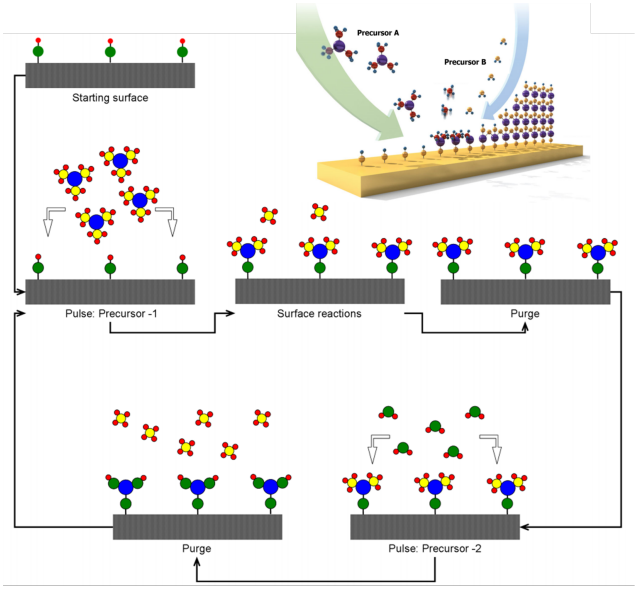

Figure 3.8. llustration and picture of the ALD process (taken from [21])

is formed on the surface together with other gaseous byproducts; finally, nitrogen is purged again to clean the chamber. TMA and water are called precursors. This process is then cycled until the appropriate film thickness is achieved.

This technique can produce high-quality amorphous coatings, it is performed at low temperature (100-250°C) and has the advantage of allowing the coating of more complex geometries with respect to PLD.

The R&D on alumina coatings deposited by ALD is slightly behind that for PLD coatings, as ALD coatings have not been irradiated with ions yet, let alone with neutrons. Moreover, the electrical conductivity of ALD coatings have not been measured yet.

The ALD coatings showed promising performances in terms of PRF (higher than 1000 [21]) and protection against corrosion in stagnant PbLi. Possibility of scaling-up was also demonstrated with a first increase of the deposition chamber (up to 300x200x300 mm^3) [21].

However, the demonstration of the ALD capability to protect relevant materials from the action of flowing PbLi has not been achieved, as it will be shown in Section 8.4 and this is the biggest obstacle for this technology to be considered the reference one for the WCLL BB.

Part II

Tritium Extraction Systems

Chapter 4

TRIEX-II facility

4.1 TRIEX-II facility description

TRIEX-II [43] is a facility designed to characterize the different technologies candidate as the Tritium Extraction Unit (TEU) of the WCLL TBS of ITER and the TER of DEMO. In particular, the facility will test two kinds of extractor technologies: the GLC, in the packed column configuration, and the PAV. The aim is to qualify the extraction of hydrogen or deuterium from flowing LiPb in the range of operative conditions foreseen for the WCLL TBM or BB. It is operated with hydrogen (or deuterium) instead of tritium for safety reasons and is equipped with prototypical components customized for LiPb applications. TRIEX-II is manufactured with 2 1/4 Cr-1 Mo steel (ASTM A335 Gr. P22), whose relatively low corrosion rate (low nickel content and consequent low degradation by precipitation [41]) allows the facility to be operated at high temperature for several thousand hours. Four main systems can be identified:

- the LiPb loop (primary loop)
- the vacuum system;
- the gas loop;
- the compressed air circuit

In the following paragraphs, a description of the different systems is provided, along with the details of their main components.

4.1.1 LiPb loop

The LiPb loop (Figure 4.1) consists of the following main components:

1. the storage tank S100;
2. the saturator S200;
3. the extractor S300 (GLC mock-up in the figure);
4. the permanent magnets pump EP100.

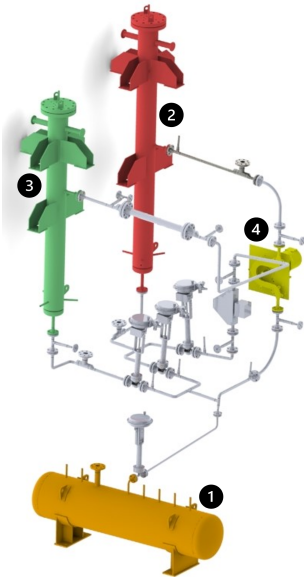

Figure 4.1. LiPb loop in TRIEX-II. In orange: storage tank S100; in red: saturator S200; in green: extractor S300 (GLC mock-up); in yellow: permanent magnets pump EP100.

Figure 4.2 shows the main window of the DACS (Data Acquisition and Control System) of TRIEX-II.

The LiPb is stored in the cylindrical storage tank (S100), which is connected through a 1/2" pipe to the rest of the loop. After the loading, the LiPb flows clockwise from the permanent magnets pump (EP100) to the saturator (S200), where hydrogen (or deuterium), carried by a flow of helium, is solubilized in the eutectic liquid metal. The LiPb enters the saturator from the top and exits from the bottom. Then, it flows towards to the top of the extractor (S300), where the mock-up for tritium extraction to be tested is placed. A thermal mass flow meter is installed between the saturator and the extractor. This instrument was designed by ENEA and Thermocoax and it was characterized in IELLLO facility [70]. The LiPb goes out from the bottom of the extractor and goes back to the pump. A bypass proportional valve is installed upstream of the extractor, with the aim to allow the draining of the pipe between the saturator and the extractor itself. This valve also allows, together with the pump, to control the flow rate (measured by the mass flow meter) entering the extractor. Six internal and more than twenty external type K thermocouples are installed throughout the piping. Each flange of the loop has a leakage detector that warns in case a LiPb leakage happens. Three helical hydrogen isotopes permeation sensors in pure iron, describe in Section 4.3.1 are used to measure hydrogenpartial pressure in LiPb. These sensors are installed in dedicated chambers located at the inlet of the saturator, between saturator and extractor and at the outlet from the extractor. The whole loop is heated by means of heating cables for bands and thermal insulated. Each heater is equipped with a control and a safety type K thermocouple (the control thermocouple monitors the heating rate, while the safety one measures the temperature of the heater, preventing its overheating).

The storage tank is equipped with:

- two internal thermocouples at different depths;
- a piezoresistive relative pressure transducer, with ceramic sensor;
- a guided micro-wave level meter;
- three heating bands.

The saturator and the extractor (GLC mock-up) are equipped with:

- two internal thermocouples at different depths;
- three heating bands;
- a piezoresistive relative pressure transducer, with ceramic sensor;
- three heating bands.
- four discrete level detectors (thermocouples used as electrodes).

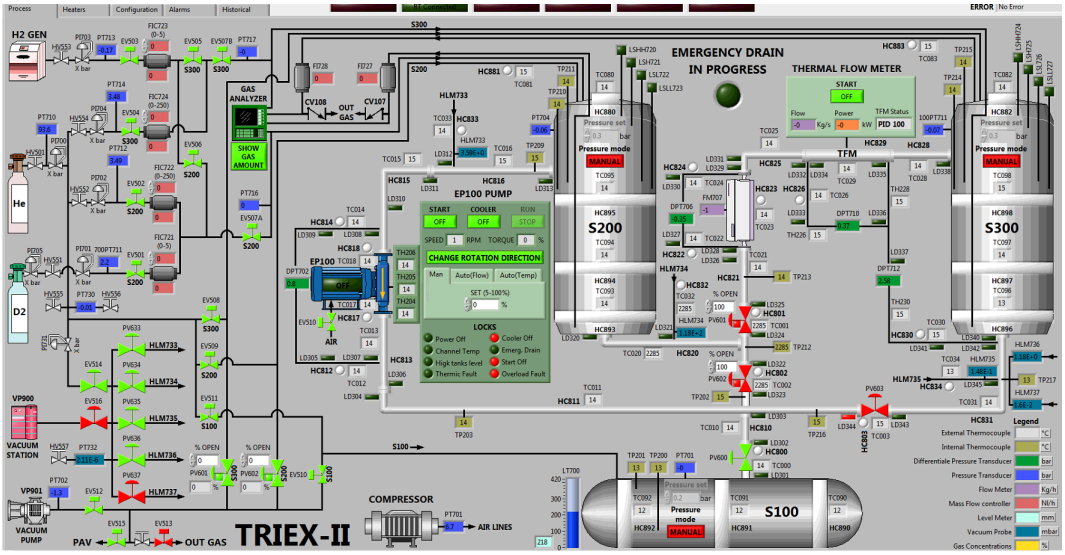

Figure 4.2. Main window of the DACS of TRIEX-II with GLC mock-up

4.1.2 Vacuum system

The vacuum system is divided in two subsystems. The first one uses a rotary vane pump to make vacuum in the LiPb loop. This system is necessary to remove any trace of oxygen before heating up the loop. Then, after 24 hours at 150 °C, vacuum is pumped again to remove the impurities that were desorbed by the pipe walls. Finally, the LiPb loading is performed under vacuum to allow the complete filling of the chambers of the hydrogen permeation sensors, which otherwise would remain partially filled by gas.

The second subsystem uses an integrated pumping station, composed of a diaphragm and a turbomolecular pump, to evacuate the hydrogen isotopes permeation

sensors, described in detail in the following. Each sensor is connected to the vacuum station by a 1/4" Swagelok line, on which a vacuum pressure transducer and a pneumatic valve are installed. The valve is used to isolate the sensor from the rest of the line during the measurements.

4.1.3 Gas and compressed air loops

The gas loop connects the gas cylinders (helium and helium + deuterium) and the hydrogen generator to the saturator and to the extractor. The gas stream is used to saturate LiPb in the saturator and as stripping gas in the extractor, when the Gas-Liquid Contactor mock-up is under testing. Each gas line is equipped with a relative pressure transducer, two valves and a mass flow controller. The mass flow controllers are used to mix desired flow rates of hydrogen (or deuterium) and helium. The inlet gas composition is analyzed by a mass spectrometer. The gas leaving the saturator and the extractor is brought to the mass spectrometer by other lines belonging to the gas loop, so that also the outlet gas composition can be measured. Each outlet line is equipped with a mass flow meter. The compressed air loop supplies the pneumatic valves and the cooling system of the permanent magnet pump.

4.2 Main Components

The main components of TRIEX-II facility are described in the following sections, except for the extraction component that, as it was said before, is the test section (GLC or PAV) and they are described in dedicated chapters.

4.2.1 Saturator

The saturator is a large vessel used to saturate hydrogen isotopes in LiPb by means of a mixed gas-liquid contactor system, consisting of a combined bubble column and packed column [71] with a filling of AISI 316 structured material, of the same type of the extractor (Sulzer MellapakPlus 452Y). The hydrogen isotopes are injected together with helium working as carrier gas. After passing through the LiPb column, the outlet gas flow rate is monitored by means of a mass flow meter. The inlet and outlet gas lines of the saturator have been conceived, manufactured and equipped with the same approach used for the extractor. The main design parameters are reported in Table 4.1.

4.2.2 Storage tank

The LiPb storage tank is used for storing all the LiPb contained in the circuit, including the one in the saturator, the extractor and the pipes, during the loading and draining phases of the system. The storage tank is equipped with:

- two internal thermocouples at different depths;
- a relative pressure transducer;

Table 4.1. Main dimensions of the Saturator

Parameter	Value	Unit
Design pressure	10	barg
Design temperature	530	°C
Max. operative temperature	500	°C
Nominal LiPb flow rate	1.2	kg/s
Saturator S200 flow rate	10-100	Nl/h
LiPb mass ow range	0.2-4-5	kg/s
LiPb Temperature	400-450	°C
He inlet Temperature	400-450	°C
Max. Q2 conc. in flow rate	5	vol. %
He pressure at the gas inlet	01-Mar	barg
Material	2 1/4 Cr-1 Mo	
Column internal diameter	154.1	mm
Total height	2.9	m
Bubble column height	765	mm
Structured packing height	426	mm
Surface-to-volume ratio	500	m^2/m^3
Void fraction packing	95	%

- a guided micro-wave level meter;
- three heating bands.

The eutectic LiPb was supplied by CAMEX in the form of $30\,cm^3 \times 7.5\,cm^3 \times 7.5\,cm^3$ ingots, with a minimum certificated purity of 99.5% (99.96% nominal). The ingots are melted under vacuum in a dedicated furnace then the liquid metal is discharged by gravity in the storage tank. A total of 156 dm^3 of LiPb is required to operate TRIEX-II, corresponding to 4 furnace loads. In order to verify the composition of the alloy after the loading phase, the eutectic point was checked analyzing the temperature evolution during the cooling down to ambient temperature of the LiPb in the storage tank. During the phase change from liquid to solid, the heat removed from the LiPb does not influence its temperature, which remains constant. Figure 4.3 shows the data measured by the storage tank thermocouples. It can be seen that the melting temperature is 235 °C, confirming the eutectic point of the liquid metal alloy.

4.2.3 Permanent magnets pump

The LiPb flow in the circuit is guaranteed by a permanent magnets pump, whose operating principle is based on the MHD effect [72]. This pump, manufactured by SAAS GmbH, must operate at a maximum operating temperature of 530 °C and is cooled by a proper cooling system with compressed air. The EP100 pump has two flanged 1" ASA 300 connections.

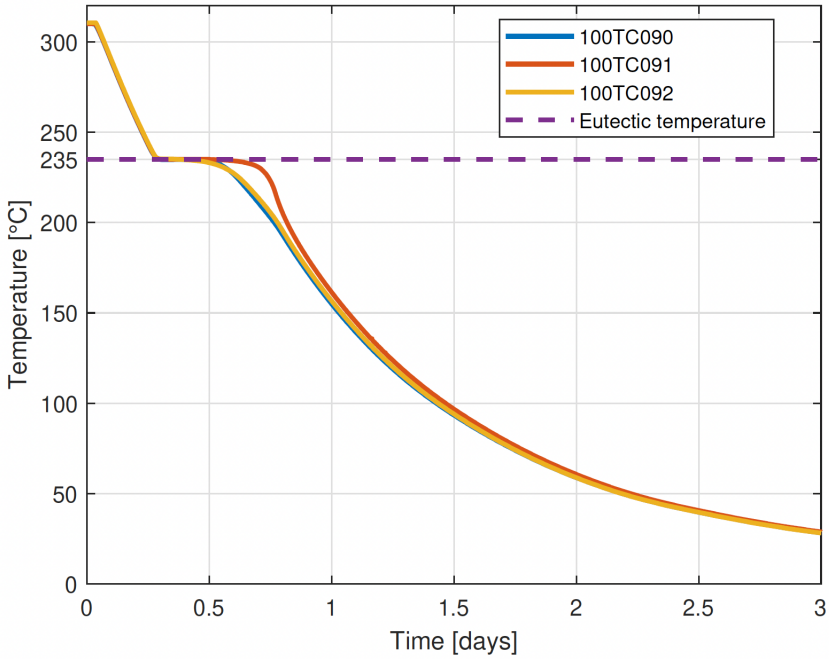

Figure 4.3. Temperature evolution during the cooling down of the LiPb in the storage tank measured by the thermocouples

4.3 Main instrumentation

The main instrumentation installed in TRIEX-II facility is described in the following paragraphs.

4.3.1 Hydrogen permeation sensors (HPS)

Hydrogen is dissolved by the saturator in LiPb at a certain concentration c_H in mol/m^3 and it is in equilibrium with a partial pressure $p_{H_2,eq}$ in Pa. ENEA, in collaboration with Politecnico di Torino, developed sensors dedicated to the measurement of hydrogen isotopes partial pressure [73],[74].

These sensors are called permeation sensors as they are based on the physical principle of permeability of hydrogen through a membrane. Hydrogen permeation sensors (Figure 4.4) is composed by a permeable helical-shaped pipe (Figure 4.5), closed at one end and immersed in the LiPb, a vacuum pressure transducer, a vacuum valve and a vacuum station (membrane pump + turbomolecular pump). TRIEX-II has three permeation sensors installed before the saturator (HLM-733), after the saturator (HLM-734) and after the extractor (HLM-735).

The measurement is made in three steps:

- vacuum is created inside the helix
- the helix is isolated with the vacuum valve
- due to the hydrogen permeation, the pressure inside the helix increases up to the equilibrium with the partial pressure in the LiPb

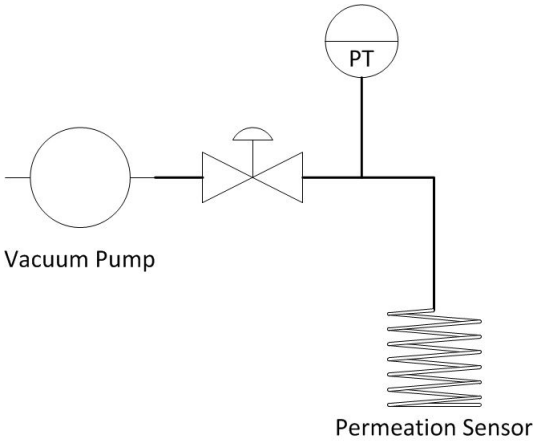

Figure 4.4. Sketch of HPS

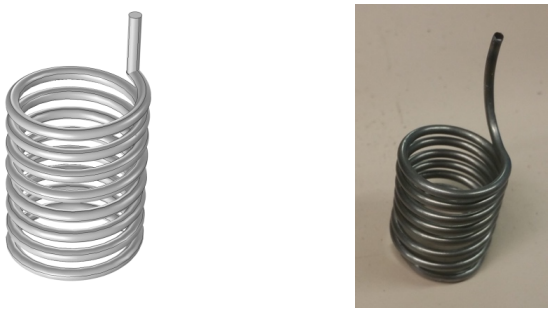

(a) **(b)**

Figure 4.5. Helical-shaped hydrogen permeation sensor

A medium vacuum (0.1-1 Pa) is reached at the start of the measurement to ensure the correct pressure gradient in order to allow the permeation through the membrane. An example of the trend of the pressure inside the HPS of two consecutive measurements is reported in Figure 4.6.

The sensors are made of iron (bcc), with a 99.5% purity, supplied by Goodfellow. The helical design allows to reduce the number of weldings, thus minimizing the problem of iron oxidation during the welding procedure and reducing the costs. The helical sensor is obtained by rounding a thin pipe around a cylindrical support.

In the first configuration, only two welds were performed: a butt weld at the bottom of the pipe, in order to close it, and an orbital weld at the top, in order to connect the helix with a 1/8" Swagelok pipe (and thus to its pressure transducer). Moreover, the three sensors installed in TRIEX-II were connected by a single vacuum line. The first configuration derives from dedicated sensitivity analyses [74] and the Process Flow Diagram is shown in Figure 4.7. The sensors were calibrated in gas and liquid phase at 400 °C and 450 °C. The calibration at 450 °C in liquid phase is shown in Figure 4.8. It is possible to observe that the three sensors achieved the equilibrium at the same partial pressure. The accuracy of the sensors is about 5% of the Full-Scale Output.

In the framework of this thesis, an upgrade of the sensors configuration was

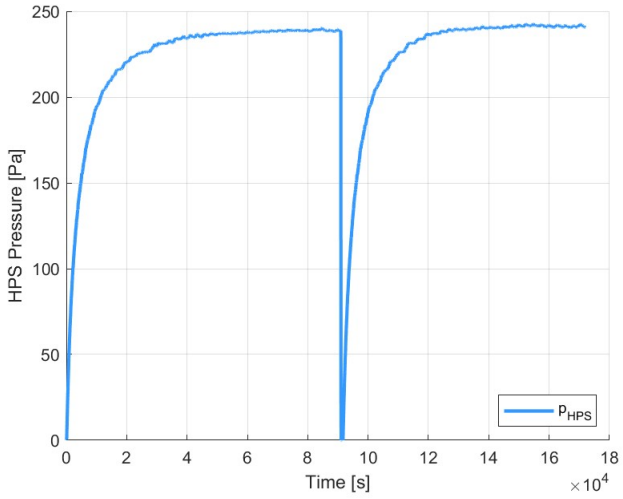

Figure 4.6. HPS pressure trend in two consecutive measurements

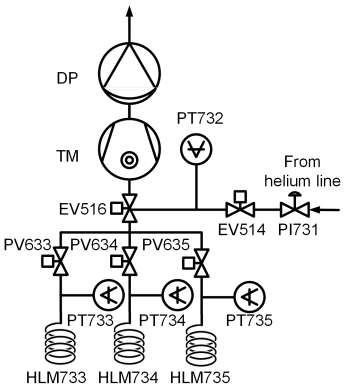

Figure 4.7. Process Flow Diagram of the first HPS configuration

made. New capacitive vacuum pressure transducers compensated in temperature and with CF (Con Flat) connection were installed (CMR 362 by Pfeiffer Vacuum). Moreover, considering the difficulties encountered with leakages in the vacuum line in the first configuration, each permeation sensor was equipped with its own vacuum station (HiCube80Eco by Pfeiffer Vacuum)and the whole line was welded by 5 Pascal S.r.l., except for the CF connection of the vacuum pressure transducer and the VCR connection of the valve (Diaphragm Sealed Valve by Swagelok). The new Process Flow Diagram (PFD) of the sensor lines is displayed in Figure 4.9. Moreover, each line was equipped with a heating cable and it is covered with insulation to perform the degassing. As the vacuum pressure transducer works at a maximum temperature of 45 °C the temperature of the CF connection is monitored during the start-up of the facility.

Due to the fact that the HPS are not able to discern between hydrogen and deuterium in the LiPb flow, when GLC mock-up is installed in TRIEX-II and deuterium tests are made, a different HPS configuration is installed. In each sensor line is added a quadrupole mass spectrometer supplied by Pfieffer, except for HLM

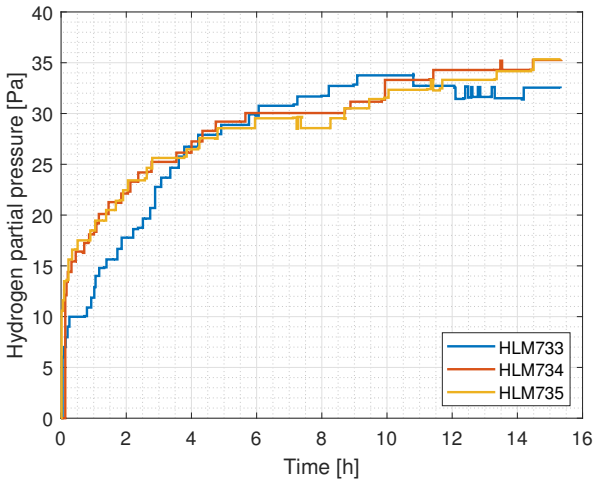

Figure 4.8. Permeation sensors pressure trend in flowing lithium-lead. LiPb mass flow rate $1 kg/s$, operative temperature 450 °C

733. Thanks to these instruments, it is possible to analyze the gas that permeate into the sensor and discriminate between hydrogen and deuterium. In addition, each line has a by-pass calibration line as shown in Figure 4.10. Using this configuration, the measurement is made in dynamic mode and not at the equilibrium: indeed, the quadrupole mass spectrometer installed works with a pressure lower than 10^{-3} Pa and it measure the hydrogen and deuterium flux that permeate into the sensor.

4.3.2 Quadrupole mass spectrometer

The quadrupole mass spectrometer is one of the most important instrument in the facility when GLC mock-up is installed because it allows to measure the concentration of hydrogen or deuterium in helium, thus allowing to close the mass balance of hydrogen isotopes. The quadrupole mass spectrometer is composed by an ion source, a mass filter (or quadrupole analyzer) and an ion detector. To work correctly, the vacuum chamber must be kept at about $5 \cdot 10^{-7}$ mbar.

Among different possible choices, the ESSCO GeneSys 200D gas analyzer was selected for TRIEX-II. One of the main advantages of this gas analyzer is that it is able to manage up to six inlets, thus allowing to analyze the inlet and outlet gases of the saturator and of the extractor. Moreover, it allows to choose between two measuring ranges: 1-200 amu and 1-5 amu. The latter is used when it is necessary to discriminate the deuterium (deuterium atomic mass: 4.0282 amu) and helium (helium atomic mass: 4.0026 amu) peaks, allowing to measure the deuterium and the HD concentrations in the stripping gas. The gas analyzer has been tested in order to check the capability to distinguish chemical compounds that have very similar molecular masses. The most important start up procedure are the background and the calibration, that in TRIEX-II are performed with nitrogen and with a set of calibrated cylinders of He+H_2 and He+D_2. The hydrogen concentration in the calibrated cylinder is in the range expected for the experiments. Figure 4.11 shows that the system is able to distinguish helium from deuterium.

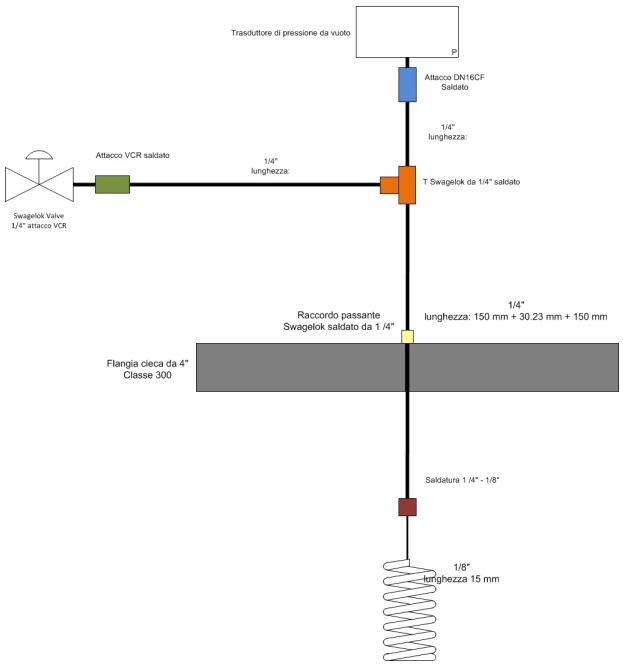

Figure 4.9. Process Flow Diagram of the upgraded HPS configuration

4.3.3 Leak detector

During the expermimental campaign with PAV mock-up, a leak detector (ASM 340 by Pfeiffer) is used to measure the permeated flux of hydrogen through the niobium pipes to the vacuum chamber of the component. In Figure 4.12 the sketch of the line that connects the leak detector to the vacuum chamber is shown. A calibrated leak (leak rate of $1.23 \cdot 10^{-4}$ mbar l/s by Vacuum Technology Inc) is used to calibrate the instrument and a vacuum pressure transducer is used to measure the pressure of the system when the gate valve isolates the vacuum chamber.

4.3.4 Thermal flow meter

A thermal mass flow meter is installed between the saturator and the extractor. This kind of instrument was designed by a joint collaboration between ENEA and Thermocoax, and it was characterized in IELLLO facility [70]. The LiPb goes out from the bottom of the extractor and goes back to the pump. A bypass proportional valve is installed above the extractor, with the aim of allowing the draining of the pipe between the saturator and the extractor itself. This valve permits, in addition to the regulation provided by the pump, to control the LiPb flow rate; the measurement is given by the mass flow meter, which enters the extractor. The thermal mass flow meter is a particular type of flow meter based on enthalpy balance, described by the following equation:

$$W_{hb} = m \cdot cp \cdot (Tout - Tin) \tag{4.1}$$

where:

- W_{hb} in W is the power supplied by a heating bulb;

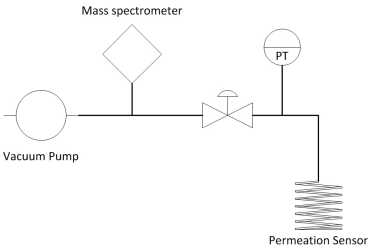

(a) Simplified sketch of the sensor line

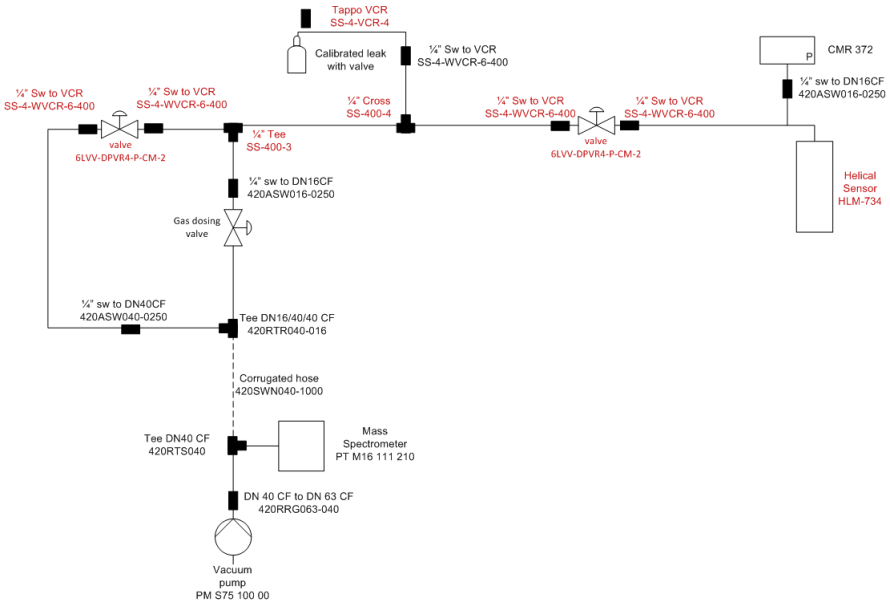

(b) Complete P&ID of the sensor line

Figure 4.10. HPS configuration for dynamic mode measurement

- m in kg/s is the LiPb mass flow rate;
- c_p in J/kg K theLiPb specific heat;
- T_{out} and T_{in} in K are the temperatures measured by two PT100 sensors, respectively.

As displayed in Figure 4.13, the LiPb enters the instrument and its temperature is measured. Then, it is heated by the bulb, blended by the static mixer and finally its temperature is measured again. Two PT100 sensors are used to measure the temperature.

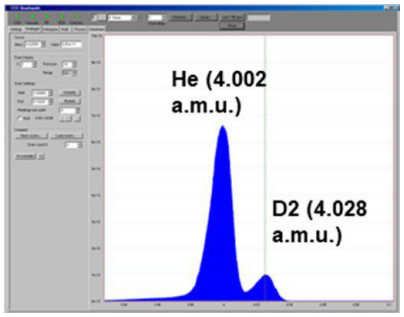

Figure 4.11. Acceptance test for EES GeneSys 200D: two distinct peaks for He and D_2

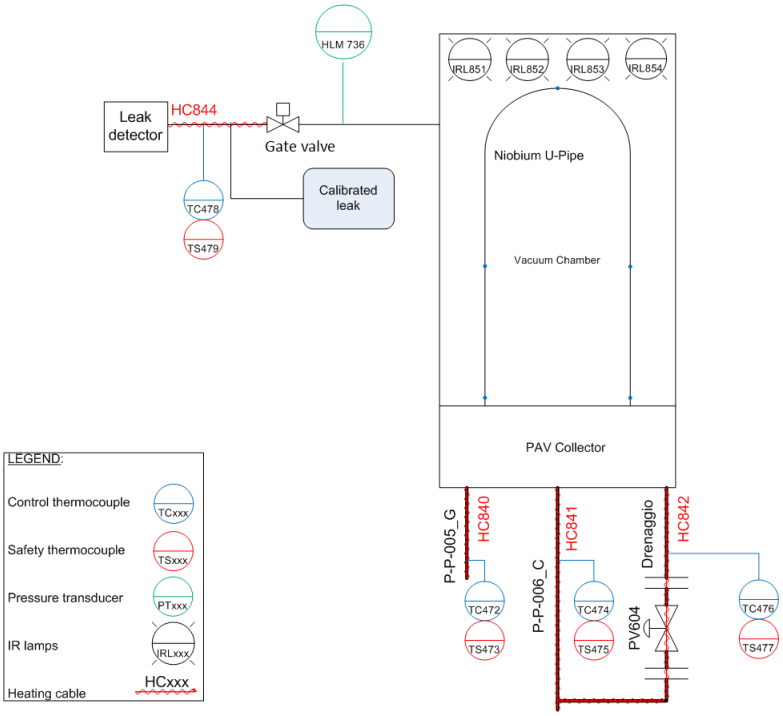

Figure 4.12. Sketch of PAV mock-up leak detector line

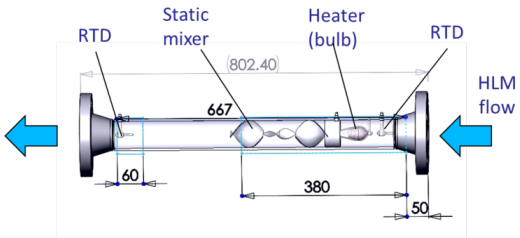

Figure 4.13. Sketch of the thermal mass flow meter

Chapter 5

PAV-ONE mock-up

As said in Chapter 3 two configurations and two membrane materials are currently investigated as main alternatives, within EUROfusion project: planar or cylindrical configuration and niobium or vanadium materials.

The planar configuration with vanadium membranes is being investigated in CIEMAT laboratories [48].

PAV-ONE is the first PAV mock-up to be built with relevant dimensions and materials and tested in LiPb in the world and, in this section, its enginering design, manufacturing and experimental campaign are described.

In this work, niobium was selected as membrane material for the mock-up because of its high permeability [75] and for its lower cost compared to vanadium (at the time of writing the vanadium price is about 3 times higher than that of niobium). Moreover, this choice was also motivated by the lower tendency to oxidation of niobium with respect to vanadium, as it can be seen in Ellingham diagram (i.e. standard free energy of formation of important oxides as a function of the temperature) [76]. Oxidation would reduce the hydrogen isotopes permeation flux [77].

Regarding the configuration, the cylindrical one was chosen in this work to minimize the welding area, the volume/area ratio and the membrane thickness while preserving a high theoretical extraction efficiency. This configuration minimizes the welding area with respect to the planar configuration because only the ends of the pipes have to be welded, while, using plates, the entire profile as to be welded in order to create a channel. Moreover, using U-pipes and a single collector, it is possible to make a double passage of the LiPb inside the vacuum chamber, making half of the welds. Using circular pipes instead of rectangular ducts, allows to adopt a lower thickness to withstand the operative loads. A lower thickness enhances the tritium permeation through the membrane. Therefore, in the selected design, the LiPb flows, in two passage, through 16 niobium “U” shaped pipes installed in a vacuum chamber and welded to an F22 plate (10CrMo9-10, ASTM A182 Grade F22), as shown in Figure 5.1.

The conceptual design of this mock-up was made by ENEA and Politecnico di Torino for the WCLL BB [78], while the engineering design was carried out in the framework of this thesis to adapt the mock-up to the size of TRIEX-II facility. Additional thermal-hydraulic simulations were carried out by Politecnico di Torino,

Figure 5.1. View of PAV mock-up

supporting the engineering design [49].

The efficiency of the PAV is defined as [71]:

$$\eta = 1 - \frac{C_{out,PAV}}{C_{in,PAV}} \tag{5.1}$$

where, $C_{in,PAV}$ is the hydrogen isotopes concentration at the inlet of the PAV mock-up, while $C_{out,PAV}$ is the hydrogen isotopes concentration at the outlet of the PAV mock-up. In Equation (5.1), $C_{in,PAV}$ is an input parameter depending on the tritium production rate in the reactor, while $C_{out,PAV}$ depends on the PAV design. This chapter descusses the engineering design of the PAV mock-up, with particular attention devoted to the solutions to two challenges of the project, namely:

- The manufacturing process and, in particular, the best solution to perform the niobium-F22 joining between the pipes and the plate.
- A heating strategy that does not disturb the tritium diffusion through the niobium membrane, allowing at the same time to keep the temperature at the rated value. The use of conventional heating cables was in fact prevented as they would reduce the permeation area, also adsorbing hydrogen.

5.1 PAV mock-up description

The geometrical description of the mock-up, the selected instrumentation and the strategy to join F22 and Nb are reported in this section. Figure 5.2 shows to picture of the component that was obtained as a result of the positive conclusion of these activities.

5.1.1 Geometrical description

Geometrically, the PAV mock-up is structured as a tube-and-shell heat exchanger, obtained simplifying the design proposed in [31], see Figure 5.3a.

The PAV mock-up is composed by a cylindrical vessel with 16 niobium U-tubes, the membranes for hydrogen permeation, welded on a F22 plate. This material has been chosen for his corrosion resistance in LiPb environments. Vacuum (about 1 Pa) is pumped in the vessel while the LiPb flows in the niobium pipes. The LiPb is distributed into the niobium pipes by a collector which constitutes the lower part of the PAV. The collector is divided in three parts; each part is connected with one pipe in P22 (10CrMo9-10, ASTM A335 Grade P22), which connects the mock-up with the LiPb loop of the facility. The three pipes are:

- the inlet pipe;
- the discharge pipe;
- the outlet pipe.

The inlet pipe is connected with the part of the collector that allows the LiPb distribution in the first 8 niobium pipes. This part is indicated in red in Figure 5.3b. The discharge pipe is connected with the part of the collector (called mixing collector) where the LiPb coming out from the first 8 niobium pipes mixes. From this section of the collector, indicated in yellow in Figure 5.3b, the LiPb is distributed in the remaining 8 niobium pipes. The discharge pipe is needed to allow the gravity draining of the mixing collector. The outlet pipe is connected with the section of the collector, indicated in red in Figure 5.3b, where the LiPb coming out from the last 8 niobium pipes mixes before leaving the mock-up. Therefore, LiPb will double pass through the vessel, as shown in Figure 5.3c and Figure 5.3d. The main dimensions of the mock-up are reported in Table 5.1, while the operative conditions are in listed in Table 5.2.

The cylindrical vessel is divided into two parts so that the upper part can be removed to inspect the Nb pipes or for maintenance. The two parts are joined together by a flange. The upper part is connected to the gas and vacuum line and hosts two feed-through connectors (in red in Figure 5.4a) for the power supply of the heating systems of niobium pipes (infrared (IR) lamps, in yellow in Figure 5.4a), which are attached inside the vessel. In this way, when the upper part of the vessel is lifted, the heating systems will also be lifted. Moreover, the upper part of the vessel is equipped with a quartz porthole to allow the visual inspection of the tube bundle also during operation. Quartz has been chosen for its impermeability to hydrogen isotopes [79].

(a) *Picture of the niobium tube bundle*

(b) *Picture of the component before the installation in TRIEX-II*

Figure 5.2. Pictures of the PAV mock-up at the end of the manufacturing

Table 5.1. Main dimensions of the PAV mock-up

Dimensions	Value
Height of the vessel	1106.00 mm
External diameter of the vessel	323.85 mm
Thickness of the vessel	6.35 mm
Length of the Nb pipes (including the portions welded in the plate, 30 mm on each side)	1805.25 mm (S) 1899.50 mm (M) 1993.74 mm (L)
External diameter of the Nb pipes	10.00 mm
Internal diameter of the Nb pipes	9.20 mm
Surface exposed to LiPb flow	0.42 m^2
Pitch of the Nb pipes	30.00 mm
Height of the LiPb collector	156.00 mm
Thickness of the plate	38.00 mm
External diameter of the P22 pipes (inlet/outlet LiPb)	33.40 mm
Thickness of P22 pipes (inlet/outlet LiPb)	3.38 mm
External diameter of the draining pipe	21.34 mm
Thickness of the draining pipe	2.77 mm

Table 5.2. PAV mock-up operative conditions

Parameter	Value	Unit
Operative internal pressure of the vessel	$10^{-1} - 10^{-5}$	Pa
Max internal pressure of the vessel	$1.1 \cdot 105$	Pa
Max internal pressure of the Nb pipes	$4 \cdot 105$	Pa
Max internal pressure of the LiPb collector	$5 \cdot 10^5$	Pa
Max temperature of the collector	530	°C
Max temperature of the Nb pipes	500	°C
Max temperature of the vessel	100	°C
Operative LiPb temperature	$350 - 500$	°C
Max speed of LiPb in the Nb pipes (at 4.6 kg/s)	0.97	m/s
Total flow rate of LiPb in the Nb pipes	0.2-4.6	kg/s
Vessel filling gas (during long stops)	Helium	-

Instead, the lower part of the vessel has two thermocouple feed-through connectors (in blue in Figure 5.4a), as 50 thermocouples are needed to monitor LiPb temperature in the 16 Nb tubes. The tube plate is wide enough to work also as upper flange of a connection with the collector. Instead, the lower part of the vessel is directly welded on the tube plate, as shown in Figure 5.4b.

As shown in Figure 5.2, a total of 16 pipes have been bended to be used in the PAV mock-up for TRIEX-II facility. Niobium shows a high ductility and it is not difficult to shape the channels using a bending jig and filling the pipes with sand. The bending process has to be slow and continuous to avoid the deformation of the pipe internal side in contact with the jig. Moreover, duct tape was utilized to protect the contact zone between the pipe and the bending jig during the hand bending.

5.1.2 Joining niobium and F22 steel

The most important issue to be solved in order to manufacture the PAV mock-up was to perform the joining between the niobium pipes and the F22 plate, as there

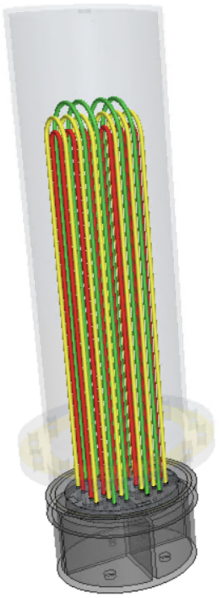

(a) *16 niobium U-tubes: Long pipes (L) in green, medium-length pipes (M) in yellow and short pipes (S) in red*

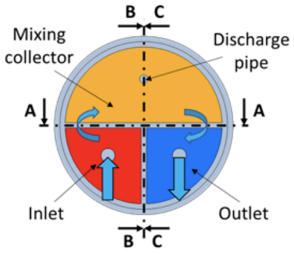

(b) *Horizontal section of PAV mock-up collector showing its 3 parts and the connecting pipes*

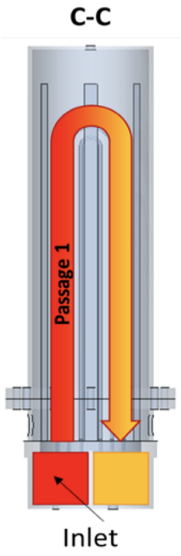

(c) *First passage of LiPb through the vessel*

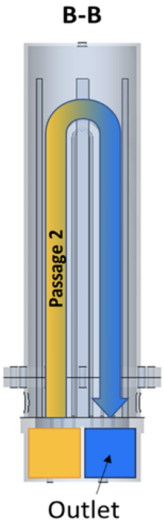

(d) *Second passage of LiPb through the vessel*

Figure 5.3. Sketches of the PAV mock-up

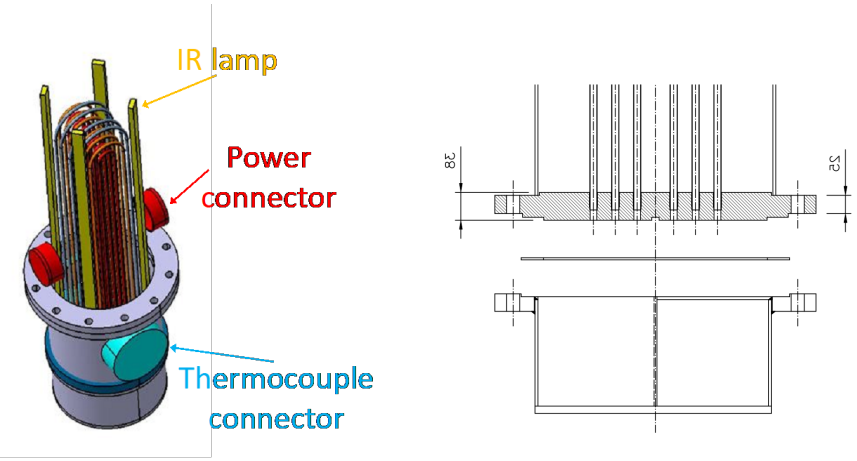

(a) *View of PAV mock-up connectors and IR lamps* **(b)** *Detail of the connection between F22 plate with the collector*

Figure 5.4. PAV mock-up details

are three main problems to be solved:

- niobium easily oxidizes at high temperatures;
- the melting points of niobium (2469 celsius) and F22 (about 1320 celsius-1390 celsius) are very different, so that performing a welding is really difficult;
- most of the brazing alloys are made of materials that are highly soluble in LiPb, such as nickel.

The solution proposed and adopted on PAV-ONE to join the niobium pipe with the F22 plate is to use a vacuum brazing based on a nickel-based brazing alloy. The vacuum brazing avoids the oxidation of niobium, while, to prevent nickel from solubilizing in LiPb, the brazing procedures are carried out in such a way that avoids the contact between the filler material and the LiPb. The brazing was performed on almost the entire depth of the plate in order to create a strong joint between the two materials. The brazing alloy can withstand up to 1100 °C, about 600 °C higher than the operative condition of the mock-up. Each brazing, after the experimental campaign, will be later inspected with not destructive testing (radiography).

However, a testing joint has also been assessed with destructive testing before starting the manufacturing, as the brazing of these materials has never been performed earlier.

A thermal analysis of the mock-up, performed by Politecnico di Torino [49], demonstrated the necessity of additional heating systems to keep constant the temperature of the niobium pipes. For this reason, infrared (IR) lamps were installed in the vessel.

Given the prototypical nature of this technique, sample joints were realized with the specific purpose of testing their resistance and the overall quality of the postulated solution. Visual examination and pressure tests were performed on some samples to control that the joints were well made. Tests were carried out with

(a) *Detail of the stereoscope analysis*

(b) *Picture of two pressure test samples*

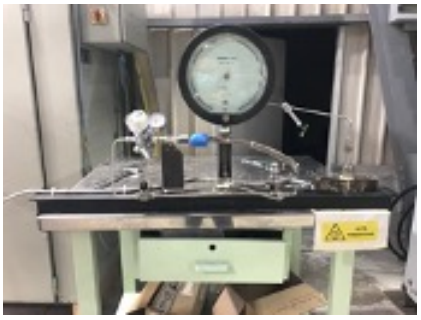

(c) *Pressure test device*

Figure 5.5. Examination and testing of the joining solution

high pressures up to 24 bar at 25 °C with helium (24 bar is the equivalent pressure at room temperature of 1 bar and 480 °C, according to the Pressure Equipment Directive). These tests were repeated with 3 different samples. All the 3 samples withstood this pressure. Moreover, a visual examination of all the welded pipes was made and all the joints met the requirements of international standards, such as ISO 18279. Figure 5.5 shows a detail of the stereoscope analysis, the pressure test device and two samples of the Nb pipe joined with the F22 plate.

A metallographic investigation with Scanning Electron Microscopy (SEM) was carried out on two cross sections of two different pipes (Figure 5.6). The metallographic analysis showed that the brazing alloy has a good pocket between the plate and each pipe and an excellent penetration. Moreover, the analyses showed a structural cohesion of about 12 microns between the brazing alloy and the walls of the tube and of the flange. High quality cohesion leads to higher mechanical performances.

In addition, the metallographic analysis revealed just isolated micro porosities in the middle of the brazed section. The largest size of the porosity found during the inspection does not exceed 0.16 mm. If we consider the brazing area in the section

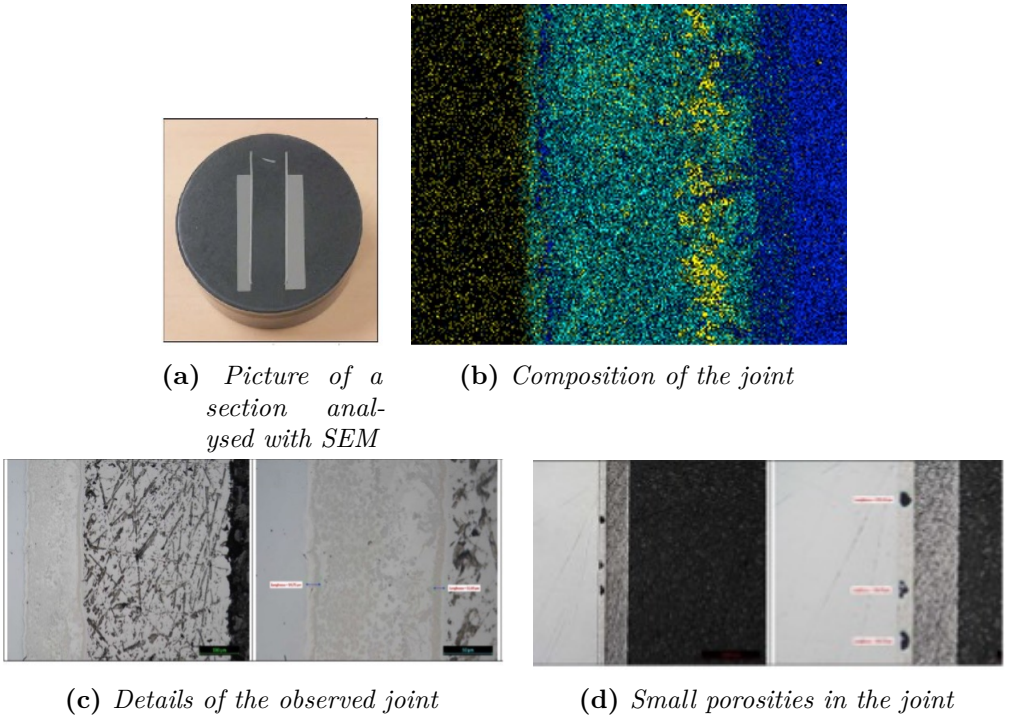

(a) *Picture of a section analysed with SEM*

(b) *Composition of the joint*

(c) *Details of the observed joint*

(d) *Small porosities in the joint*

Figure 5.6. SEM analysis of the Nb-P22 joint

(about 1 square millimeter) the presence of these defects affects only 1.5% of the cross section. Therefore, it is considered that this type of isolated defect does not affect the overall performance of the joint. With reference to ISO 18 27 9 level B, the limit of acceptable porosity is 20% of the projected area.

Non-destructive testing

One of the most important issues to deal with in the manufacturing of the PAV for DEMO is the inspection of the brazed joints between the pipe in niobium and the support plates.

NDT (Nondestructive Testing) refers to a group of inspection methods that allow inspectors to evaluate and collect data about a material, system, or component without permanently altering it. The goal of NDT is to ensure that critical infrastructure is properly maintained in order to avoid accidents. Welding and brazing connections may fail if not created to proper specification (e.g. welding temperature, cooling rate and compatible materials for the joint). The typical welding/brazing defects are:

- lack of fusion of the welding/brazing to the base metal;
- cracks or porosity inside the welding/brazing;
- variations in welding/brazing density.

These could cause the joint to fail.

The methodologies of NDT are divided in two groups: volumetric and superficial. The former highlights defects in the entire volume of the component, while the latter only shows defects on or near the surfaces (e.g. liquid penetrant testing (PT), visual inspection (VT), magnetic particle testing (MT) and eddy current testing (ECT)). The techniques that can be used in the PAV application are the volumetric ones:

- Ultrasonic NDT (UT),
- Radiography NDT (RT),
- Acoustic Emission NDT (AE),
- Infrared and thermal NDT (TIR).

However, the visual inspection is important because it is the only one that verifies also that the joint geometries are compliant with the designed ones.

The volumetric methodologies, in turn, are divided into transmission and reflection ones. The radiography NDT is a transmission method: the rays have to pass through all the material to be detected on the other side by a sensor. The ultrasonic NDT is a reflection method, but sometimes they can be used also in a transmission way. Acoustic emission and infrared and thermal NDT are classified separately, because they are based on energy emission by the material. The advantage of transmission methods is a low attenuation of the signal, but they need an accessible material on both sides of the sample.

The main challenge to face in the PAV application is the small diameter of the niobium pipes and of the defects to detected. The results of the SEM analyses of the first brazing samples showed that the main defects had dimensions lower than 0.2 mm and, considering the brazing area in the section (about $1\,\mathrm{mm}^2$), the presence of these defect affected only 1.56% of the cross section.

Currently, the most common kind of NDT used in the inspection of components having a shell and tubes heat exchanger design is the ultrasonic NDT. In this process high-frequency sound waves are transmitted into a material to find variations in the properties. Pulse echo is a common technique to perform ultrasonic testing and consists in measuring the echoes coming from imperfections towards the receiver.

The method proposed for the PAV application is the Multigroup Phased Array Ultrasonic Testing (PAUT). In these instruments, many rectangular crystals are placed in a row and they emit ultrasonic waves. These waves travel into the material and, only in presence of defects, are reflected back to the sensors. The use of several crystals allows to have a very accurate analysis and a fast inspection speed.

5.1.3 Heating system for the niobium pipes

The heating strategy adopted to keep the LiPb at the rated temperature and to avoid disturbing the tritium diffusion through the niobium membrane is described in this section. The use of heating cables as heating system would not only be difficult for the installation, since the number of pipes is high compared to the dimensions of the component, but also the presence of the cables would create an additional obstacle to the diffusion of tritium through the Nb membrane. For these reasons, a different solution is proposed.

The heating system of the niobium pipes consist of 4 double-tube infrared lamps mounted inside the vessel. The lamps are made of quartz, a material that prevents hydrogen permeation, so that their presence do not affect the measurement of the permeated flux [79]. The lamps allow to keep the temperature of the niobium pipes at about 450 °C to avoid the solidification of the LiPb inside the pipes. The lamps, 100 cm long and positioned symmetrically with respect to the center, have a maximum power of 3.5 W/cm, they are 100 cm long and they have an angle of action of 60°. A sketch of a lamp is shown in Figure 5.7, together with the positions of the 4 lamps in the PAV vessel. Figure 5.8 shows a picture taken from the quartz porthole during operation: two of the lamps are simultaneously switched on (indeed, the control system switches on and off the lamps according to the temperature of the tubes) and allow a perfect vision of the niobium tubes.

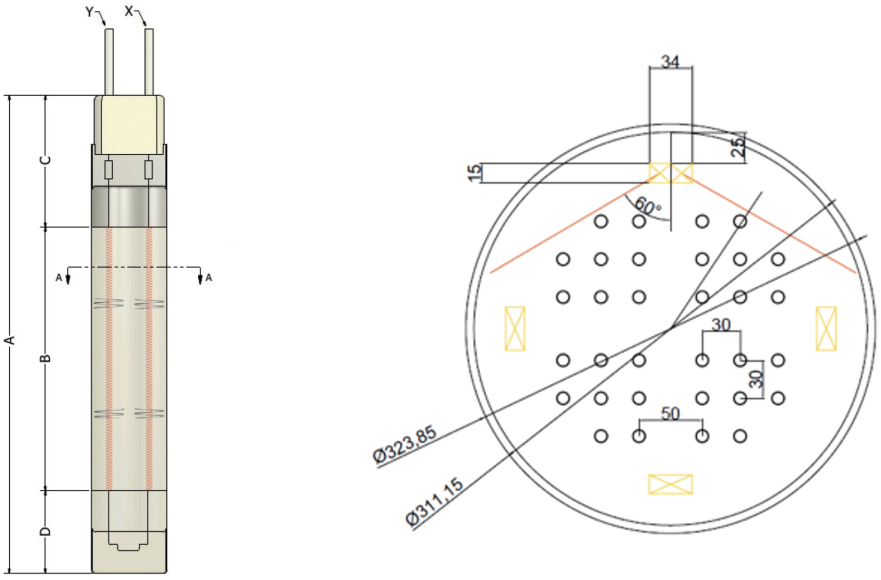

Figure 5.7. Sketch of an IR lamp and PAV mock-up technical drawing, horizontal section of the vessel showing the IR lamps position and their angles of action

5.1.4 Mock-up instrumentation

One of the main aims of the PAV mock-up was to quantify the hydrogen permeation flux through a 0.4 mm thick niobium pipe with flowing LiPb inside and under different working conditions. To this end, a helium leak detector (ASM340 series by Pfeiffer Vacuum) is connected to the vacuum side of the PAV vessel through a 3/4" vacuum-tight Swagelok line. A flexible hose with DN40 is used to avoid any stress to the instrument connection. The instrument performs an integral measurement of the permeated hydrogen, from which it is possible to evaluate the average permeation flux per unit area. This value will be used as a reference for the results of numerical models. The leak detector is equipped with a rotary vane pump with 15 m^3/h backing pump capacity and a hybrid turbo/drag vacuum pump (53 l/s). It has a minimum detectable rate as low as $5 \cdot 10^{-12}$ mbar l/s.

Figure 5.8. Picture of the niobium tubes from the porthole installed on the top of the PAV vessel. The lamps are on and illuminate the tube bundle.

Heating cables and bands are used to heat up the collector and the P22 pipes that connect the collector to the facility, to maintain the LiPb that flows in the niobium pipes at 450 °C. In order to control the niobium pipes temperature, 50 thermocouples are installed at different heights on the pipes. In order to insert the thermocouples in the vessel while preserving the vacuum tightness, feed-through vacuum connectors by Vaqtec were selected with a market survey and six of them were welded to two dedicated nozzles (three per nozzle). Each pipe is equipped with two thermocouples at the inlet and outlet. Additionally, six pipes have one more thermocouple at the top of the U-bend and two more at half height. These six pipes were chosen in order to have a good mapping of the temperature in the various positions, taking advantage of the cylindrical symmetry.

5.2 PAV Commissioning tests

Before starting the experimental campaign with PAV, commissioning tests were carried out. These tests are divided in two typologies: pressure and vacuum tests. All the tests were repeated twice, once at ambient temperature and once at 450 °C.

The first test was a pressure test of the LiPb loop at about 50 °C. The loop was filled with helium at 1 barg. After about 4 days the pressure decreased of about 0.3 bar (leak of 0.12 mbar l/s), as shown in Figure 5.9. Then, the temperature was raised to 350 °C and the test was repeated, giving very similar results as shown in Figure 5.10. After the two tests, the sealing of the loop was considered satisfactory for the needs of the experimental campaign.

A different test was devoted to check if the permeation sensors were able to

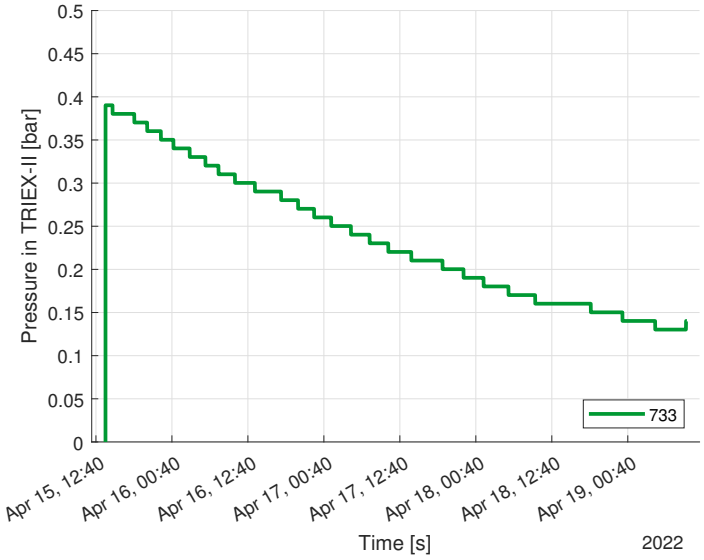

Figure 5.9. Pressure decrease during the test in cold conditions (50 °C)

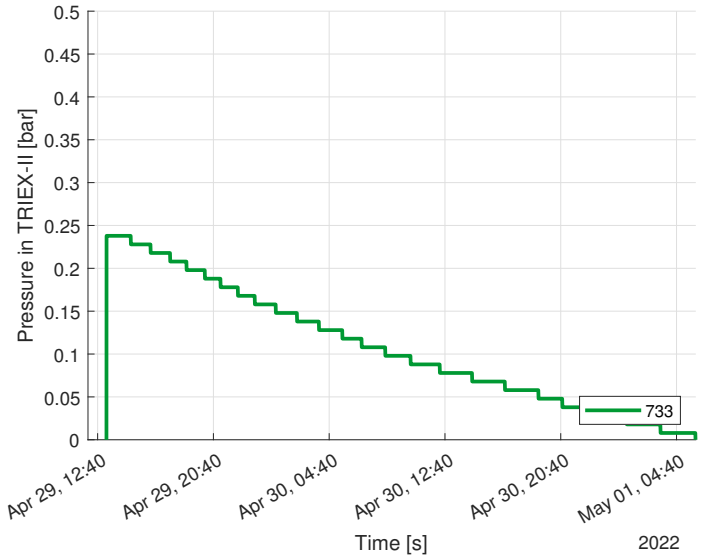

Figure 5.10. Pressure decrease during the test in hot conditions (350 °C)

reach a steady state or continue to increase due to leakages from the environment. Figure 5.11, Figure 5.12 and Figure 5.13 show that they do not have any leakage and are able to reach a constant value. At the end of the commissioning tests,

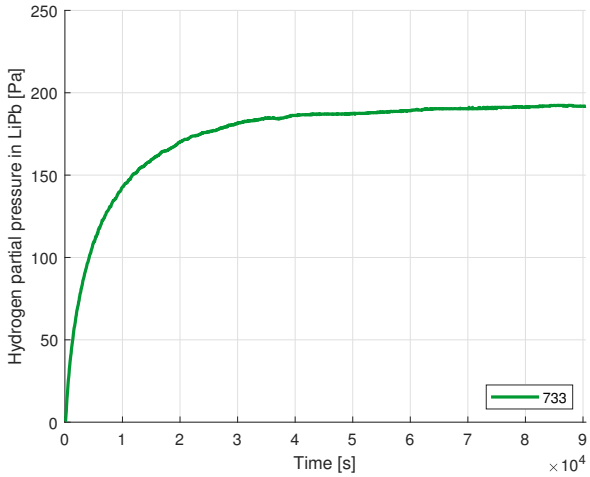

Figure 5.11. Commissioning test for sensor HLM733, located upstream of the saturator

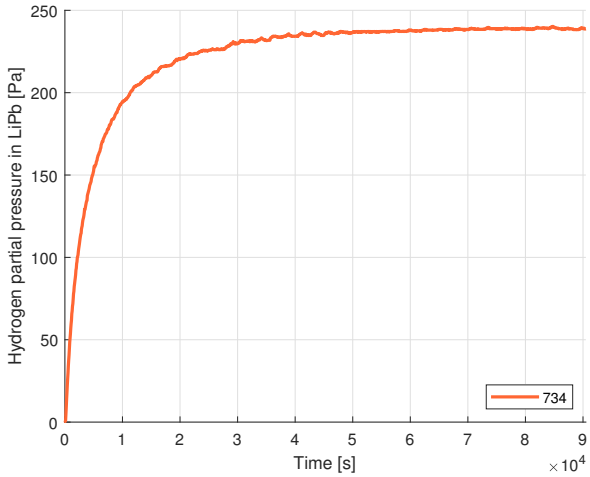

Figure 5.12. Commissioning test for sensor HLM734, located downstream of the saturator

calibration of the leak detector was performed with a calibrated leak of $1.23 \cdot 10^{-4}$ mbar l/s. The calibration was repeated every day during the campaign to be sure to have a reliable measurement from the instrument.

Finally, TRIEX-II was loaded.

5.2.1 TRIEX-II loading procedure with PAV mock-up

TRIEX-II loading procedure follows these steps:

- close helium injection valve EV507A (this valve is usually kept open to prevent the obstruction of the injection line in the saturator);

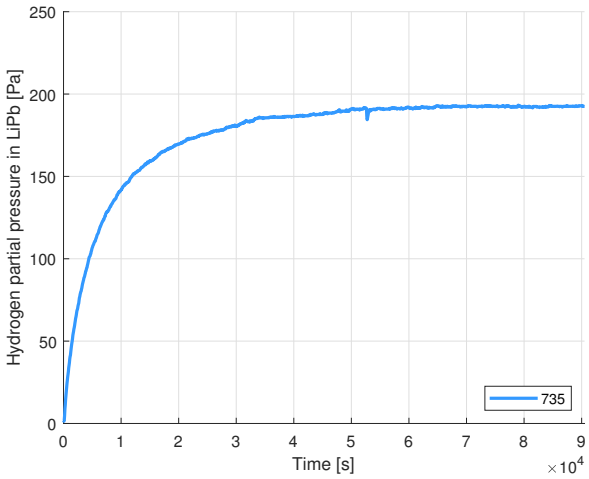

Figure 5.13. Commissioning test for sensor HLM735, located downstream of the extractor

- set the pressure control system to "automatic" and its discharge pressure to 1 barg;
- set the pump speed to 80% and the rotation direction to "clockwise" (upwards in the control system);
- check that the gas discharge valve PV602 is closed and the EV513 is open;
- check that the loading valve PV600 is closed;
- pump vacuum in the loop until it reaches about 0.1 mbar;
- open valve PV600;
- start increasing the pressure in the storage tank dome, while checking the loading by monitoring the temperature in the different parts of the loop;
- stop the permanent magnet pump when the LiPb reaches the bottom of the saturator (variation of the temperature measured by TC020 and TC093). From this moment until the end of the loading procedure it is important to keep an eye on the temperature in the pump channel, as it is heated only by the Joule effect, and to be as quick as reasonable with the remaining steps;
- start helium injection in the saturator at low flow rates (about 10 Nl/h);
- continue to increase the pressure in the storage tank dome until TP209 measures a change in the temperature (at this time all the HPS chambers are filled with LiPb);
- stop the vacuum pump, close valve on the vacuum line and increase the helium injection to 250 Nl/h (maximum allowed by the mass flow controller; the aim is to reach 1 barg as fast as possible);

- continue loading LiPb until the high level in the saturator switches on (LSH721) while the pressure in the saturator is 1 barg (if the two conditions are not met simultaneously, start alternating the injection of helium and the loading of LiPb until they are met);
- close the loading valve PV600, the PAV mock-up draining valve PV604 and the bypass valve PV602;
- switch on the permanent magnet pump and check if circulation is established (the thermal mass flow meter should measure a mass flow rate);
- reduce the helium flow rate to 30 Nl/h.

5.3 Test matrix and procedure of the experimental campaign

The hydrogen partial pressure in LiPb at the first load was more than 5000 Pa and then, extracting mainly by the PAV mock-up, it decreased reaching 170 Pa, condition of the first test. In Figure 5.14 part of the extraction is shown (up to about 620 Pa).

The final test matrix, with the tests that were really performed, is reported in Table 5.3.

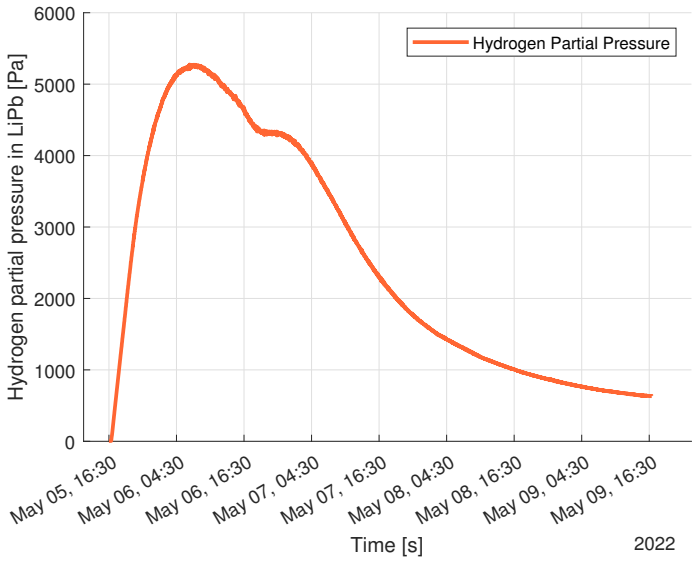

Figure 5.14. Hydrogen partial pressure decrease during the commissioning of TRIEX-II: after a partial pressure of about 5200 Pa was measured by the HPS, the PAV started to reduce it towards values suitable for the experimental campaign

The tests were carried out as reported in the following.

First of all, a mix of hydrogen and helium is fluxed in the saturator to maintain constant the concentration of the test.

Table 5.3. Test matrix of the PAV mock-up experimental campaign

Test	p_{in} [Pa]	Measure	Start date	Start time	End date	End time
1	170	1	15/07/22	15:00	15/07/22	20:00
		2	17/07/22	02:00	17/07/22	08:00
2	240	1	20/07/22	03:00	20/07/22	10:05
		2	21/07/22	05:00	21/07/22	11:30
		3	22/07/22	00:00	22/07/22	10:10
		4	23/07/22	06:00	23/07/22	12:00
3	360	1	27/07/22	01:30	27/07/22	09:50
		2	28/07/22	06:00	28/07/22	13:55
		3	29/07/22	11:00	29/07/22	14:25
4	110	1	01/08/22	09:40	01/08/22	13:40
		2	02/08/22	06:50	02/08/22	10:25
5	130	1	03/08/22	14:20	03/08/22	17:35
		2	04/08/22	08:10	04/08/22	10:15
6	184	1	06/08/22	22:00	07/08/22	16:15
		2	09/08/22	11:00	09/08/22	16:45
7	226	1	11/08/22	10:30	11/08/22	15:25
		2	12/08/22	12:55	12/08/22	13:52

The concentration in LiPb reaches a value lower than the concentration in the gas, as the equilibrium value is a balance between the quantity of solubilized and extracted hydrogen.

This operation was chosen as it makes the measure independent of the time and to use the Sievert's constant in the mass balances (Equation (2.67) is applicable only at the equilibrium). Indeed, if the saturator does not compensate the extraction of the PAV, the value measured by the sensors should start to decrease, due to the counter permeation from the sensor chamber to LiPb, that is a slow process. Moreover, in the same instant the three sensors measure three values of concentration in three different LiPb volumes and, therefore, a time lag exists between the sensors during the transient phase. This difference is related to the time needed for a volume of LiPb to travel from a sensor to the other. To extrapolate the value of the same LiPb volume, the exact time that the alloy needs to circulate should be estimated.

For these reasons and to reduce uncertainties, the stationary method described above has been chosen for this campaign, maintaining the partial pressure at the inlet of the PAV constant. This method allowed to have more accurate data.

The mix of hydrogen and helium injected in the saturator is made with mass flow controllers, instruments that regulate the mass flow rates of each gas following the operator needs. The calculation is the following:

$$p_{H_2} = \frac{G_{H_2}}{G_{He}} \cdot p_{injection} \tag{5.2}$$

where:

- p_{H_2} is the injected hydrogen partial pressure in Pa
- G_{H_2} is the hydrogen flux

- G_{He} is the helium flux
- $p_{injection}$ is the pressure measured by a pressure transducer installed downstream of the mass flow controllers in Pa.

For instance, when an injected hydrogen partial pressure of 300 Pa is required, a fixed hydrogen flow rate of 0.1 Nl/h is imposed and knowing that the gas pressure downstream of the mass flow controllers is about 3.13 bar, the helium mass flow controller has to be set to about 104 Nl/h.

When the hydrogen partial pressure becomes constant, 3 kind of measures are carried on:

- partial pressure measurement with Hydrogen Permeation Sensors (HPS) at the inlet and the outlet of PAV mock-up
- permeated flux with the Leak Detector (LD)
- pressure increase in the PAV mock-up vessel

The HPSs positioned in LiPb loop at the inlet and at the outlet of the PAV mock-up measure different partial pressures, as Figure 5.15 shows. This difference is due to the PAV mock-up extraction. The hydrogen partial pressure at the outlet of the PAV mock-up is measured twice: indeed, 2 HPSs are installed in two different positions as explained in Chapter 4 (Figure 5.16). The LD is set to detect hydrogen and it measures the flux that permeates through the niobium tubes. Moreover, an additional indirect measurement of the flux is performed by isolating the vessel of the PAV mock-up by means a specific gate valve (pressurization test). The pressure inside the vessel increases and, knowing the initial pressure, the final pressure and the duration of the pressurization it is possible to calculate the flux of hydrogen that permeates through the niobium tubes. This calculation has some uncertainties due to the use of an average temperature of the system vessel+vacuum line, but it is used to have a verification of the leak detector measurement. From the pressure increase (Figure 5.17) it is possible to calculate the permeation rate in mbar l/s:

$$\Phi\,[\mathrm{mbar}\cdot\mathrm{l/s}] = \frac{\Delta p}{\Delta t}\cdot V_{PAV} \tag{5.3}$$

where Δp is the pressure increase due to the permeation in the considered time Δt and V_{PAV} is the volume of the PAV vessel. From the permeation rate, the permeated flux is derived by:

$$\Phi\,[\mathrm{mol/s}] = \frac{\Phi\,[\mathrm{mbar}\cdot\mathrm{l/s}]}{10\cdot R\cdot T_{av}} \tag{5.4}$$

where T_{av} is an average temperature in the PAV vessel. This temperature cannot be directly measured and it is estimated by averaging the temperature of the PAV vessel wall and the temperature of the niobium tubes, but this process introduces a certain uncertainty in the calculation. For this reason, the pressurization test is conceived mainly as a way of confirming the order of magnitude of the flux measured by the leak detector.

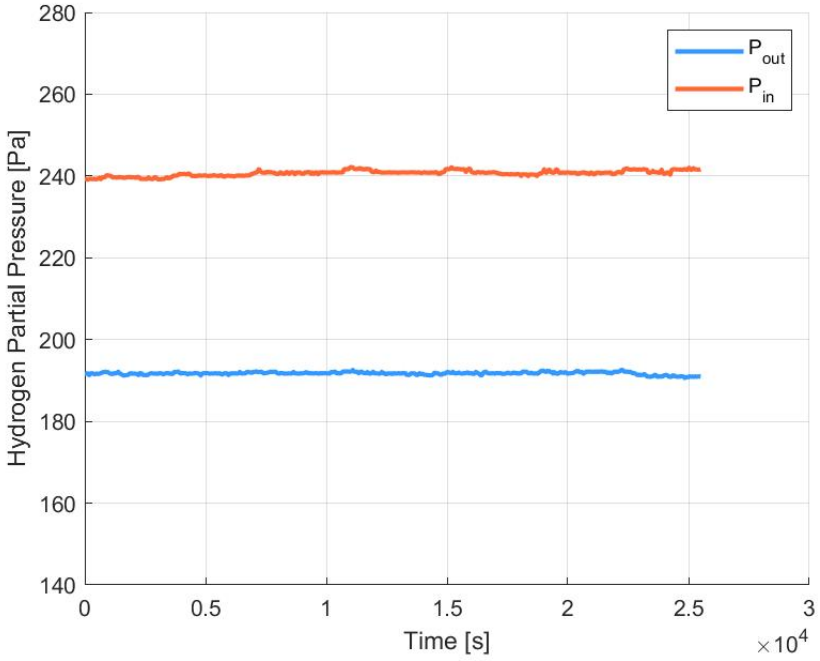

Figure 5.15. Example of partial pressure measured by the HPSs at the inlet and at the outlet of the PAV mock-up

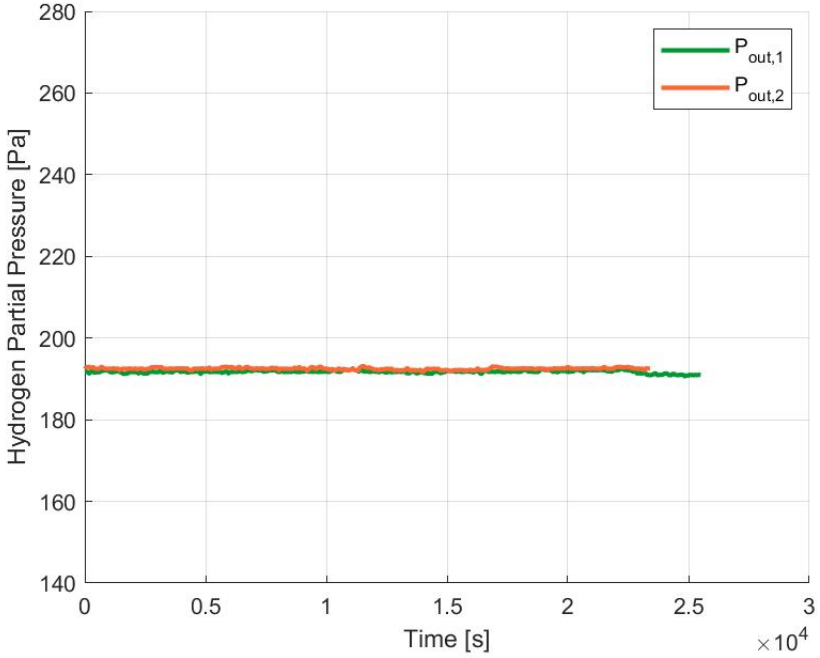

Figure 5.16. Example of partial pressure measured by the HPSs installed at the outlet of the PAV mock-up

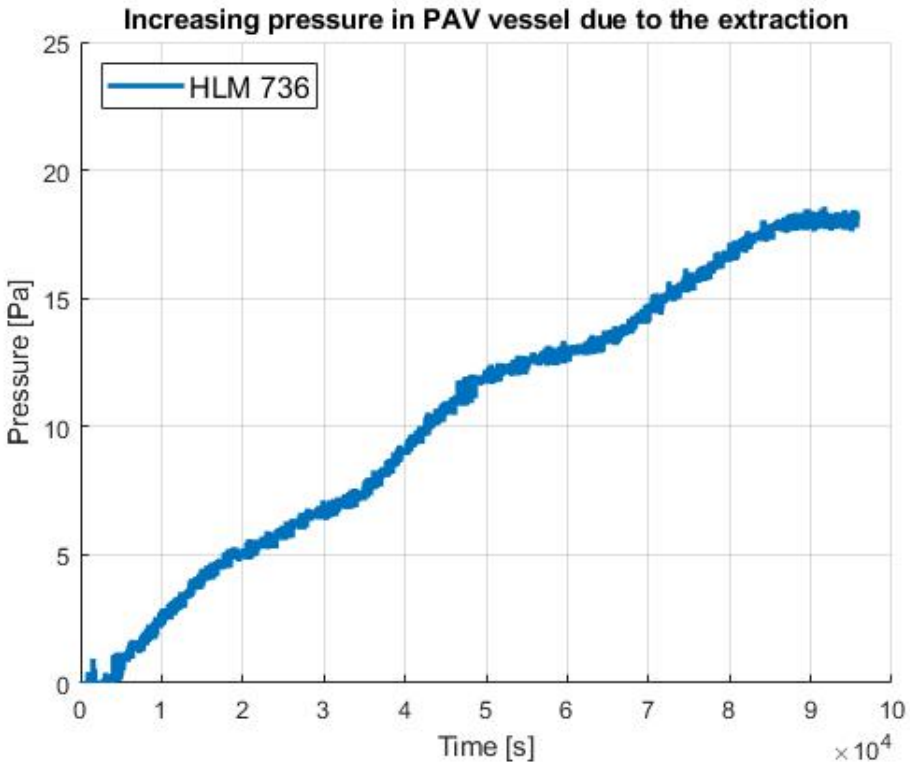

Figure 5.17. Example of pressure increase in the vacuum side of the PAV

5.4 Results of the experimental campaign

5.4.1 Summary of the results

The main results of the experimental campaign are summarized in Table 5.4 and in Table 5.5.

The first table shows the actual operative conditions of each experiment, which of course slightly differ from the ideal parameters listed in the test matrix. These data are complemented by the estimated measurement uncertainty 9.2, which is essential for the reliability of the experimental data and for the possibility to use them in discussions or even to validate numerical models.

The first table also includes the extraction efficiency for all the tests, even though this parameter is not considered the best one to compare tests at different operative conditions, as discussed in Section 5.4.2.

Moreover, the table shows the hydrogen partial pressure at the outlet of the PAV mock-up. A partial pressure difference across the PAV mock-up exists in every measurement, demonstrating that the extraction is occurring, and remains almost constant within each test, demonstrating the repeatability of the measurements. The extraction efficiencies for all the measurements are shown in Figure 5.18 together with their experimental error bars.

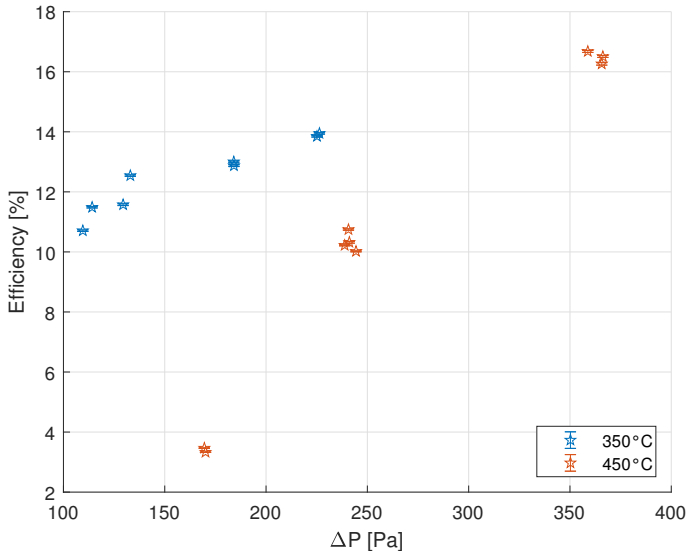

Figure 5.18. Extraction efficiencies as a function of the partial pressure difference between the LiPb entering the PAV and the vacuum side.

The most important parameter to characterize the performances of the PAV mock-up is the permeated flux, which is also the most relevant parameter for the design of the PAV system for the WCLL TER, as it can be used to estimate the size of a component able to extract the amount of tritium that has to be routed to the fuel cycle.

The parameters related to the amount of hydrogen that was permeating through the niobium walls during the tests are shown in the second table. The first column of data contains the measurements of the leak detector in mbar l/s, which were then

converted into mol/s by dividing the values by $10 \cdot R \cdot T_{LD}$, where R is the gas constant in J/(mol K), 10 comes from the conversions of mbar to Pa and liter to m^3 and T_{LD} is the temperature in the chamber of the leak detector in K.

Finally, the last column shows an estimation of the hydrogen permeated flux performed by closing the gate valve that connects the PAV chamber to the leak detector and measuring the pressure increase in the PAV chamber. Knowing the PAV volume and estimating the average temperature in the chamber, it is possible to calculate the corresponding flux.

Unfortunately, the estimation of the average temperature is not easy and, therefore, the flux calculated in this way can only be used as a confirmation of the order of magnitude, instead than an additional measurement (and this is reflected by the large uncertainties associated to these values). Nonetheless, the pressurization tests served as a qualitative confirmation that the leak detector is reliable in this kind of experiments.

The permeated fluxes were also divided by the area of the niobium tubes (about 0.42 m^2) to obtain an average flux per unit area. The values are shown in Table 5.6. Also these numbers are useful inputs for designing the tritium extraction unit of the WCLL TER.

The hydrogen fluxes in mol/s are reported in Figure 5.19 for the 7 tests.

The fluxes at 450 °C are approximately one order of magnitude higher than those at 350 °C and these results are coherent with the theory. The correlations for niobium diffusivity available in literature are quite scattered and have opposite trends with temperature (cf. for instance [19]). Nevertheless, the transport phenomena in LiPb and the surface processes have been shown to have a bigger importance in the overall transport with respect to diffusion by preliminary simulations that were performed at Politecnico di Torino using the PAV geometry and boundary conditions coming from experiments.

Moreover, the order of magnitude of the fluxes was confirmed by performing the so-called pressurization tests, as shown in Figure 5.20 for the tests at 450 °C and in Figure 5.21 for the tests at 350 °C. The pressurization tests were performed once per test, with the exception of test number 5, where the pressurization was performed for both measurements to confirm the repeatability of the pressurization test and increase the reliability of the measurement.

It can be noted that the four measurements of test number 2 show a slight decrease in performance with time. This can be motivated by the fact that the LiPb temperature decreased during the four measurements.

Finally, the measured permeation rates were compared with values obtained from modelling activities performed at Politecnico di Torino. As uncertainties exist on the tritium transport parameters for LiPb and niobium, these simulations were performed by using the highest and lowest values available in literature for the involved parameters. In this way, a maximum and a minimum value was obtained for the permeation rate of each test.

As shown in Table 5.7, the experimental permeation rates lie close to the minimum values obtained by the modelling activities. This can be explained by the fact that the niobium tubes of the PAV mock-up did not undergo any particular treatment and an oxide layer likely formed on their external side [80]. Indeed, this is coherent with the adoption of a correlation for oxidized surfaces for the niobium recombination

Table 5.4. Actual testing conditions and results of the PAV mock-up experimental campaign (with experimental error).p_{in} and p_{out} are the hydrogen partial pressures at the inlet and at the outlet of the PAV mock-up, T is the LiPb temperature measured by an immersed PT100 before its entrance in the PAV, $LiPb\ \dot{m}$ is the LiPb mass flow rate measured by the thermal mass flow meter.

Test	Measure	p_{in} [Pa]	p_{out} [Pa]	T [°C]	LiPb $\dot{m}$ [kg/s]	Efficiency [%]
1	1	170 ± 0.52	158 ± 0.58	453 ± 2.56	1.19 ± 0.10	3.46 ± 0.01
	2	170 ± 0.39	159 ± 0.52	458 ± 2.24	1.19 ± 0.10	3.33 ± 0.01
2	1	241 ± 0.83	192 ± 0.51	458 ± 2.26	1.19 ± 0.10	10.74 ± 0.03
	2	239 ± 0.60	192 ± 0.46	443 ± 2.21	1.19 ± 0.10	10.22 ± 0.03
	3	241 ± 0.82	194 ± 0.90	444 ± 2.25	1.18 ± 0.10	10.32 ± 0.04
	4	244 ± 0.53	198 ± 0.48	446 ± 2.21	1.18 ± 0.10	10.02 ± 0.02
3	1	359 ± 0.86	249 ± 0.79	446 ± 2.22	1.20 ± 0.10	16.68 ± 0.05
	2	366 ± 1.33	256 ± 0.92	445 ± 2.22	1.20 ± 0.10	16.26 ± 0.06
	3	366 ± 0.90	255 ± 0.74	446 ± 2.21	1.20 ± 0.10	16.51 ± 0.04
4	1	114 ± 0.33	89 ± 0.23	354 ± 1.84	1.28 ± 0.10	11.49 ± 0.03
	2	110 ± 0.33	87 ± 0.22	353 ± 1.82	1.28 ± 0.10	10.71 ± 0.03
5	1	129 ± 0.40	101 ± 0.41	353 ± 1.84	1.22 ± 0.10	11.57 ± 0.04
	2	133 ± 0.38	102 ± 0.41	352 ± 1.83	1.22 ± 0.10	12.54 ± 0.03
6	1	184 ± 0.47	139 ± 0.50	353 ± 1.86	1.22 ± 0.10	13.00 ± 0.04
	2	184 ± 0.49	140 ± 0.50	353 ± 1.85	1.22 ± 0.10	12.87 ± 0.04
7	1	226 ± 0.48	168 ± 0.45	353 ± 1.84	1.22 ± 0.10	13.95 ± 0.03
	2	225 ± 0.47	167 ± 0.45	353 ± 1.87	1.22 ± 0.10	13.85 ± 0.03

coefficient in the modelling activities ([81]).

5.4.2 On the relationship between the efficiency and the permeated flux

The efficiency has usually been considered as the main result of a campaign devoted to characterize a tritium extraction technology (e.g. [15]) but it is strictly related to the geometry of the system, so it is difficult to use it to compare different technologies.

Moreover, the efficiency is also linked with the operative temperature and with the permeated flux via a relationship which is described in this section.

First, it is necessary to recall the definition of efficiency:

$$\eta = 1 - \frac{C_{out}}{C_{in}} * 100 = \frac{\sqrt{p_{in}} - \sqrt{p_{out}}}{\sqrt{p_{in}}} * 100 \tag{5.5}$$

where C_{in} and C_{out} are the concentrations at the inlet and at the outlet of the system. Likewise, the permeated flux can be written by performing a mass balance across the system (cf. Figure 5.22):

$$\Phi = k_s \cdot (\sqrt{p_{in}} - \sqrt{p_{out}}) \cdot \frac{\dot{m}}{\rho} \tag{5.6}$$

where k_s is the Sieverts' constant, $\dot{m}$ is the LiPb mass flow rate and ρ is the LiPb density. It is possible to combine these two equations, obtaining a relationship between the flux and the efficiency:

Table 5.5. Measured permeation rate and hydrogen permeated flux calculated from the data of the leak detector and measured by pressurization test (with experimental error)

Test	Measure	Permeation rate [mbar · l/s]	Permeated flux [mol/s]	Flux press. [mol/s]
1	1	$1.10 \cdot 10^{-3} \pm 5.71 \cdot 10^{-5}$	$4.58 \cdot 10^{-8} \pm 2.75 \cdot 10^{-9}$	$4.42 \cdot 10^{-8} \pm 1.59 \cdot 10^{-8}$
	2	$1.20 \cdot 10^{-3} \pm 5.25 \cdot 10^{-5}$	$4.67 \cdot 10^{-8} \pm 2.58 \cdot 10^{-9}$	
2	1	$1.28 \cdot 10^{-3} \pm 6.30 \cdot 10^{-5}$	$3.00 \cdot 10^{-8} \pm 1.67 \cdot 10^{-9}$	$3.31 \cdot 10^{-8} \pm 1.18 \cdot 10^{-8}$
	2	$1.12 \cdot 10^{-3} \pm 4.18 \cdot 10^{-5}$	$2.56 \cdot 10^{-8} \pm 1.18 \cdot 10^{-9}$	
	3	$6.17 \cdot 10^{-4} \pm 8.79 \cdot 10^{-5}$	$1.73 \cdot 10^{-8} \pm 1.51 \cdot 10^{-9}$	
	4	$4.81 \cdot 10^{-4} \pm 2.19 \cdot 10^{-5}$	$1.15 \cdot 10^{-8} \pm 5.90 \cdot 10^{-10}$	
3	1	$1.41 \cdot 10^{-3} \pm 9.93 \cdot 10^{-6}$	$3.08 \cdot 10^{-8} \pm 6.84 \cdot 10^{-10}$	$6.93 \cdot 10^{-8} \pm 2.47 \cdot 10^{-8}$
	2	$1.71 \cdot 10^{-3} \pm 6.77 \cdot 10^{-5}$	$3.75 \cdot 10^{-8} \pm 1.88 \cdot 10^{-9}$	
	3	$1.80 \cdot 10^{-3} \pm 1.10 \cdot 10^{-4}$	$3.95 \cdot 10^{-8} \pm 2.80 \cdot 10^{-9}$	
4	1	$1.41 \cdot 10^{-4} \pm 1.12 \cdot 10^{-5}$	$3.37 \cdot 10^{-9} \pm 3.00 \cdot 10^{-10}$	$5.02 \cdot 10^{-9} \pm 1.41 \cdot 10^{-9}$
	2	$1.25 \cdot 10^{-4} \pm 7.89 \cdot 10^{-7}$	$2.98 \cdot 10^{-9} \pm 6.49 \cdot 10^{-11}$	
5	1	$8.38 \cdot 10^{-5} \pm 1.75 \cdot 10^{-5}$	$2.00 \cdot 10^{-9} \pm 4.36 \cdot 10^{-10}$	$4.40 \cdot 10^{-9} \pm 1.23 \cdot 10^{-9}$
	2	$1.22 \cdot 10^{-4} \pm 3.36 \cdot 10^{-6}$	$2.90 \cdot 10^{-9} \pm 1.13 \cdot 10^{-10}$	$6.97 \cdot 10^{-9} \pm 1.96 \cdot 10^{-9}$
6	1	$1.47 \cdot 10^{-4} \pm 6.28 \cdot 10^{-6}$	$3.00 \cdot 10^{-9} \pm 1.80 \cdot 10^{-10}$	$4.51 \cdot 10^{-9} \pm 1.27 \cdot 10^{-9}$
	2	$1.47 \cdot 10^{-4} \pm 1.16 \cdot 10^{-5}$	$2.90 \cdot 10^{-9} \pm 3.03 \cdot 10^{-10}$	
7	1	$1.24 \cdot 10^{-4} \pm 4.60 \cdot 10^{-6}$	$2.96 \cdot 10^{-9} \pm 1.41 \cdot 10^{-10}$	$7.61 \cdot 10^{-9} \pm 2.14 \cdot 10^{-9}$
	2	$1.11 \cdot 10^{-4} \pm 3.95 \cdot 10^{-7}$	$2.64 \cdot 10^{-9} \pm 5.47 \cdot 10^{-11}$	

$$\Phi(T) = \frac{k_s(T) \cdot \sqrt{p_{in}} \cdot \eta(T) \cdot \dot{m}}{100 \cdot \rho(T)} \tag{5.7}$$

This equation highlights that there are a total of four parameters that are expected to change with temperature: the efficiency η and the flux Φ, of course, but also LiPb density and Sieverts' constant. This means that the trend of the efficiency with temperature is not easily anticipated by looking at the flux alone.

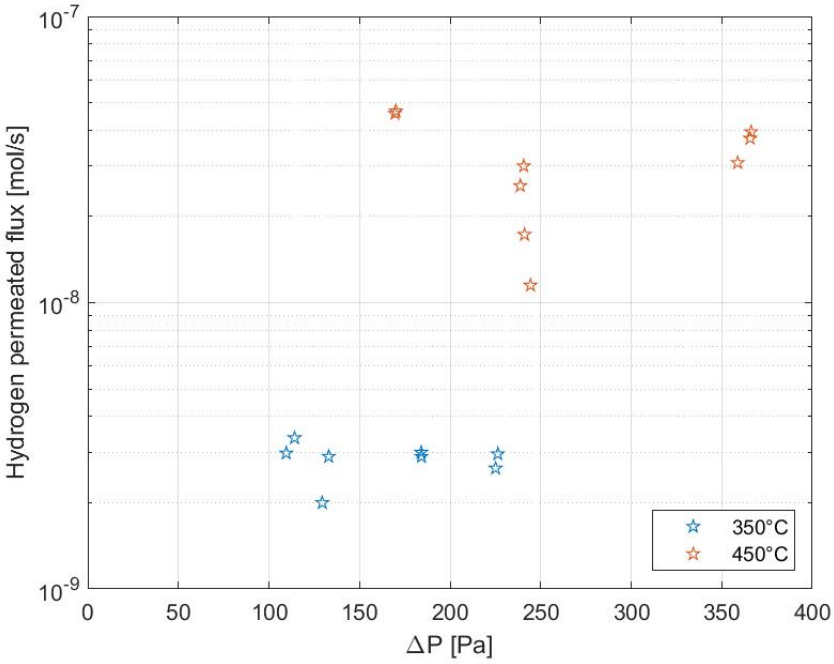

Figure 5.19. Hydrogen permeated flux as a function of the partial pressure difference between the LiPb entering the PAV and the vacuum side. Red stars indicate the fluxes at 450 °C, blue ones those at 350 °C.

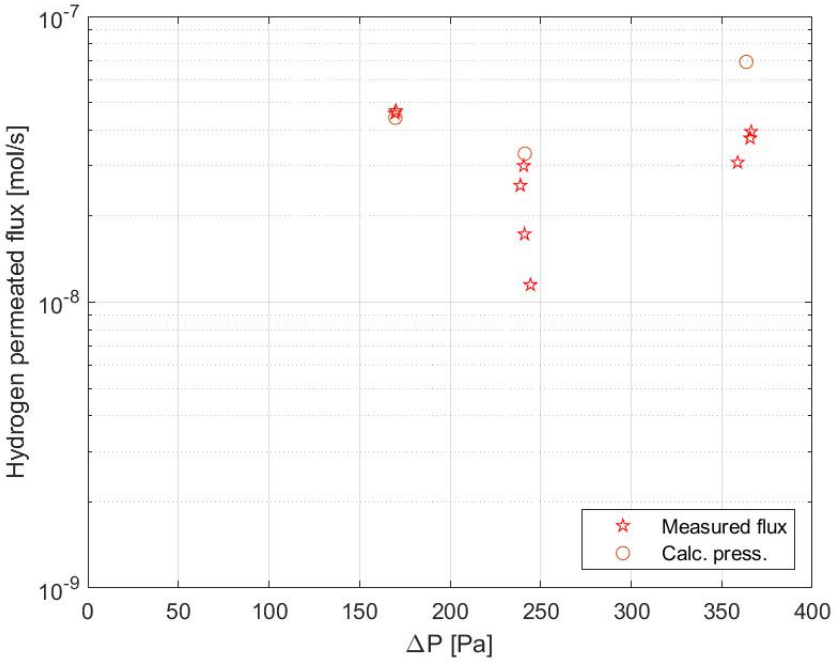

Figure 5.20. Hydrogen permeated fluxes for the tests at 450 °C (stars) compared with the fluxes calculated from the data of the pressurization tests (circles)

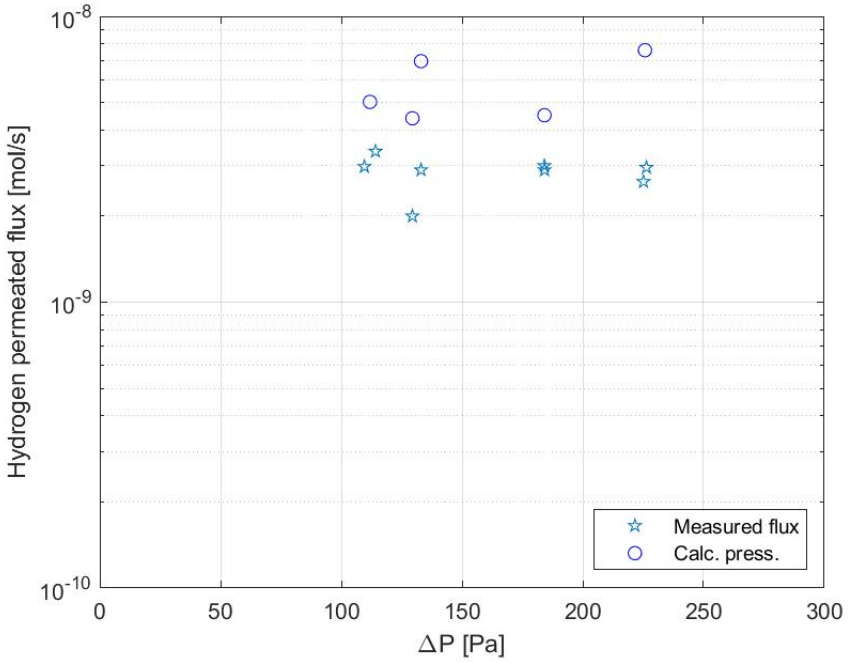

Figure 5.21. Hydrogen permeated fluxes for the tests at 350 °C (stars) compared with the fluxes calculated from the data of the pressurization tests (circles)

Table 5.6. Hydrogen permeated flux per unit area (with experimental error)

Test	Measure	Flux per unit area $\left[\mathbf{mol}/(\mathbf{s}\cdot\mathbf{m^2})\right]$
1	1	$1.08 \cdot 10^{-7} \pm 6.47 \cdot 10^{-9}$
	2	$1.10 \cdot 10^{-7} \pm 6.07 \cdot 10^{-9}$
2	1	$7.06 \cdot 10^{-8} \pm 3.93 \cdot 10^{-9}$
	2	$6.03 \cdot 10^{-8} \pm 2.77 \cdot 10^{-9}$
	3	$4.08 \cdot 10^{-8} \pm 3.55 \cdot 10^{-9}$
	4	$2.70 \cdot 10^{-8} \pm 1.39 \cdot 10^{-9}$
3	1	$7.26 \cdot 10^{-8} \pm 1.61 \cdot 10^{-9}$
	2	$8.82 \cdot 10^{-8} \pm 4.42 \cdot 10^{-9}$
	3	$9.30 \cdot 10^{-8} \pm 6.58 \cdot 10^{-9}$
4	1	$7.92 \cdot 10^{-9} \pm 7.05 \cdot 10^{-10}$
	2	$7.01 \cdot 10^{-9} \pm 1.53 \cdot 10^{-10}$
5	1	$4.70 \cdot 10^{-9} \pm 1.03 \cdot 10^{-9}$
	2	$6.83 \cdot 10^{-9} \pm 2.66 \cdot 10^{-10}$
6	1	$7.06 \cdot 10^{-9} \pm 4.24 \cdot 10^{-10}$
	2	$6.82 \cdot 10^{-9} \pm 7.14 \cdot 10^{-10}$
7	1	$6.97 \cdot 10^{-9} \pm 3.32 \cdot 10^{-11}$
	2	$6.22 \cdot 10^{-9} \pm 1.29 \cdot 10^{-10}$

Table 5.7. Comparison of measured permeation rates with the minimum and maximum values obtained from modelling

Test	Measure	Exp. permeation rate [mbar · l/s]	Min. permeation rate from model [mbar · l/s]	Max. permeation rate from model [mbar · l/s]
1	1 2	$1.10 \cdot 10^{-3}$ $1.20 \cdot 10^{-3}$	$8.82 \cdot 10^{-4}$	$1.19 \cdot 10^{0}$
2	1 2 3 4	$1.28 \cdot 10^{-3}$ $1.12 \cdot 10^{-3}$ $6.17 \cdot 10^{-4}$ $4.81 \cdot 10^{-4}$	$1.10 \cdot 10^{-3}$	$1.42 \cdot 10^{0}$
3	1 2 3	$1.41 \cdot 10^{-3}$ $1.71 \cdot 10^{-3}$ $1.80 \cdot 10^{-3}$	$1.30 \cdot 10^{-3}$	$1.75 \cdot 10^{0}$
4	1 2	$1.41 \cdot 10^{-4}$ $1.25 \cdot 10^{-4}$	$8.13 \cdot 10^{-5}$	$5.64 \cdot 10^{-1}$
5	1 2	$8.38 \cdot 10^{-5}$ $1.22 \cdot 10^{-4}$	$8.45 \cdot 10^{-5}$	$5.82 \cdot 10^{-1}$
6	1 2	$1.47 \cdot 10^{-4}$ $1.47 \cdot 10^{-4}$	$1.01 \cdot 10^{-4}$	$6.92 \cdot 10^{-1}$
7	1 2	$1.24 \cdot 10^{-4}$ $1.11 \cdot 10^{-4}$	$1.12 \cdot 10^{-4}$	$7.66 \cdot 10^{-1}$

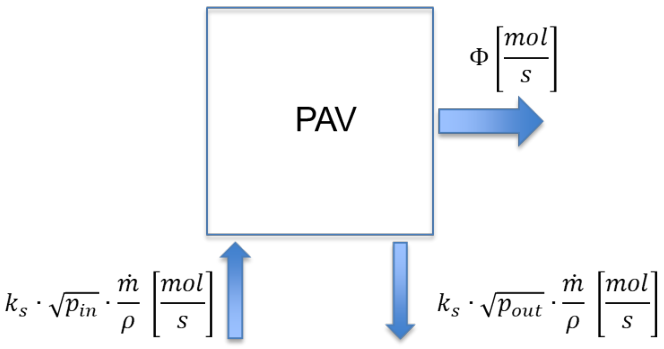

Figure 5.22. Skect of the mass balance across the PAV mock-up.

5.5 Main outcomes of the activities on the Permeator Against Vacuum

This section summarizes the main achievements of the activities on the PAV mock-up. When this thesis started, a conceptual design of a PAV mock-up had already been done by the group of Prof. Bonifetto at Politecnico di Torino and it was engineered during the first part of the work. Afterwards, the techniques to manufacture the joint between F22 plate and the Nb tubes of the mock-up were selected together with experts from RINA CSM. In the meanwhile, a selection of the most suitable instruments and pieces of equipment was performed, in parallel with a refurbishment of TRIEX-II facility to host the PAV mock-up. The manufacturing of the first PAV mock-up for LiPb to ever be completed, and its successful commissioning, constitutes an important milestone towards the development of the WCLL TER, as the possibility to manufacture a PAV was questioned at the end of the Framework Program 8 ([82]).

After the installation of PAV-ONE in TRIEX-II, a first experimental campaign was carried out with the aim of characterizing the mock-up performances at different temperatures and hydrogen partial pressures. The experimental campaign demonstrated that the manufacturing techniques can withstand the harsh conditions of a LiPb flow, but, most importantly, also that the PAV technology can be used to extract hydrogen isotopes from a stream of LiPb. The tests highlighted that the higher the temperature the higher the permeated flux, with approximately one order of magnitude between the tests at 350 °C (in the order of 10^{-9} mol/s) and those at 450 °C (in the order of 10^{-8} mol/s). These results are also confirmed by the pressurization tests, which indicate similar orders of magnitude for the permeated flux, and by the signals of the Hydrogen Permeation Sensors, which show a partial pressure drop across the mock-up that is repeatable within each test and that increases with the inlet partial pressure.

Chapter 6

Gas-Liquid Contactor

One of the activities carried out during the PhD was an experimental campaign on the Gas-Liquid Contactor in TRIEX-II facility, performed in 2021. This chapter describes the tests performed and the relults obtained. Surprisingly, the calculated efficiency was found to be extremely low (about 6% in 32h) and this motivated a post-mortem analysis of the GLC with an endoscopy. It was discovered that the GLC packings were gravely corroted by the LiPb flow. Therefore, the component was disassembled and a SEM analysis was performed on the pakings.

6.1 GLC description

One of the two TRIEX-II mock-ups is the Gas-Liquid Contactor. GLC is a well-known industrial technology [83] and has already been used in experimental qualifications with LiPb [41][15], even if in these cases the H_2 mass balance could not be verified. In this technology, a gas and a liquid are brought into contact, allowing a diffusion exchange between them. GLC are typically classified depending on the interface surface that mediates the contact between the two fluids. The GLC of TRIEX-II is characterized as a packed column type [71]. Packed columns are vertical columns filled with a packing which breaks the liquid flow and provides a large interfacial area between the liquid and the gas phases.

In the packed column, the extraction of the hydrogen isotopes from LiPb is mediated by the use of a stripping gas (helium). The gas injection system is positioned at the bottom of the tank to achieve a complete dispersion of gas bubbles inside the tank containing the LiPb, counter-current with the liquid metal. The continuously injected gas in the tank leaves from the top with appropriate flow control so as to adjust the pressure inside the tank and consequently the level of the LiPb. The packed column can also be lengthened or shortened in order to collect an opportune data set for modelling, varying both the LiPb mass flow rate and the volumetric flow rate of the purge gas. As far as packings are concerned, two main groups can be individuated: the random packing and the structured packing [83]. Structured packing was chosen because of:

- maximisation of the specific surface area, which increases the gas-liquid contact area;

- uniformly spreading of the surface area, augmenting the gas-liquid contact;
- maximisation of the void space per unit volume of the column, which minimises the resistance to gas up-flow;
- minimisation of the friction, realised with an open shape in order to give good aerodynamic characteristics;
- minimisation of the costs, which rise with the weight per unit volume of the packing.

The GLC column of TRIEX-II is made of 2-1/4 Cr-1 Mo steel and is operated with a stripping gas of helium or helium plus hydrogen. Sulzer MellapakPlus 452Y structured packing, manufactured in AISI 316, was chosen to be firstly qualified in TRIEX-II in order to minimise the risk of hold-up due to the high value of surface tension of the LiPb, as suggested by the manufacturer. The main design parameters are reported in Table 6.1.

Table 6.1. Design parameters of the GLC mock-up equipped with MellapakPlus 452Y in TRIEX-II

Parameter	Value	Units
Design pressure	10	barg
Design temperature	530	°C
Max. operative temperature	500	°C
Void fraction	98	%
Surface-to-volume ratio	350	$m^2\ m^{-3}$
Design temperature	530	°C
Gas stripping flow rate range S300	50-450	Nl h^{-1}
LiPb mass flow range in S300	0.2-4.5	kg s^{-1}
Column internal diameter	154.1	mm
Total height	2.5	m
Structured packing height	852	mm
Void fraction packing	95	%

When the GLC mock-up was designed, a preliminary estimation of AISI316 packing corrosion was made on the basis of [84]. The analysis performed in [43] pointed out a 50% weight reduction in about 5 years of continous operation. However, the experience described in this chapter showed that the aggressive LiPb environment combined with the necessity to clean the GLC component during maintenance (with a solution of water, acetic acid and hydrogen peroxide) could significantly shorten the lifetime of packings due to corrosion, compared with the ones reported in the literature for stainless steels in LiPb.

In the extractor of TRIEX-II , the LiPb enters the upper part and it is uniformly distributed on the filling material by means of a dedicated diffuser. Due to the low solubility of hydrogen isotopes in LiPb and to its concentration gradient at the LiPb/gas interface, a mass transport occurs with the passage of hydrogen isotopes from the LiPb to the gas phase. The higher the LiPb/gas interface, the greater

the total flow of extracted hydrogen isotopes. The extraction process of hydrogen isotopes from the LiPb is also determined by the thickness of the LiPb film on the surface of the metal sheet that composes the packing of the column. The lower the LiPb film height, the lower the time required by hydrogen isotopes to diffuse from the LiPb to the LiPb/carrying gas interface.

The gas injection and extraction lines are normally kept at room temperature, but they are equipped with heating cables and thermal insulation. In this way, they can be heated in case of a LiPb ingress in the lines to prevent solidification and obstruction. Then, once the loop is completely drained, LiPb can be removed by increasing the gas pressure in the lines.

6.2 GLC Experimental campaign

During this experimental campaign, the hydrogen permeation sensors were in the first configuration, as explained in the Chapter 4. Their repeatability was tested and an example is shown in Figure 6.1. The sensor operating procedure, in equilibrium mode, is constituted by the following steps:

1. The vacuum is created inside the permeation sensor;

2. The permeation sensor is isolated by means of the pneumatic valve;

3. After about 24 h, the pressure, measured by means of the vacuum pressure transducer, becomes constant and this means that it reaches the equilibrium with the hydrogen concentration inside the LiPb.

The intrinsic leakage of each sensor, when present, is measured and removed from the measured value. HLM 735 sensor has been taken as a reference as it showed the most stable behavior and it had no leakages during the pre-tests and the experiments.

The test matrix of the experimental campaign is reported in Table 6.2 and the test procedure is described in the following:

1. Measurement of the initial hydrogen partial pressure (p_0) in LiPb by means of permeation sensor HLM 735.

2. The extraction phase begins by injecting a flow rate (G) of stripping gas in the extractor. The stripping gas flow rate is kept constant for 32 h. This time was selected to be long enough to ensure a complete stabilization of the signal of the permeation sensors and to measure a decrease in the hydrogen partial pressure which is significant with respect to the instrument sensitivity.

3. During the extraction the hydrogen partial pressure decreases and it is measured.

4. At the end of the extraction phase the hydrogen partial pressure in LiPb is measured by the permeation sensors (p_1).

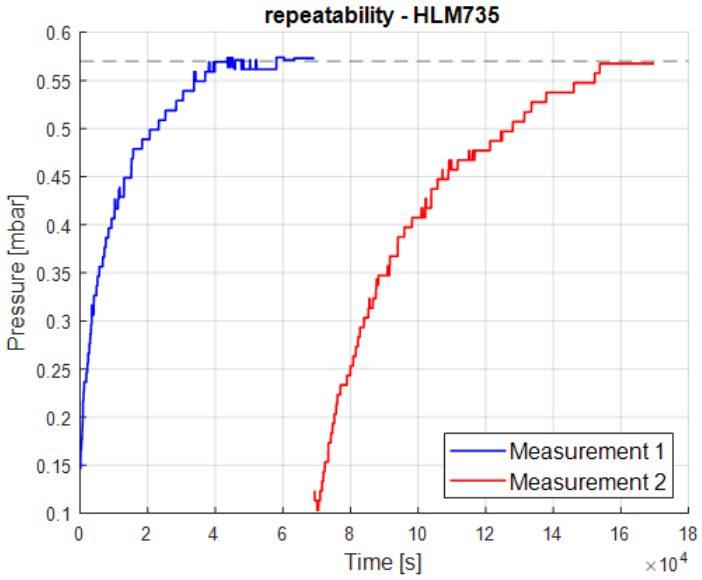

Figure 6.1. Repeatability of the hydrogen permeation sensor

5. The measurement is repeated by pumping vacuum in the sensors and waiting for them to stabilize at the hydrogen partial pressure. With this procedure, any spurious measurement is easily detected and that test can be discarded. The vacuum is pumped for a small period of time (10 min) so that the hydrogen partial pressure in LiPb is not further reduced by the sensors, as they extract hydrogen since they share the working principle with the Permeator Against Vacuum.

6. The efficiency averaged over the 32 h of extraction can be calculated as:

$$\eta = 1 - \frac{C_{out}}{C_{in}} * 100 = \frac{\sqrt{p_{in}} - \sqrt{p_{out}}}{\sqrt{p_{in}}} * 100 \tag{6.1}$$

The efficiency of a single passage in the extractor can be evaluated by dividing the average efficiency by the time required for the LiPb to make a complete loop. This time has been calculated and it is about 15.7 minutes. This estimation was performed by measuring the length of each pipe of TRIEX-II and, knowing the internal diameters, it was possible to compute the average LiPb velocity in it. For the saturator and the extractor, the average LiPb velocity was derived by the pressure drops measured with the differential pressure transducers. By summing all the contributions, it was possible to estimate the average time needed for an ideal LiPb particle to travel in the entire loop.

6.2.1 Data analysis

The actual testing conditions and the experimental results are reported in Table 6.3. In each test, the hydrogen partial pressure is measured twice. The first measurement

Table 6.2. Deuterium concentration in the samples after the background subtractions

Test number	LiPb mass flow rate	Stripping gas flow rate in Nl/h	L/G	T in °C	H partial p in Pa
1	0.9	100	3.5	450	103
2	0.9	100	3.5	450	94
3	0.9	100	3.5	450	84
4	0.9	100	3.5	450	72
5	0.6	100	2	450	58
6	0.6	100	2	450	46
7	0.9	50	7	450	45
8	0.9	200	2	450	45

is made while the extraction is on-going: the pressure measured by the sensor decreases due to the lower hydrogen partial pressure in the eutectic alloy with respect to inside the sensors. The second measurement is made when extraction is completed: vacuum is made in the sensors and then they are isolated again to reach the equilibrium. The value of hydrogen partial pressure considered in the efficiency calculations is the average of the signal after it has stabilized. An example of this procedure is shown in Figure 6.2.

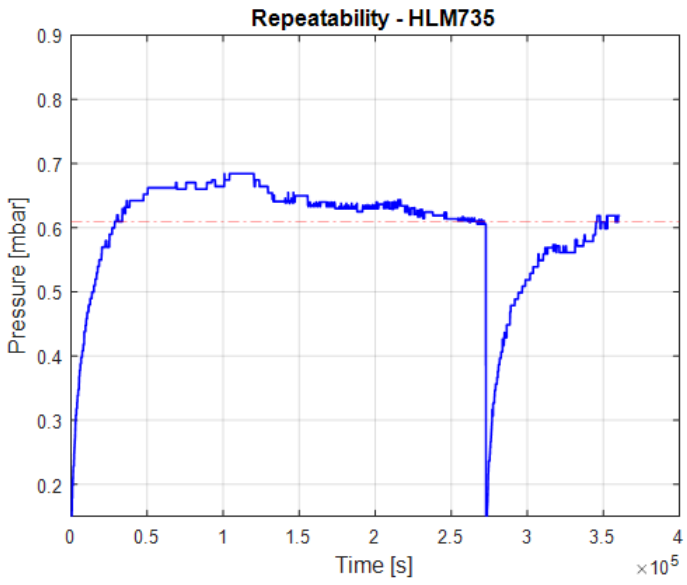

Figure 6.2. Example of the double measurement of hydrogen partial pressure

A leakage in the sensor HLM 734 was detected during the experimental campaign, therefore the sensor could not reach the equilibrium. However, since the leakage is constant, it was possible to find its contribution to the pressure trend by interpolating the experimental values in each measurement. Then, the real hydrogen partial pressure was calculated by subtracting the evaluated loss trend from the measured signal.

The following figures Figure 6.3-Figure 6.10 show the normalized sensor pressure trends before and after the extraction. The pressure trends are normalized with the

Table 6.3. Actual testing conditions and experimental results

Test number	H partial p in Pa	LiPb ṁ in kg/s	Stripping gas flow rate in Nl/h	L/G	η_{735} in 32 h	η_{734} in 32 h
1	103	0.91	98.9	3.4	4.43	4.33
2	94	0.9	99	3.4	5.3	5.05
3	84	0.88	99.3	3.3	6.57	8.91
4	72	0.83	99.2	3.1	10.2	5.84
5	58	0.61	98.9	2.3	6.3	5.14
6	46	0.66	99.1	2.5	1.07	8.03
7	45	0.95	48.9	7.2	0	0
8	45	0.92	204.2	1.7	1.65	0

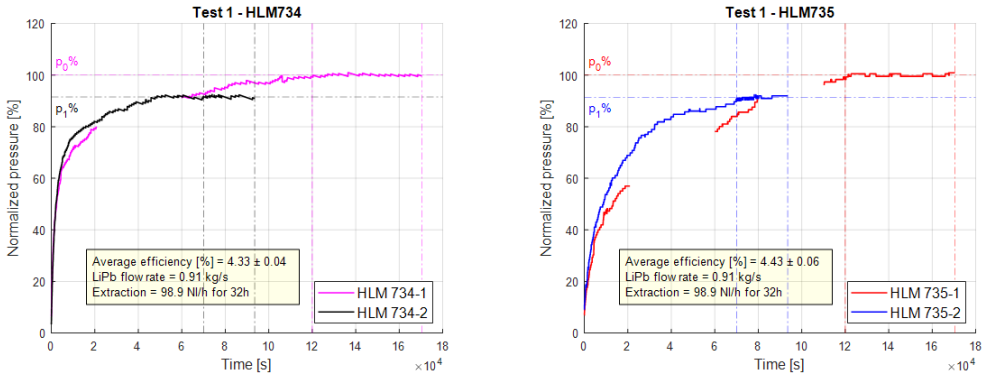

(a) **(b)**

Figure 6.3. Normalized hydrogen partial pressure in test 1

average equilibrium value of the measurement before the extraction. The trend is considered stable between the vertical dotted lines shown in the plots. The pressure measurement before the extraction (whose equilibrium value is labelled $p_0\%$) is reported in the plots in red, for the sensor HLM 735, and in magenta, for the HLM 734. The measurement after the extraction (whose equilibrium value is labelled $p_1\%$) is in blue and in black, respectively. In some tests, there were interruptions of acquisition while the sensors were reaching the equilibrium. However, these interruptions did not influence the tests, as the equilibrium values are clearly identifiable.

It can be noted that the calculated efficiency is about 6% in 32 h in the first five tests, when the hydrogen partial pressure was higher than 60 Pa. A drop in efficiency is evident when the hydrogen partial pressure reaches values below 60 Pa.

Table 6.4 shows the data for each instrument involved in the test. Accuracy and temperature effect of the pressure transducers and the amplification and offset error of the control unit were considered to calculate the error in the efficiency. The propagation of the error from the primary quantities (the hydrogen partial pressure) to the derived quantities (the efficiency) was calculated by means of the method of sequential perturbations, proposed by [85]. In each plot of the experimental results the total error of the efficiency is reported. The total error on the efficiency is reported in Table 6.5. The final results are reported in Table 6.6 together with the

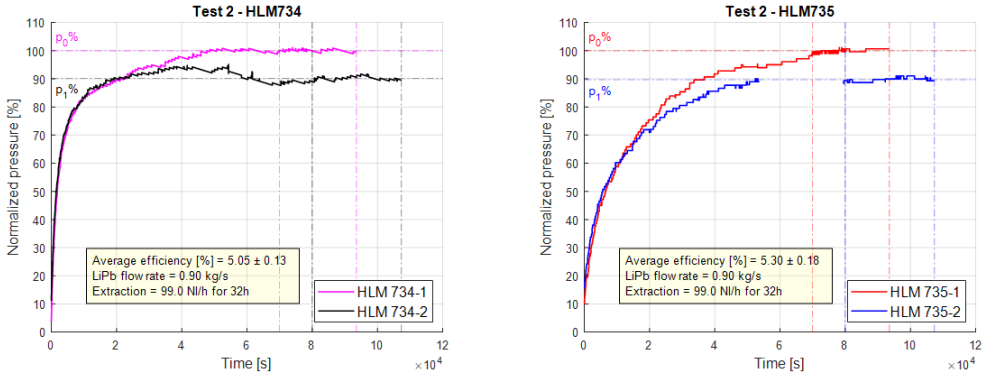

(a) **(b)**

Figure 6.4. Normalized hydrogen partial pressure in test 2

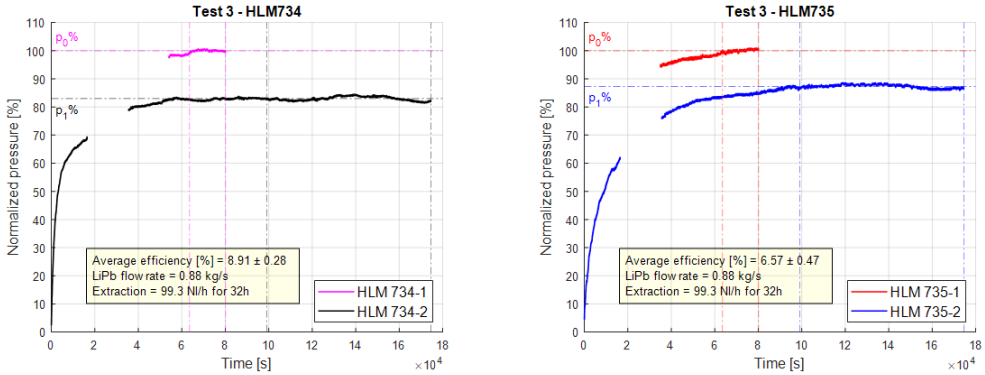

(a) **(b)**

Figure 6.5. Normalized hydrogen partial pressure in test 3

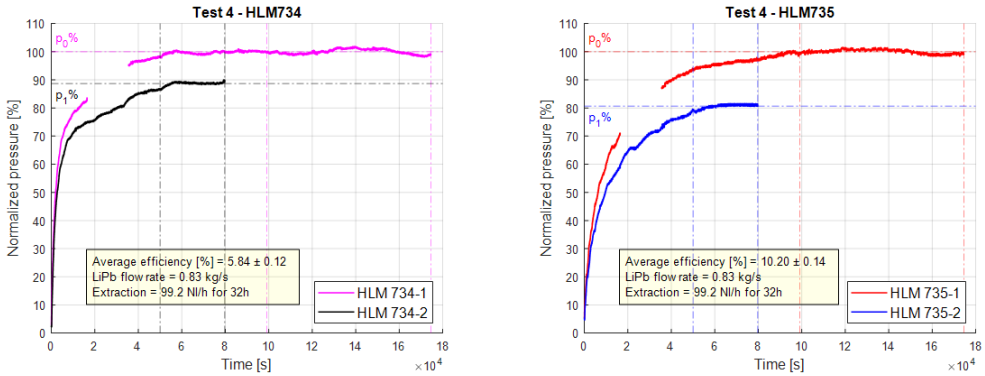

(a) **(b)**

Figure 6.6. Normalized hydrogen partial pressure in test 4

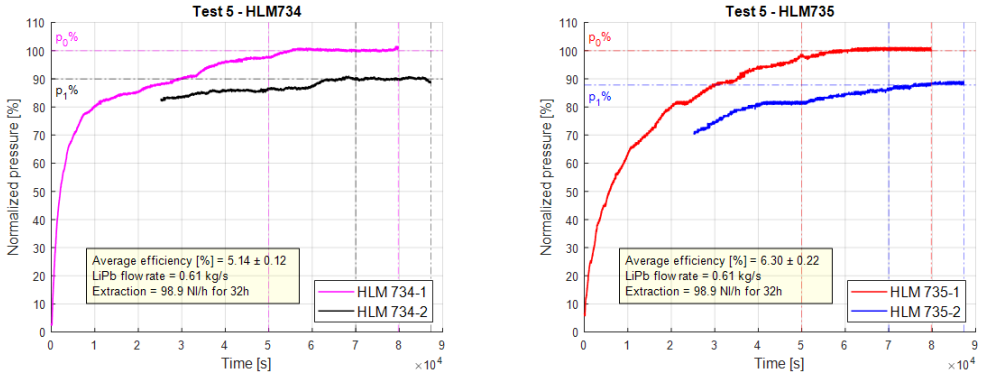

(a) (b)

Figure 6.7. Normalized hydrogen partial pressure in test 5

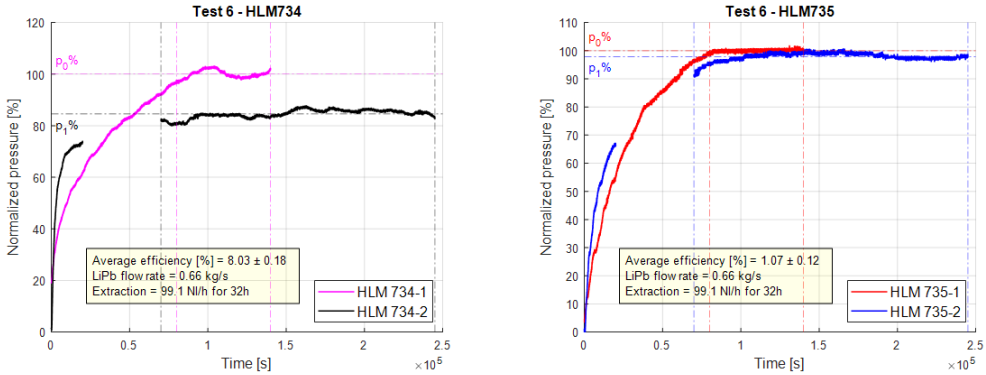

(a) (b)

Figure 6.8. Normalized hydrogen partial pressure in test 6

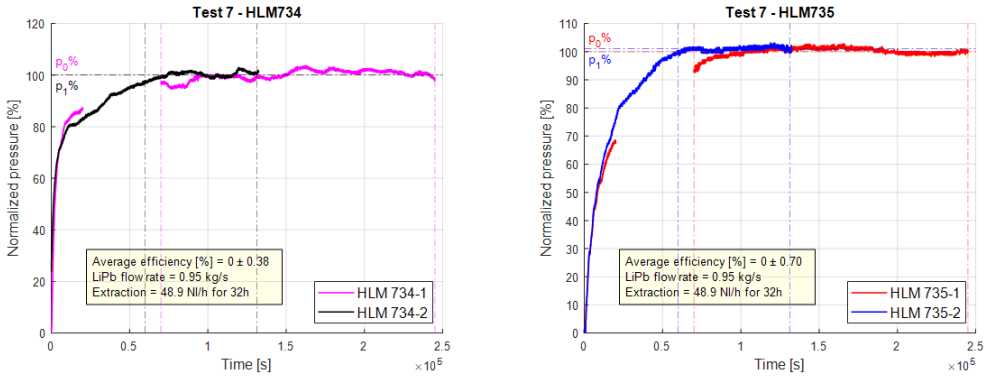

(a) (b)

Figure 6.9. Normalized hydrogen partial pressure in test 7

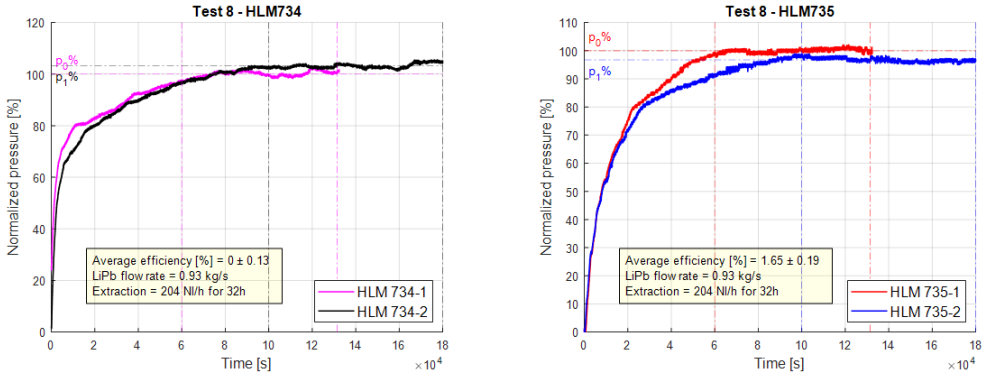

(a) **(b)**

Figure 6.10. Normalized hydrogen partial pressure in test 8

Table 6.4

Instrument	Accuracy	FSO	T effect
HLM 733	0.15% of reading	100 hPa	0.01% of reading
HLM 734	0.15% of reading	100 hPa	0.01% of reading
HLM 735	0.15% of reading	100 hPa	0.01% of reading
Control unit	0.01% FSO (amplification+offset error)	100 hPa	/
TFM	0.1 kg/s	5 kg/s	/
Thermocouple	$\pm 1.5°C$ from $-40°C$ to $+375°C$ $\pm 0.004 \cdot T[°C]$ above $+375°C$	$1260°C$	/ /
Helium mass flow meter	0.5% of reading +0.1% FSO	250 Nl/h	/

evaluated experimental errors.

Following the low efficiencies with respect to the past experiments [41][15] and to the theoretical ones, the GLC column was disassembled to check for possible issues. An endoscopy was performed finding that the packing at the top among the five piled in the GLC mock-up was collapsed. For this reason, the packings were extracted from the mock-up and analysed with the SEM and XRD. The packing appearance after the campaign is shown in Figure 6.11. It can be noted that the lowest packings were less affected by the corrosive attack with respect to the ones on top.

6.2.2 Chemical analysis of the corroded packings

This section reports about the microstructural characterization of the AISI 316 materials of the packed column of the GLC, performed in the materials characterization laboratory of ENEA Brasimone R.C. The component worked for about 4000-6000 h at 400-450 °C. The investigation was carried out by Scanning Electron Microscopy (SEM) and X-Ray Diffraction (XRD).

The samples of Mellapak foil and net observed both to the naked eye and under SEM analysis, revealed the presence of an encrustation/deposit on the original AISI 316 steel (Figure 6.13, Figure 6.14).

The EDX (Energy Dispersive X-ray) investigations on the Mellapak laminas

Table 6.5. Total errors in the measurements of HLM 734 and HLM 735

Test number	**Total error on the efficiency in % (734)**	**Total error on the efficiency in % (735)**
1	0.06	0.04
2	0.18	0.13
3	0.47	0.28
4	0.14	0.12
5	0.22	0.12
6	0.12	0.18
7	0.7	0.38
8	0.19	0.13

Table 6.6. Results with experimental error

Test number	**H partial p in Pa**	**LiPb $\dot{m}$inkg/s in kg/s**	**Stripping gas flow rate in Nl/h**	L/G	η_{735} **in 32 h**	η_{734} **in 32 h**
1	103	0.91	98.9	3.4	4.43 ± 0.06	4.33 ± 0.04
2	94	0.9	99	3.4	5.3 ± 0.18	5.05 ± 0.13
3	84	0.88	99.3	3.3	6.57 ± 0.47	8.91 ± 0.28
4	72	0.83	99.2	3.1	10.2 ± 0.14	5.84 ± 0.12
5	58	0.61	98.9	2.3	6.3 ± 0.22	5.14 ± 0.12
6	46	0.66	99.1	2.5	1.07 ± 0.12	8.03 ± 0.18
7	45	0.95	48.9	7.2	0 ± 0.70	0 ± 0.38
8	45	0.92	204.2	1.7	1.65 ± 0.19	0 ± 0.13

Figure 6.11. Packings appearance after the experimental campaign: the packings are numbered from 1 to 5 starting from the bottom of the column

evidences a severe dissolution attack by the molten metal to the 316L steel with depletion of nickel and chromium, behavior already observed in this kind of steels exposed to liquid lead alloys [86]. The depletion of alloying constituents produces in the Mellapak foils a porous microstructure and a reduction of the thickness from the 89 microns measured on the virgin material to about 40 microns.

Where the original alloy was accessible, the morphology of the foil appeared quite irregular under SEM observation, showing deteriorated parts characterized by high porosity (especially at the high and highest part of the column). The surface of the foils of the Mellapak is covered by a large amount of deposits clearly visible to the naked eye. The microscopically observations revealed that the deposits are made of crystalline structures with different shapes and morphologies, pointing out to different precipitation events.

The main constituents of the deposits are identified as Lead Hydroxide Oxide and Lead Oxide Carbonate Hydroxide by x-ray diffraction; these compounds, despite fitting satisfactorily some reflections, do not allow the indexing of the whole peaks of the spectra. Different hypotheses are formulated on the origin of the observed microstructures, ascribable to a combination of several factors, as impurities within LiPb and/or as secondary products of the cleaning process performed to the GLC

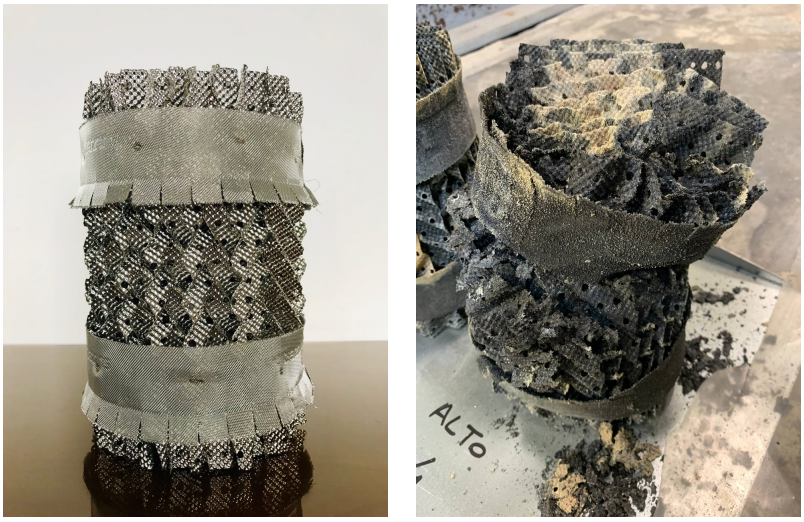

(a) *Virgin packing* **(b)** *Packing after exposure*

Figure 6.12. Example of a virgin packing and appearance of the packing on the top of the column after the experimental campaign

before the start of the experimental campaign (by acetic acid and hydrogen peroxide in water [87]), and/or ingress of oxygen/atmospheric gasses during the operation.

While considering the Mellapak net (Figure 6.15), the morphology was not detectable since the entire material was covered by deposits of crystals and/or was in a decohesioned state.

Generally, every sample from each part of the extractor column showed the presence of several crystals on the surface, with different shapes and dimensions. The dimensions vary from values smaller than 10 µm to several tens of microns.

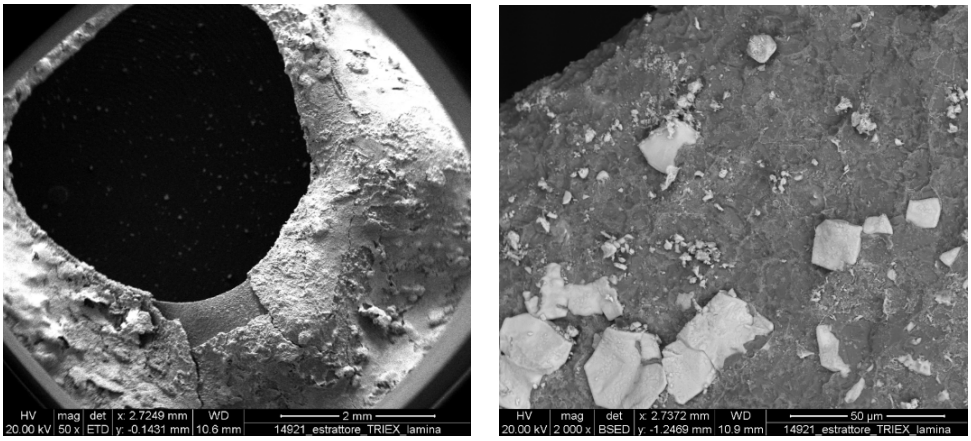

(a) *50X, under ETD (Everhart-Thornley Detector)* **(b)** *2000X, under BSED (Back-Scattered Electron Detector)*

Figure 6.13. Surface SEM micrographs of metal foil from the middle-low part of the extractor column

In order to limit the steel corrosion, good practices can be made, for a lack of a

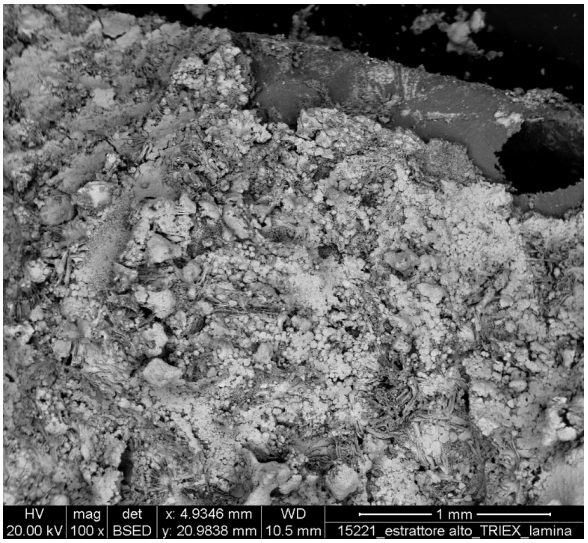

Figure 6.14. Surface SEM micrograph (100X, under BSED) showing the Mellapak foil from the high part of the extractor column

better understanding of the involved physical processes, to avoid the formation of deposits of lead compounds. A follow-up experimental campaign is currently being prepared where:

- Mellapak elements will be realised in C22 ferritic-martensitic steel, more resistant to the corrosive attack of LiPb.
- Periodically monitor the composition of the LiPb circulating in the loop through sampling and analysis utilising techniques such as the ICP (Inductively Coupled Plasma) spectroscopy [88].
- Prevent the entry of oxygen, nitrogen and water vapour by using high purity process gas or using oxygen filters on the gas lines.

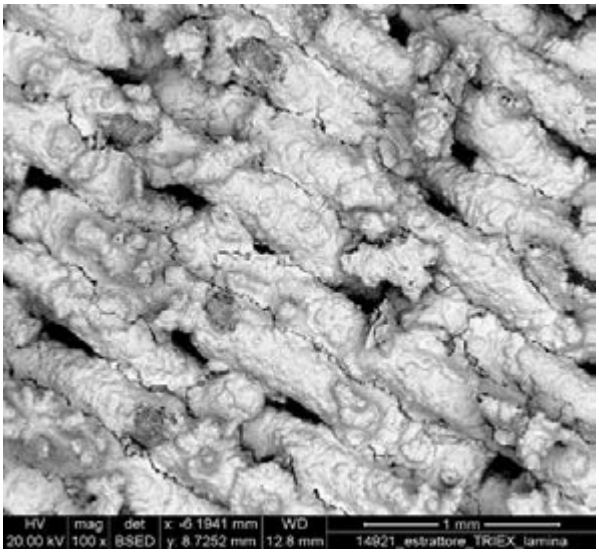

Figure 6.15. Surface SEM micrographs (100X, under BSED) of Mellapak net from the middle-low part of the extractor column

6.3 Main outcomes of the activities on the Gas-Liquid Contactor technology

The efficiency of the Gas-Liquid Contactor was investigated in an experimental campaign in TRIEX-II facility. The tests were executed measuring the hydrogen partial pressure in LiPb with permeation sensors before and after a 32 h extraction. The efficiency was calculated as the difference between the square roots of the average initial and final partial pressures divided by the root of the average initial one. While the HLM 735 sensor does not present a leakage, the measurement of HLM 734 was corrected by subtracting the interpolated leakage.

The results of the experimental campaign show that the calculated efficiency was about 6% in 32h in the first five tests, when the hydrogen partial pressure was higher than 60 Pa. A drop in efficiency is evident when the hydrogen partial pressure reached values below 60 Pa.

Being the efficiencies so low, the packings were examined, finding lack of integrity and general signs of corrosion.

Part III

Anti-permeation Coatings and Compatibility of Materials with LiPb

Chapter 7

Activities on APRIL facility

As said in Part I anti-permeation barriers are needed for fusion and fission reactors (LFR) in order to reduce tritium contamination of the water coolant. Alumina coatings (Al_2O_3) manufactured by PLD (Pulsed Laser Deposition) or ALD (Atomic Layer Deposition) were identified as some of the most promising barriers. For this reason, in the framework of TRANSAT (TRANSversal Actions for Tritium) project, the work had the aim of experimentally investigating the PRF of the coating technologies, starting with LFR operative conditions. For this objective, APRIL (Alumina-coating for tritium Permeation Reduction for Innovative LFR) facility was designed and manufactured to characterize the PRF of candidate coatings in static conditions representative of those envisioned for the ALFRED steam generator. TRANSAT project aimed to address the challenges related to tritium release mitigation strategies and waste management improvement, and refine knowledge in the fields of radiotoxicity, radiobiology, and dosimetry. The project contributed to improve the knowledge on tritium management in fission and fusion facilities.

The activities of the task were divided in 2 steps:

- design and manufacturing of APRIL facility
- experimental campaign at ALFRED operative conditions

In the following section, APRIL facility and LFR steam generator mock-ups are described, while in the Section 7.2 the experimental campaign is reported.

7.1 APRIL description

7.1.1 Mock-up manufacturing and coatings

The ALFRED heat exchanger design by Ansaldo is constituted by 1" Bayonet tubes in AISI 316. In order to test the PLD coating in APRIL facility, 3 small mock-ups of steam generator tubes have been manufactured by ENEA and coated by IIT (Italian Institute of Technology), Figure 7.1.

The tubes manufactured are 300 mm long and have 1" Swagelok diameter (about 25.4 mm) and a thickness of 0.083" (about 2.1 mm), sufficient to withstand the test conditions of 480 °C and 100 bar. The 1" tubes were welded with a closing cap, Figure 7.2, and Non-Destructive Testing (NDT) of the weld was performed by X-ray.

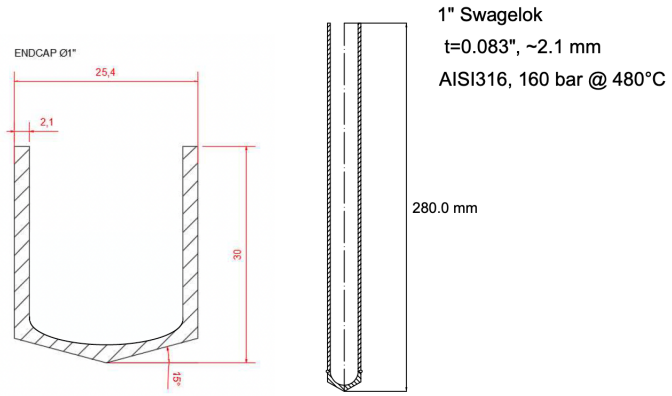

(a) *Sketch of APRIL mock-up cap* **(b)** *Sketch APRIL mock-up tube*

Figure 7.1. Sketch of APRIL mock-up

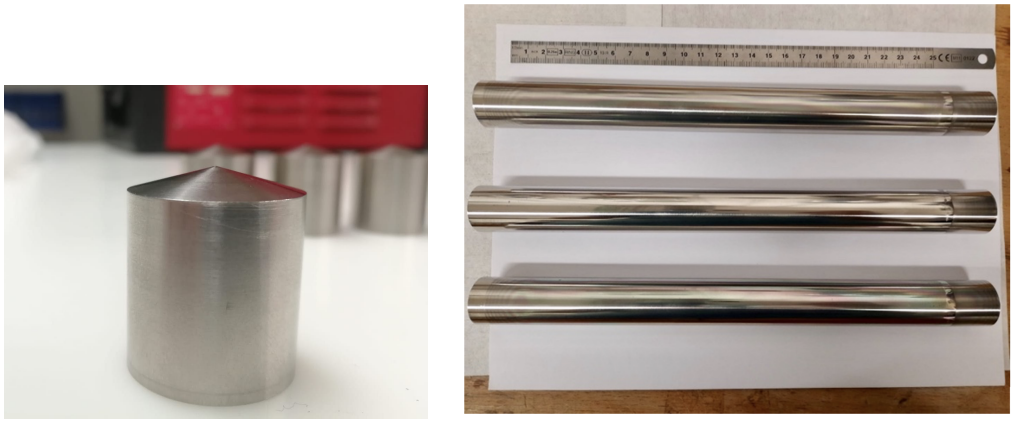

(a) *APRIL mock-ups cap* **(b)** *APRIL mock-ups tube*

Figure 7.2. APRIL mock-ups

Additionally, a pressurization test at 200 bar was carried out to assess the resistance of the assembly.

Once the mock-ups were manufactured, they were sent to IIT that proceeded with the realization of the coatings on 2 of the 3 tubes. Due to the technical limitations of PLD technology only 200 mm of the total pipe length have been coated, which has been the only one inserted in the gas chamber. The tubes of the mock-up were initially grounded with SiC paper with increasing grit (180, 400, 800, 1200, 2400), then they were mirror-polished with diamond pastes having different grain size (6 µm, 3 µm and 1 µm). Secondly, the samples were sonicated in isopropanol for 30 minutes in order to remove possible residues of the polishing procedure. At the end, they were dried with nitrogen and put in the deposition chamber using a specific clamping system. Vacuum was made in the chamber (10^{-4} Pa) and a further *in situ* cleaning procedure was performed using ionized argon gas accelerated towards the steel substrate (90 minutes treatment). Finally, the deposition was started using the

GEN-III recipe ([21]), which foresees a background oxygen pressure of 0.15 Pa, an energy fluence on the solid target of about 4 J/cm^2 and a laser pulse rate of 50 Hz. The coating was deposited uniformly on the external surface of the sample with a nominal thickness of 3 µm.

7.1.2 Description of APRIL facility

APRIL is mainly composed of a test section, constituted by the 3 ALFRED heat exchanger pipes, which are inserted in a gas chamber.

Each mock-up is filled with pressurized water (480 °C and 100 bar). Two tubes are coated with an alumina layer of 3 µm thickness, made with PLD technique, while one pipe is uncoated. The tubes, closed at the bottom with a welded cap, are connected through 3 valves to a collector and to a loading water tank. The 3 valves allow to isolate the 3 mock-ups during the test.

During the tests, the gas chamber, Figure 7.3a and Figure 7.3b, is filled with helium with a known concentration of deuterium (0.5 %). It has a volume of 130 l and it is equipped with a rupture disk, two thermocouples and a piezoresistive pressure transducer. Moreover, it is connected to a gas line and a vacuum line. A proportional valve activated by the signal of the pressure transducer allows to constantly control the gas pressure in the chamber. The same system controls the pressure in the mock-ups during the heating phase.

The entire facility is heated by heating cables installed on the external walls of the chamber and on the part of the pipes outside the chamber. The internal part of the pipes is heated by thermal conduction through the pipes themselves and by the combined contribution of heat radiated by the walls of the chamber and conducted by the helium filling it.

As the procurement of the three valves that should isolate the pipes from the main water line was in delay, the first experimental campaign was performed with a slightly different configuration: each pipe has been lengthened so that the pressure at the testing temperature would not overcome 100 bar. Then, water was poured manually into each pipe, closed at the end with a Swagelok cap, Figure 7.3c.

In Figure 7.4, the main window of the DACS (Data Acquisition and Control System) of the facility is shown. Table 7.1 and Table 7.2 report the design parameters and the operating conditions of APRIL.

Table 7.1. APRIL operative conditions

Parameter	Value	Unit
Operative temperature	480	°C
Deuterium partial pressure	5000	ppm
Gas pressure in the chamber	1	barg
Water pressure in the tubes	50	barg

Table 7.2. Design parameters

Parameter	Value	Unit
Maximum gas pressure in the chamber (at 550 °C)	3	bar
Maximum steam pressure in the tubes (at 600 °C)	180	bar

7.1.3 Main components and P&ID

In this paragraph, the APRIL main components are detailed and the P&ID is shown in Figure 7.5. In purple, the pressure transducers or the vacuum transducer are represented. The process thermocouples are drawn in green, the control thermocouples of the heating cables and safety thermocouples one are respectively in blue and in red. The bold tubes represent the coated one, the red lines are the heating cables and S02 is the loading tank.

The water is loaded by this tank and it filled the water line, including the test section. The gas chamber is filled through the gas line that are connected with two tanks, one of pure helium and one of helium and deuterium at the test concentration. Thanks to the heating cables, the temperature reaches the test conditions while the pressure, in both the water side and the gas side, is controlled by the pressure transducers that automatically open the pneumatic check valves to discharge steam/gas when the pressure increase test values. All the valves are normally closed except for the two check valves.

Gas chamber

The chamber was designed to withstand a maximum pressure of 3 bar at about 550 °C . A check bellows sealed valve, supplied by Swagelok, maintains a pressure of 1.2 bar during the heating up of the gas. The chamber has 3 penetrations for the passage of the tubes, 1 penetration for connecting the gas line, 2 penetrations for the type K thermocouples and 1 penetration for the safety valve. The chamber guarantees tightness in low vacuum and overpressure.

Piping

APRIL presents a water/steam line, a gas line and a vacuum line.

Water line

The three 1" mock-up tubes are connected to the ½" water line by three ½" bellows sealed valves, supplied by Swagelok, and they must withstand a pressure of 100 bar and an internal operating water temperature of 480 °C. The pressure in the mock-up pipes is measured by 3 pressure transducers supplied by Gefran and based on the piezoresistive principle. These instruments combine the high temperature resistance (they can withstand up to 538 °C) with a high-pressure rating (range of measurement: 0-200bar), making possible their use in APRIL. This is possible thanks to a construction principle based on hydraulic transmission of pressure by an incompressible transmission liquid (NaK). The pressure transducers are also

equipped with a type J thermocouple to monitor the mambrane temperature. Their accuracy is 0.25% of FSO.

Gas and Vacuum lines

The gas and vacuum lines have a diameter of ¼" and can withstand a minimum pressure of 10^{-2} mbar and a maximum pressure of 5 bar. A multi-stage root pump by Pfeiffer is used to pump vacuum in the facility, both in the water lines and in the gas chamber. The same pump is used to degas the facility. The vacuum line is equipped with an Edwards Active Pirani vacuum pressure transducer, supplied by 5 Pa (range of measure: atmosphere to 10^{-3} mbar).

Compressed air line

A compressed air line at 6 bar is present to move the pneumatic valves.

Heating system

The heaters consist of 1 heating cable for the S1 chamber and 4 heating bands for the water line. The installed power is about 5 kW. The chamber and the water line are thermally insulated with rockwool layers. The temperature operating conditions are as follows:

- Design temperature of the gas chamber filled argon+deuterium: 550 °C
- Nominal operating temperature of steam: 480 °C

The regulation of the heating system takes place through a PID controller. A safety thermocouple and a control thermocouple are installed on each heating element. The former monitors the temperature of the heater and protects it by allowing the control system to switch it off when the temperature rises above a limit that the operator can set up in the DACS (normally 600 °C is used as maximum temperature of the heaters). The latter measures the temperature of the heated component and its signal serves as input for the PID controller. Attention is given to the installation of the control thermocouple, as it is important to avoid both cold and hot spots, such as flanges or places that are heated simultaneously by two heating elements.

7.1.4 Considerations on hydrogen regulations

The main regulations and technical standards considered for application with hydrogen are:

- Standard EN 60079-10-1: 2016 "Explosive atmospheres. Part 10-1: Classification of areas - Explosive gas atmospheres";
- Standard IEC 80079-20-1: 2017 "Explosive atmospheres. Part 20-1. Material characteristic for gas and vapors classification - Test methods and data".

In this application, it is not foreseen that hydrogen isotopes can accumulate, so that the concentration will always be below the LEL (lower explosion level) of 4%.

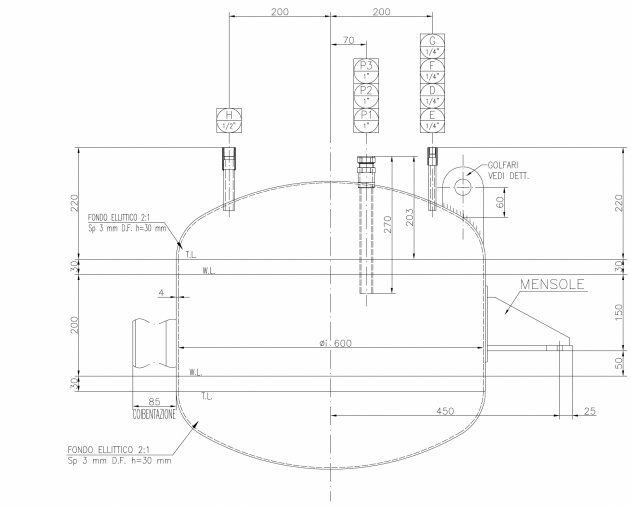

(a) *Sketch of APRIL chamber*

(b) *APRIL chamber*

(c) *Current APRIL configuration*

Figure 7.3. APRIL facility

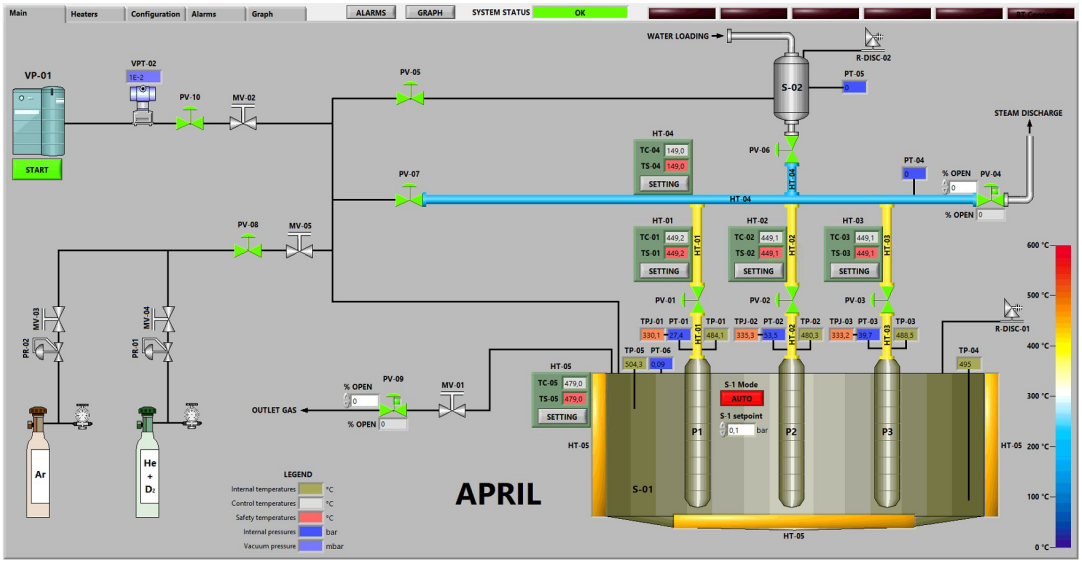

Figure 7.4. The main window of APRIL Data Acquisition and Control System

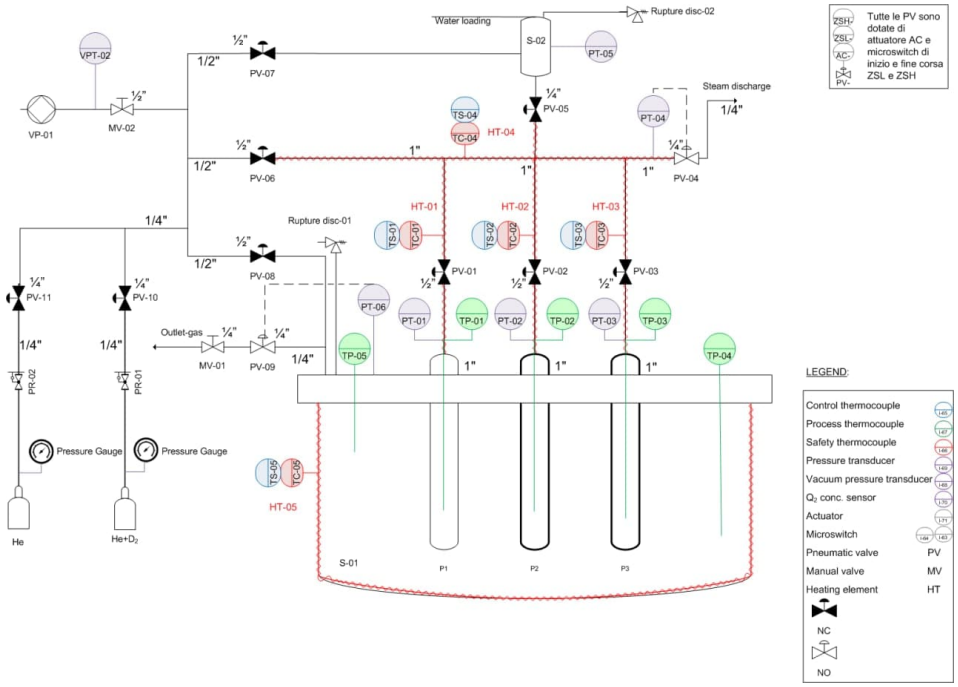

Figure 7.5. P&ID of APRIL

7.2 APRIL Experimental campaign

7.2.1 Start-up procedure

The start-up procedure for APRIL facility is described below.

First of all, to degas the facility from the trapped oxygen, hydrogen and other impurities, the system is preheated to a temperature of 150 °C with a thermal gradient of 10 °C/h and vacuum is pumped in the heated system with the scroll pump until 0.1 mbar are reached. The system is kept for 24 hours at the temperature and pressure set for degassing.

After that, the system is filled with pure He at 1 bar and the temperature of the facility is brought back to 20 °C. At this point, the loading of the water begins. The valve of the water tank is opened and water enters in the pipes (the water tank is initially filled with water and He at 1 bar). When the 3 pipes P1, P2 and P3 of the mock-up are completely filled with water, the water tank valve is closed.

The next step is to reach the operative temperature by setting the heating bands/cables at 480 °C. The check valves maintain the pressure at 100 bar in the water line and at 1.1 bar in the gas chamber, compensating for the increase of the line pressure by venting steam and gas. When the operative conditions are reached, vacuum is made again in the gas chamber to substitute the pure helium with He+D_2 at test partial pressure.

Due to the delay in the supply of the water loading tank, 8 ml of pure water were manually introduced in each pipe. The quantity of water used was calculated considering the required final pressure and temperature in the pipes and the minimum amount of water requested to measure the D_2O/HDO permeated in the water pipes. This quantity is large enough for the measurement system that detects HDO and allows to quantify the PRF of the coatings and to not exceed the design pressure of the tubes. However, this quantity is also small enough to not overcome the design pressure of the facility during the warming up.

7.2.2 Experimental campaign

The facility started to be heated up with a temperature gradient of 10 °C/h, then degassed for 3 days, in order to remove oxygen and moisture from the gas chamber and it reached the operating conditions (pipes at 480 °C) after about 1 week. Then, the gas chamber was firstly loaded with He+D_2 (0.5%) to start the permeation experiment.

Analytical evaluations showed that the concentration of deuterium in helium constantly reduces during the test because of permeation through the chamber walls (undesired) and towards the pipes (aim of the test). For this reason, the gas mixture in the chamber was periodically changed by pumping vacuum for a short time (2 minutes) and subsequently filling the chamber again from the gas cylinder. In this way, an almost constant concentration was maintained on the external side of the pipes. The test was completed after 81 hours of operation at 480 °C.

This duration was decided after a preliminary simulation, made in collaboration with Politecnico di Torino, to analyze the kinetics of deuterium transport in APRIL facility. The preliminary analysis was developed with COMSOL Multiphysics on the uncoated pipe [89]. This analysis was necessary to have an estimation of the

permeation flux and the time needed to reach the equilibrium condition of HDO species in water during the experimental campaign.

The results of the simulation indicated that the 95% equilibrium time, i.e. the time to reach the 95% of the asymptotic value of the permeation flux, is about 2 h. The time needed to reach 95% of the asymptotic deuterium concentration in water is 14 days. Finally, PERI-II facility, a device at ENEA Brasimone that has been used to characterize the PLD performances in gas phase, showed that the PRF is about 35 for the coatings under testing [89]. An estimation of the test time can be done by multiplying the PERI-II PRF by the 2 h obtained from the simulations.

Therefore, the test time was conservatively chosen to be 81 h, so that also the flux in the tube with coating could reach the steady state. When the steady state is reached, the flux does not depend on time anymore and so it is possible to calculate the PRF as the ratio between the concentration of HDO in the tubes. The time of the test has to be less than 14 days as the equilibrium concentration in the uncoated tube has not to be reached to make possible to use this approach. Indeed, if the equilibrium conditions were reached in one tube, the permeation would macroscopically stop and this would introduce an error in the calculation of the PRF.

7.2.3 Results

At the end of the experiment the facility was cooled down and the water inside the uncoated tube and inside one of the coated ones was collected. The samples were sent to the Laborator Izotopi Stabili of ICSI for being analyzed. The samples were analyzed with an infrared spectrometer based on light adsorption delivered by Bruker company. This infrared (IR) spectrometer used can be calibrated both at lower and high deuterium concentrations. Considering the test operative conditions, IR was calibrated for low concentrations of HDO in H_2O. A calibration curve that gives less than 5% deviation is achievable. The carried uncertainty is calculated using an expansion factor K=2, which corresponds to a confidence level of approximately 95%.

The measured concentration of deuterium in the sample coming from the pipes with and without coating are reported in Table 7.3. As the average deuterium concentration in regular water is 144 ppm, subtracting this background from the measured values, it is possible to evaluate the deuterium permeated into the pipes Table 7.4. From these values, a PRF of 13.5 can be evaluated as a ratio of the concentrations.

A measurement of the background deuterium concentration in the water used in the tests is proposed for future experiments in order to have more accurate data. The fact that the PRF resulted to be 13.5 confirms that the assumption on the test duration was good. Indeed, a PRF higher than that obtained with PERI-II would have meant that a steady flux was not achieved during the test, forcing to repeat it. The lower PRF is likely due to the presence of the water that change the kinetics of permeation with the isotopic exchange phenomenon. The isotopic exchange consists in the substitution of an atom of water hydrogen with one of the permeated deuterium, this reaction increases the permeation rate.

Table 7.3. Deuterium concentration in the samples

Sample	Deuterium ppm	Uncertain ppm
Pipe without coating	523	±6
Pipe with coating	172	±2

Table 7.4. Deuterium concentration in the samples after the background subtractions

Sample	Deuterium ppm	Uncertain ppm
Pipe without coating	379	±6
Pipe with coating	28	±2

7.3 Main outcomes of the activities on APRIL

In this section, the activities to evaluate the PRF in presence of water of the alumina anti-permeation barriers deposited with PLD technique are described.

The work was organized in three phases: the design of APRIL facility, the manufacturing of the facility and of the mock-ups and the first test at ALFRED operative conditions (water at 480 °C, deuterium concentration in the gas phase of 0.5%).

After the design phase was concluded, three tubes with the same geometry of the ALFRED Heat Exchanger ones were manufactured, two of them were coated (3 µm thickness) and all of them were installed in APRIL.

An experimental test was performed with a total duration of 81 hours, following some considerations based on the results of pre-test simulations with COMSOL.

The water samples extracted from the facility were analyzed by IR spectrometry and, after subtracting the natural deuterium abundance in water, a deuterium concentration of 379 ppm was found in the water contained in the bare pipe, while 28 ppm were found in the coated pipe. These data led to a calculated PRF of about 13.5.

Chapter 8

Compatibility of Materials with LiPb

A corrosion campaign was organized and carried out in IELLLO facility during 2020-2021 with the aim of obtaining data on the behavior of relevant materials for this thesis in flowing high temperature LiPb. It was decided to characterize niobium and vanadium samples, as they are the two main candidate materials for the PAV membrane. Moreover, P22 samples were also exposed as TRIEX-II is made of this ferritic steel. Finally, EUROFER samples coated with alumina by ALD and PLD were tested.

Scanning electron microscope (SEM), Energy-dispersive X-rays (EDX) and X-ray diffraction (XRD) are the techniques used to characterize the materials. SEM analysis has a resolution of the nanometer scale and uses the interaction between electrons emitted by a filament with the atoms of the sample. The interaction produces different effects, such as the incident electrons backscattering (BSE) from deeper regions of the sample or the emission of secondary electrons (SE) from the surface, that give information about the composition and the surface geometry. Moreover, these interactions can produce also energy-dispersive X-rays (EDX) that are characteristic of the element that emitted them, so a spectrum with several peaks is generated. This analysis gives information not only on the elements present on the sample but also on their concentration in a given region. Finally, XRD is a technique that uses incident X-rays on a sample to characterize its crystallographic structure, including the grain size, the lattice parameters and defects. The intensities and angles of the scattered X-rays are used to identify the elements according to their diffraction.

8.1 Materials and methods

The specimens were hosted in a test section, shown in Figure 8.1, composed of three 1” pipes bolted together in series and installed in IELLLO facility. Each pipe hosted a rod of specimens to be removed at the end of each exposure period (1000, 2000 and 4000 h). The first pipe of the three 1” pipes that LiPb wets at the entrance of the test section is longer than the other two as a long dummy specimen was added to ensure fully developed flow at the location of the specimens to be characterized.

The distance to develop the flow was evaluated following the criterion $x/D > 10$ [90], where D is the hydraulic diameter. In order to keep this feature for the entire campaign, the longest pipe hosted the specimens for an exposure of 4000 h.

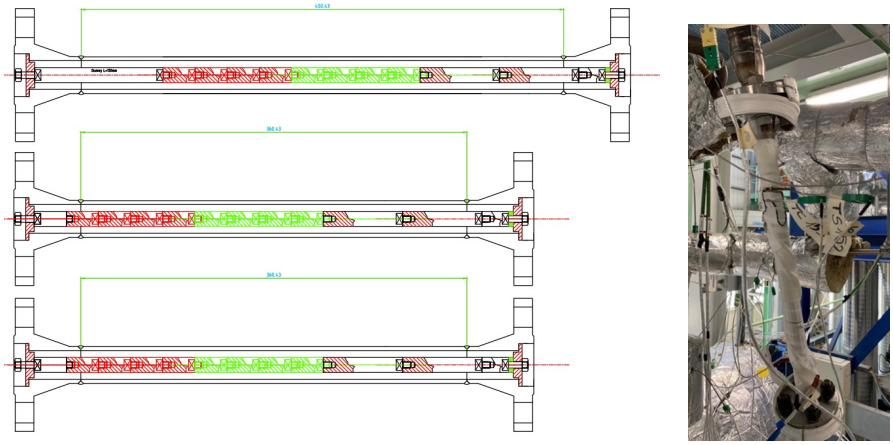

(a) **(b)**

Figure 8.1. Drawing of the three parts composing the test section (a) and picture of the test section before thermal insulation (b)

Specimen geometries are shown in Figure 8.2. Niobium and vanadium bars were supplied by Goodfellow with nominal purity 99.9% *wt.* and 99.8% *wt.*, respectively (main impurities being 255 ppm of Ta, 230 ppm of O, <100 ppm of W and 35 ppm of N for niobium and 300 ppm of Si, 70 ppm of Fe and 15 ppm of Cr for vanadium). The bars were machined to the required diameter (14 mm) by 3T Srl. P22 specimens were machined at the workshop of ENEA Brasimone R.C. starting from bars available in the warehouse. The LiPb exposed surface was 1318.8 mm^2 for the Nb and V specimens. Dummy specimens are made of AISI316L. Alumina-coated EUROFER specimens were also exposed to flowing LiPb in IELLLO facility (whose description can be found in [70]) during this campaign and their geometries are shown in 8.2.

The twelve niobium specimens were examined at SEM in cross-section and surface view and by XRD. One non-exposed specimen was also examined at SEM as a reference. Three specimens per exposure were also cleaned in a chemical solution made of acetic acid, hydrogen peroxide and ethanol (1:1:1 ratio) for 24 h and then weighted. The same examinations were performed on the twelve vanadium specimens, with the exception of weight loss analysis. Vanadium is sensitive to oxidative aqueous environment and, as a consequence, it is attacked by typical chemical solutions usually used to remove residual Pb, i.e. nitric acid solutions and hydrogen peroxide solutions. For this reason a methodology to clean the V specimens is under investigation. The three P22 specimens, one per exposure time, were analyzed at SEM in cross-section and surface view. Finally, the six EUROFER samples coated with alumina by PLD and ALD techniques were cleaned with chemical solution to remove residual LiPb on the surface and then examined with high-resolution SEM in cross-sectional and longitudinal view.

The characterization of the samples, i.e. their morphology and their microstruc-

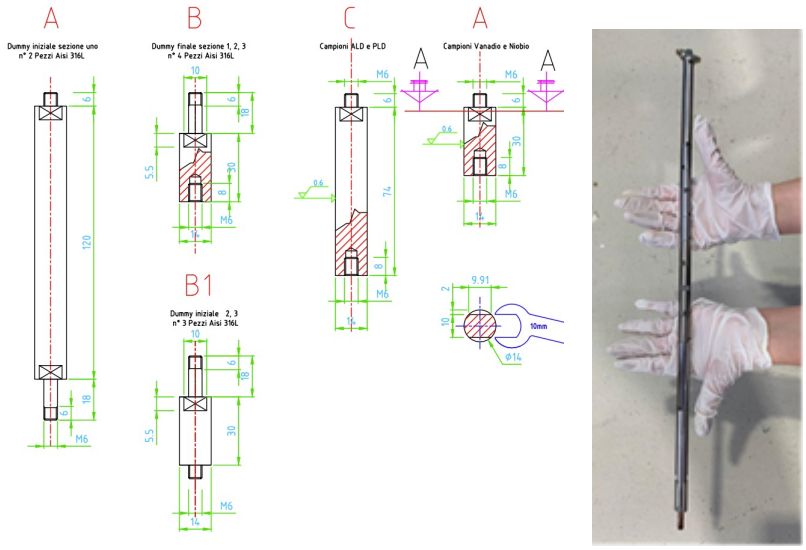

(a) (b)

Figure 8.2. Drawings of the specimens exposed to LiPb in this campaign (a) and picture of a rod of specimens before insertion in the test section (b)

ture, was performed by Scanning Electron Microscopy (SEM-FEI QUANTA INSPECT-S) coupled with Energy Dispersive X-ray spectroscopy (EDX-EDAX Genesis). XRD investigations were performed by Philips X Pert-Pro diffractometer equipped with $CuK\alpha$ source.

8.2 Membrane materials

In the Water Cooled Lithium-Lead Breeding Blanket (WCLL BB) [8], LiPb slowly flows through the Breeding Units and interacts with neutrons coming from the plasma chamber, generating tritium, which has to be removed from the liquid alloy to be used as a fuel for the ractor itself. Permeator Against Vacuum is one of the candidate technologies for this task and is based on the tritium permeation through permeable membranes [91]. The candidate materials for membranes are niobium and vanadium [75]. Although mock-ups of the Tritium Extraction Unit are currently being manufactured with both niobium (Nb) [49] and vanadium (V) [48] as membrane materials, their compatibility with LiPb was only studied in stagnant conditions by Feuerstein et al. [92] and Grabner et al. [93]. Both references deemed these elements to be very stable in LiPb up to 650°C. The solubility of V is reported to be 1.1 and 3.5 *ppmw* at 500 °C and 600 °C respectively, whereas the solubility of Nb is reported to be 0.053 *ppmw* at 600 °C [92]. Dissolution rate were found to be about 0.01 $g/m^2 \cdot d$ at 550 °C and below 0.004 $g/m^2 \cdot d$ for Nb at 600 °C [93]. Studies in flowing conditions are not available for the pure elements, although Adelhelm et al. [94] and Borgstedt et al. [95] investigated the corrosion of the vanadium alloy V-3Ti-1Si in static and flowing LiPb, proving fairly good corrosion resistance.

Due to the lack of data on the behavior of pure vanadium and pure niobium in flowing LiPb, ENEA decided to perform an experimental characterization in IELLLO

(Integrated European Lead Lithium LOop [96] [70] [97]) at ENEA Brasimone R.C. The tests were carried out at 500 °C and $0.5 m/s$ for exposures of 1000, 2000 and 4000 h. This velocity is the maximum foreseen in the LiPb loops of the WCLL BB, while the temperature was chosen following a conservative approach, as the WCLL LiPb systems are isothermal at 330 °C (although an alternative layout of the loops with a section at 450 °C is under consideration for enhanced tritium extraction efficiency).

P22 ferritic steel samples and alumina coatings deposited on EUROFER samples by ALD and PLD techniques were also exposed to LiPb within the same experimental campaign. The results are shown in Section 8.3 and Section 8.4, respectively. Instead, the following section reports on the results of niobium and vanadium samples.

8.2.1 Niobium

The weight of the specimens before and after the exposure to flowing LiPb was measured with analytical balance with tolerance ± 0.1 mg. The results of the weight loss normalized for the exposed surface and the relative corrosion were reported in Table 8.1 as average values of three weighted specimens. The weight loss is slightly negative for 1000, 2000 and 4000 h and indicates an increase of weight. In addition, the weight gain for 4000 h exposed specimens is slightly higher than 1000 and 2000 h specimens. This slight weight gain could likely depend on traces of LiPb remained inside the screws of the specimens and also on chemical surface modification and interaction with Fe and Ni contaminants (see SEM analyses in Figure 8.3 hereafter). However, the final corrosion values are very low, indicating no significant corrosion/modification of Nb in the operating conditions. These results are in agreement with data obtained in static LiPb by Feuerstein and Grabner, which reported a low solubility of 0.053 ppmw at 600 °C [92].

Table 8.1. Average weight loss and corrosion of Nb specimens after exposure to LiPb with indication of the standard deviation (STD)

Time $[h]$	Δm [g]	STD Δm [g]	$\Delta m/S$ $[g/m^2]$	STD $\Delta m/S$ $[g/m^2]$	Corrosion $[\mu m]$	Density $[g/cm^3]$	STD corrosion $[\mu m]$
1000	-0.0016	0.0033	-1.2	2.5	-0.1	8.57	0.3
2000	-0.0004	0.0013	-0.3	1.0	0.0	8.57	0.1
4000	-0.0053	0.0003	-4.0	0.3	-0.5	8.57	0.0

Figure 8.3 shows cross-section SEM images at comparable magnification of Nb specimens as virgin and after exposure in flowing LiPb for 4000 h. The exposed specimen presents a slightly increased roughness compared to that of the virgin material. The bulk exhibits porosity and likely depends on the material production process.

From the point of view of composition, various line-scans were performed at the interface to evaluate possible diffusion gradients and/or chemical modifications (Figure 8.4). The interface is enriched with Ni and Fe. The contamination with Ni and Fe comes from the LiPb and it is related to corrosion of the loop piping, and the surface enrichment is likely related to the formation of an intermetallic compound. In some areas, surface oxygen is also detected (line 1 and 2, black areas). In other

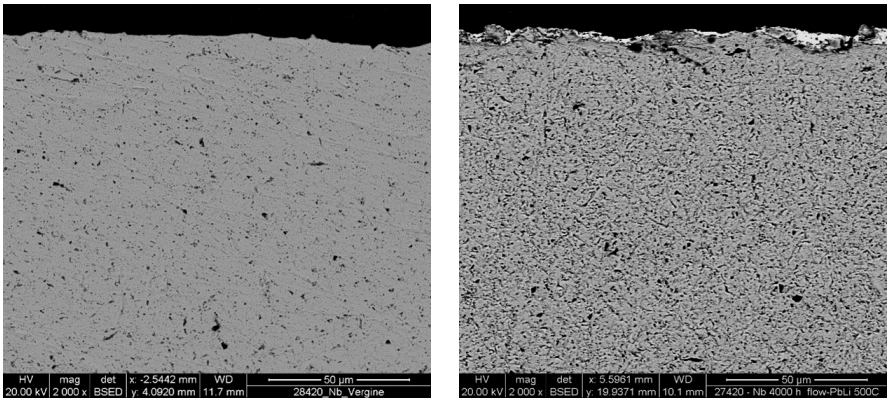

(a) **(b)**

Figure 8.3. Cross-section SEM images at 2000x magnification of a virgin Nb specimen and after 4000 h in flowing LiPb

parts, the intermetallic compound is detached from the interface in the form of particles (line 2) and this intermetallic layer is generally thin. The formation of a thin intermetallic layer on niobium was already observed in liquid Pb at 1000 °C in presence of dissolved Ni, Cr and Fe in the melt [98].

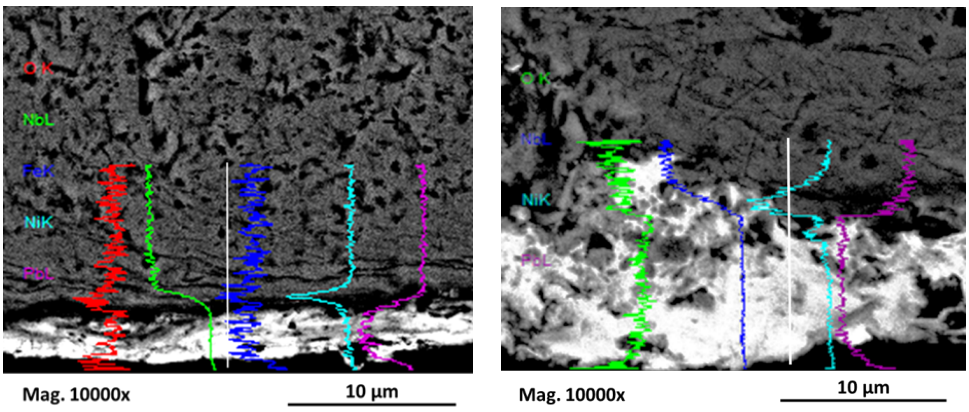

(a) **(b)**

Figure 8.4. EDX line-scans at high magnification of the interface (10000x) in Nb specimens exposed for 4000 h

Surface SEM images at different magnification and EDX compositions are reported in Figure 8.5 only for specimens exposed for 4000 h. The surface has now a grainy/crystalline appearance and contains Nb, Ni (up to 40% *wt.*), Fe and O after cleaning in the chemical solution (even some traces of Pb still remained on the surface). Similar evidences were observed also for 1000 and 2000 h exposed specimens, but the results are not shown here for the sake of brevity. By EDX analyses performed on the specimens exposed to the various times, the amount of Ni on the surface increased with the exposure (from 4 to about 40% *wt.*), whereas the content of Fe decreased (from 8 to about 3% *wt.*), as shown in Table 8.2. High amount of oxygen was found especially for 1000 and 2000 h of exposures.

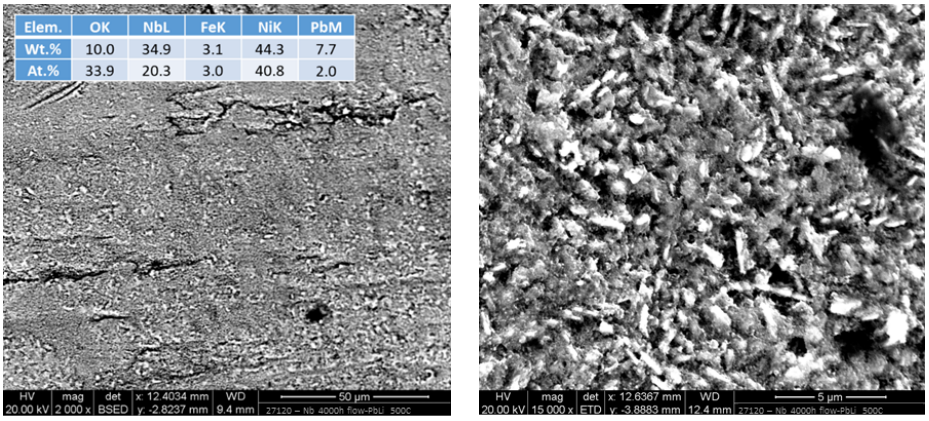

(a) **(b)**

Figure 8.5. Surface SEM images at different magnification of Nb specimen exposed to 4000 h in flowing LiPb, with indication of the surface composition by EDX

Table 8.2. Surface composition of Nb specimens over the exposure times detected by EDX

Time	O		Nb		Ni		Fe	
[*h*]	Wt.%	At.%	Wt.%	At.%	Wt.%	At.%	Wt.%	At.%
1000	12	42	77	47	4	4	8	8
2000	19	55	62	30	16	12	3	3
4000	11	35	38	20	48	42	3	3

From EDX semi-quantitative composition it is difficult to state about the possible compound or compounds formed at the interface. In addition, EDX has a limitation in detecting Li element, which may interact with the surface. By looking at phase diagrams, Nb element is prone to form a variety of intermetallic compounds both with Ni and Fe [99] [100] and isothermal sections at 450 and 500 °C are available for ternary Nb-Ni-Fe phase diagram [101] [102].

In addition, the presence of oxygen, which may interact to form oxides, must be considered. Nb-oxides (Nb_2O_5, NbO_2 and NbO) are thermodynamically instable in LiPb environment (see Ellingham diagram of Figure 8.6) and, if really present on the surface, they may be related to oxidation during draining in hot argon before extraction or due to the formation of more stable mixed oxides (such as LiNb oxides potentially forming by Li interaction). However, thermodynamic data of known LiNb oxides such as $LiNbO_3$ or Li_3NbO_5 are uncertain and data available in literature are not fully consistent to definitively assess the thermodynamic stability in LiPb (Figure 8.7).

XRD spectra have then been performed on 2000 and 4000 h exposed specimens in order to identify possible compounds (Figure 8.8). According to the spectra, Nb was the predominant phase in the 2000 h specimen and traces likely related to $NbNi_3$ and Fe_2Nb were found. To the opposite, Nb_3Ni phase is consistent in the 4000 h exposed specimens, in accordance with the increase of Ni content detected by surface EDX analysis in Table 8.2. The formed phases are in fair agreement with ternary phase diagram section at 500 °C (see Figure 8.9): at 1000 and 2000 h the stable

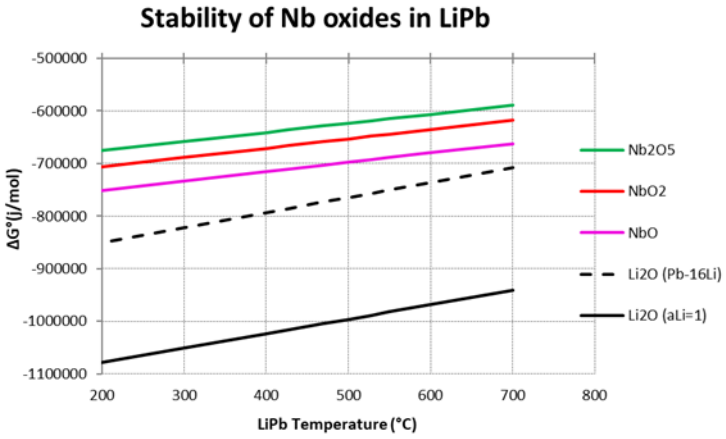

Figure 8.6. Ellingham diagram of Nb oxides in LiPb eutectic. Thermodynamic data for Nb oxides were taken from [103]

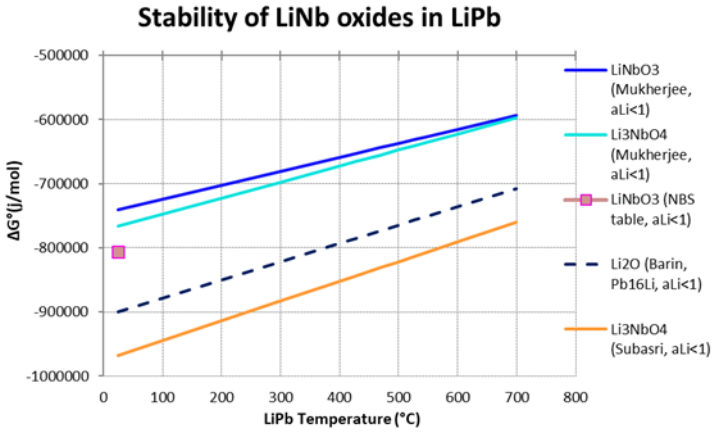

Figure 8.7. Ellingham diagram of LiNb oxides in LiPb eutectic. Thermodynamic data for LiNb oxides were taken from [104] [105] [106]

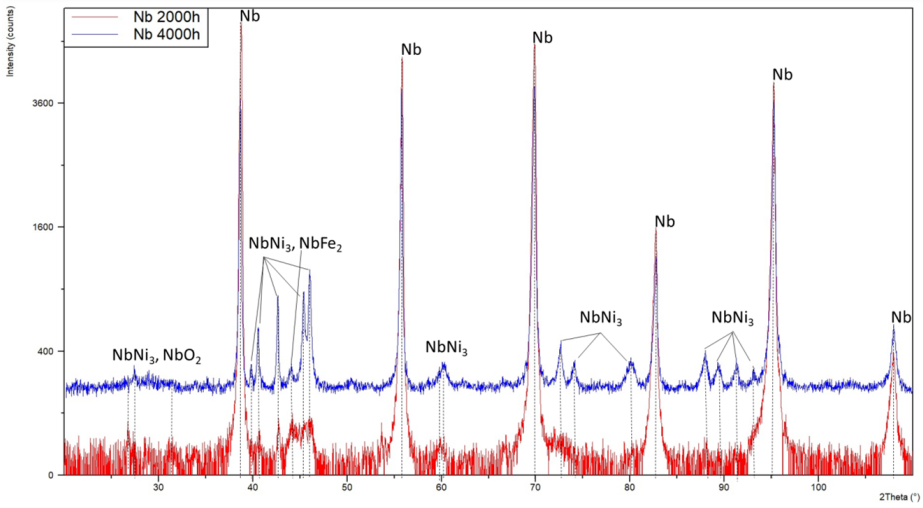

Figure 8.8. XRD pattern for Nb specimens exposed for 2000 h and 4000 h

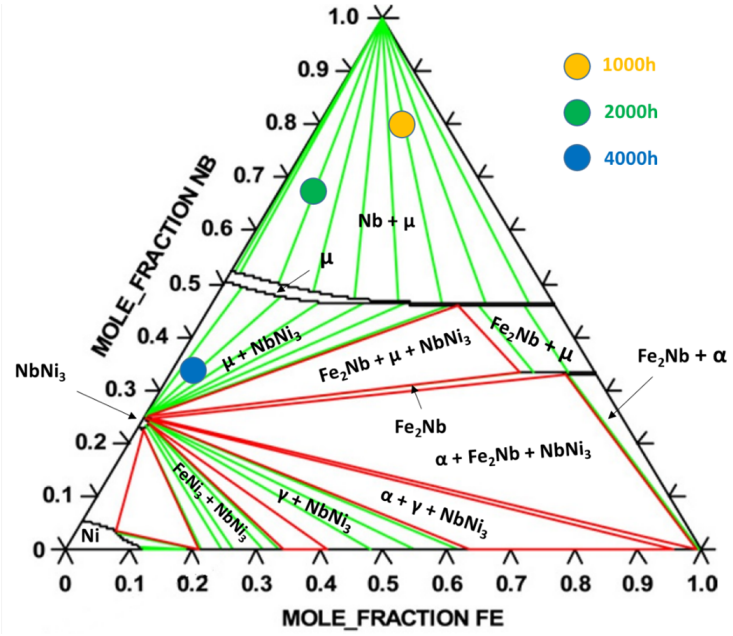

Figure 8.9. Ternary Nb-Ni-Fe phase diagram section at 500 °C (figure adapted from [102] with permission from Elsevier under license 5240860644879). The points correspond to surface composition detected by EDX for the various exposure times

phase is Nb with μ solid solution [107]. To the opposite, the surface enrichment of Ni stabilized the $NbNi_3$ phase at 4000 h, as detected in the XRD spectrum.

8.2.2 Vanadium

Figure 8.10 shows cross-section SEM images at comparable magnification of V specimens as virgin and after exposure in flowing LiPb for 4000 h. Going on with the exposure, the specimens present smoother surfaces compared to that of the virgin

material. The bulk of the specimens exhibits porosity and this likely depends on the material production process.

From the point of view of composition, the surface does not present a well-defined interface. EDX line-scans on high magnification images indicate the presence of a layer enriched with Ni and Fe elements at the interface, likely related to the formation of intermetallics. This enriched layer is about 1.5 μm thick. In addition, the formed layer tends to be detached or dissolved during the exposure. The formation of this layer is highlighted by EDX elemental maps in Figure 8.11 and confirmed by point compositional analysis (Figure 8.12), which shows the presence of Ni, Fe and V in the layer at the interface. The content of Ni and Fe is significant (26% *wt.* and 6% *wt.* respectively) and there is also some oxygen (about 8% *wt.*). The Si content is likely related to the preparation of the samples for the SEM examination.

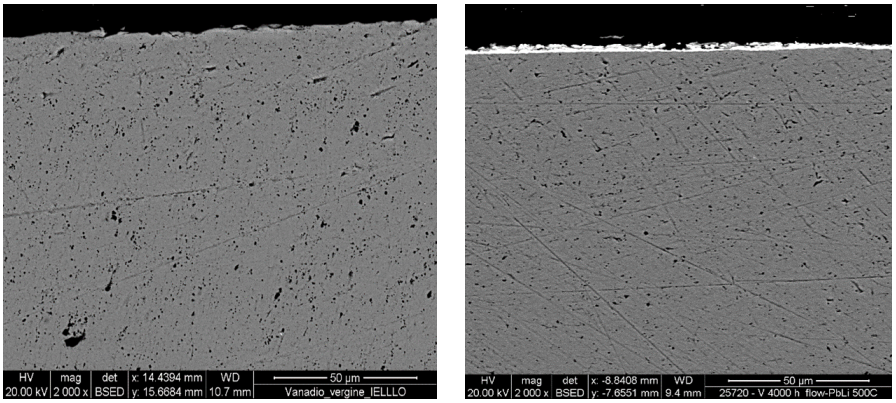

(a) **(b)**

Figure 8.10. Cross-section SEM images at 1800-2000x magnification of virgin V specimen (a) and exposed for 4000 h in flowing LiPb (b)

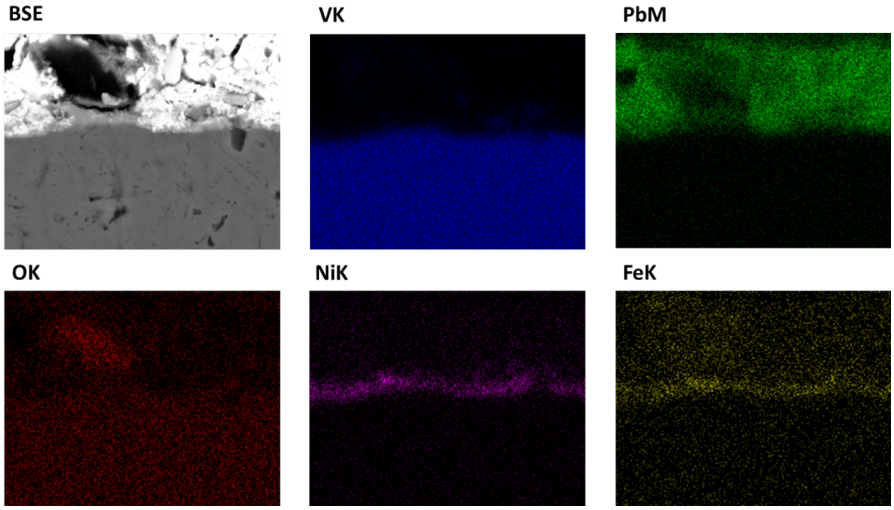

Figure 8.11. Cross-section SEM images of V specimen after 4000 h and elemental maps by EDX

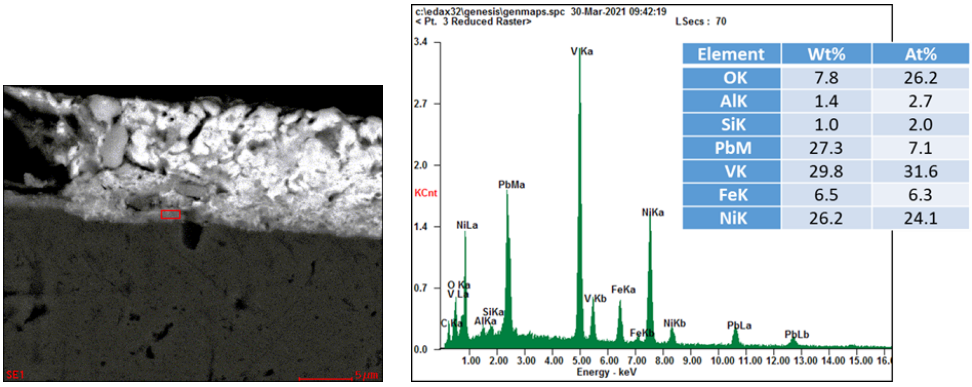

(a) (b)

Figure 8.12. Point EDX elemental composition on Fe, Ni enriched layer on V specimen after 4000 h

Corrosion of V alloys was studied in static and flowing LiPb in the past by Adelhelm et al. [94] and Borgstedt et al. [95], who detected the interaction of V with contaminants. According to the work by Adelhelm, V-3Ti-1Si alloy was tested in static LiPb in stainless steel capsules at 357 and 547 °C for about 1000 h. The adherent LiPb layer on the specimens was not removed for weight loss evaluation and only element composition analysis was performed on the specimens. At 357 °C the surface was basically unaffected and conserved the starting roughness after the exposure, whereas a corrosion attack was detected at 547 °C as a consequence of the interaction with Fe, Cr and Ni contaminants (coming from the corrosion of the steel capsules). The original surface and starting roughness was not anymore recognized after the test and the interface changed into a bubble-shape layer. Borgstedt tested V-3Ti-1Si alloy in flowing LiPb at 550 °C up to 3687 h. V alloy specimens exhibited a weight gain ascribable to an interaction with Fe contaminant and the formation of a thin Fe-composed metal layer on the surface. The formation of an intermetallic layer on V was also observed in liquid Pb at 1000°C in presence of dissolved Ni, Cr and Fe in the melt [98].

The data here reported confirm previous results by Adelhelm and Borgstedt. The interaction is related to the formation of stable intermetallics or solid solutions with Fe and Ni, as shown in Fe-V and Ni-V phase diagrams [108] [109] [110]. Also traces of Al were found in the layer (see Figure 8.12) and Al is prone to form intermetallics with V [111]. The observed “smoothing” effect may be due to dissolution or, most likely, to the formation of an intermetallic layer that tends to dissolve in LiPb. According to Feuerstein and Grabner, the solubility of V is reported to be quite low at 500 °C (1.1 ppmw), suggesting that the formation of the intermetallic compounds may have the primary role over the corrosion.

A summary of the chemical composition of the layer for the various exposure times is reported in Table 8.3. By neglecting Pb content on the surface (not expected to interact with V [112]), the trend of the elements indicates that Ni slightly accumulates with the exposure time whereas Fe content is high at low exposure time (1000 h) and then decreases. Oxygen is constant over time and may be related to oxidation of the adherent LiPb on the surface, since oxygen peak has not been detected through

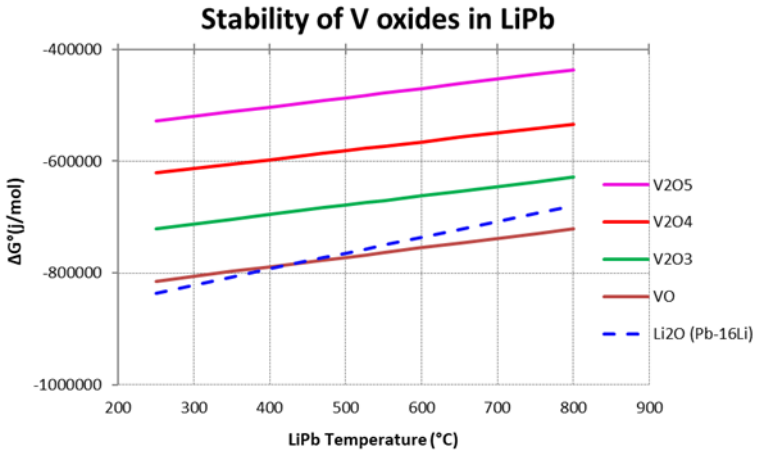

Figure 8.13. Ellingham diagram of V oxides in LiPb eutectic. Thermodynamic data for V oxides were taken from [103]

the line-scans and single V-oxides are not stable in LiPb (Figure 8.13). However, potential interaction of O with V, Li and contaminants to form stable oxides in LiPb eutectic is not to be excluded a priori in the form of traces.

Table 8.3. Surface composition of V specimens over the exposure times detected by EDX. Values at 1000 and 2000 h were obtained through surface EDX on uncleaned specimens, while the values at 4000 h through cross EDX at the interface

Time	O		V		Ni		Fe		Pb	
[*h*]	Wt.%	At.%	Wt.%	At.%	Wt.%	At.%	Wt.%	At.%	Wt.%	At.%
1000	8	33	19	24	16	17	9	11	47	14
2000	11	44	14	17	17	18	4	4	54	17
4000	8	33	30	33	27	25	7	5	28	7

Unfortunately, no isothermal sections around 500 °C are available for ternary phase diagram V-Fe-Ni and so no predictions about the stability of the phases can be performed considering the chemical compositions detected after 1000, 2000 and 4000 h of exposure.

XRD spectrum was collected for 1000 h specimens, that was partially cleaned on corrosive acetic acid and hydrogen peroxide solution (Figure 8.14). As the specimens conserved the intermetallic phase formed by interaction with Fe and Ni in most of the surface, XRD analysis was performed to identify potential compounds. The XRD spectrum indicates the formation of a Ni-V intermetallic phase and the presence of Ni and Fe, which may form solid solutions. In particular, Ni_3V and Ni_2V have peaks in accordance with the present spectrum. According to binary Ni-V phase diagram, formation of these intermetallics is possible in the range of Ni content between $20 - 50\%$ *at.* (cf. [109]).

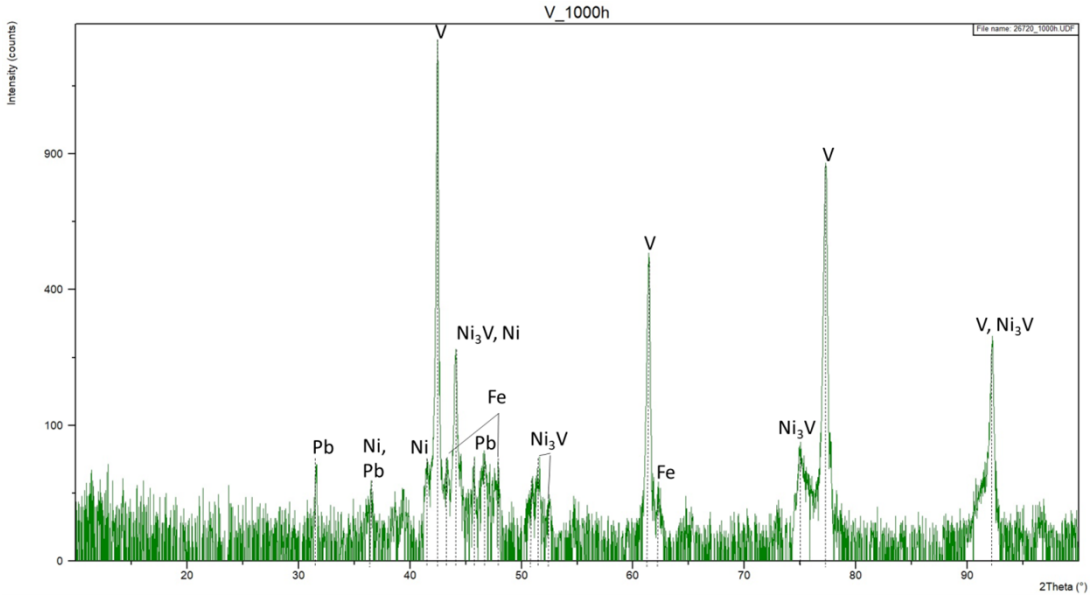

Figure 8.14. XRD pattern for V specimen exposed for 1000 h (cleaned)

8.3 Structural materials

LiPb is a corrosive fluid, whose effect on structural materials is strongly linked with its temperature, its velocity and the amount of impurities dissolved in it [113]. Many studies have been carried out in the past to investigate corrosion on austenitic [114] and ferritic/martensitic steels [115], especially on EUROFER [116], under different operative conditions. Among the structural materials of fusion interest, the behavior of P22 ferritic steel (ASTM A335 Gr. P22) has not been investigated, despite being currently considered as one of the reference materials for the piping of the LiPb loops [117]. For this reason, specimens of P22 steel were exposed to LiPb in the same campaign described in Section 8.2. This section describes the results.

8.3.1 P22 ferritic steel

Figure 8.15 shows cross-section SEM images at lower (2000x) and higher (5000x) magnification of P22 specimens after exposure in flowing LiPb for 4000 h. The surface is affected by LiPb penetration with a depth ranging from 2 to 9 μm. No portions of detached specimen were found near the interface in the LiPb. The surface profile of the specimens appears to be similar between the various exposures and no significant increase of roughness was detected at 4000 h. For the surface examination, a portion of the specimen was cleaned with a soft solution of hydrogen peroxide, acetic acid and ethanol to not degrade the alloy (ratio 1:1:1 diluted up to 10% *vol.*). Significant Cr enrichment was found on the samples surface after 4000 h of exposure, up to about 51% *wt.* (40% *at.*). This strong enrichment is likely due to re-deposition of corrosion products and mostly related to contamination of the LiPb in the loop. The enrichment is confirmed by EDX maps of the elements (Figure 8.16) and by EDX surface analysis on a cleaned portion of the specimen (Figure 8.17).

Surface Cr enrichment and re-deposition increases with the exposure times, as

shown in Table 8.4. Presence of O should be related to the oxidation of the surface with the chemical solution. From SEM images at the lower magnification, the lines of the manufacturing are still visible, whereas at the higher magnification it is possible to observe the grainy appearance of the surface (also detected for 1000 and 2000 h exposed specimens).

As the internal bulk composition profile did not change significantly over the exposure times at the interface (selective leaching of element was not detected) and no detachments were detected, it is to suppose that uniform dissolution and erosion mostly proceeds with a currently unknown corrosion rate.

Table 8.4. Surface composition of P22 specimens over the exposure times detected by EDX

Time	O		Cr		Fe	
[h]	Wt.%	At.%	Wt.%	At.%	Wt.%	At.%
virgin	-	-	2.14	-	95.8	-
1000	3	10	30	29	66	60
2000	9	25	47	40	45	36
4000	8	22	54	46	38	31

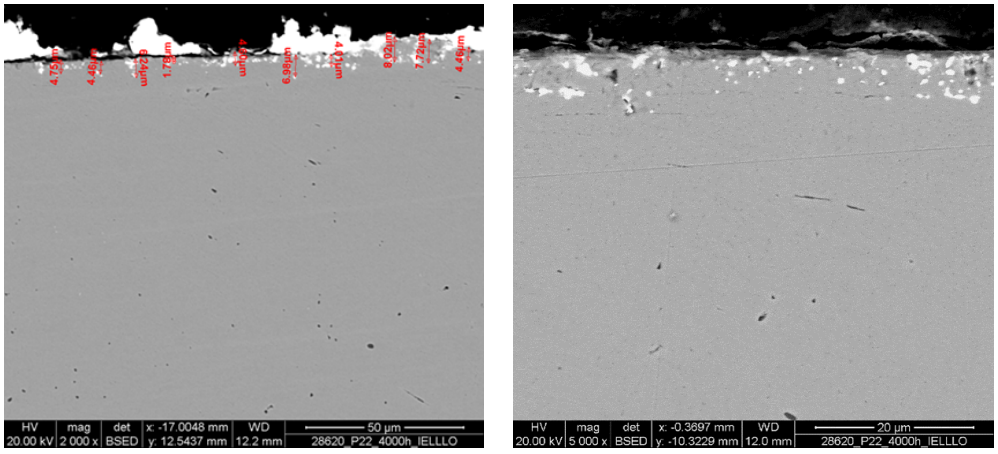

(a) **(b)**

Figure 8.15. Cross-section SEM images at 2000x (a) and 5000x (b) magnification of P22 specimens exposed for 4000 h in flowing LiPb

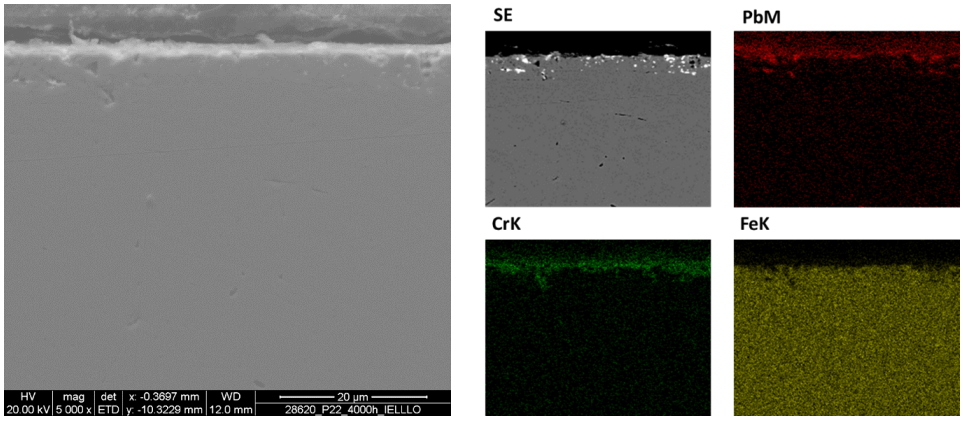

(a) **(b)**

Figure 8.16. Cross-section SEM images at high magnification of P22 specimens exposed for 4000 h and EDX maps showing Cr surface enrichment and LiPb penetration

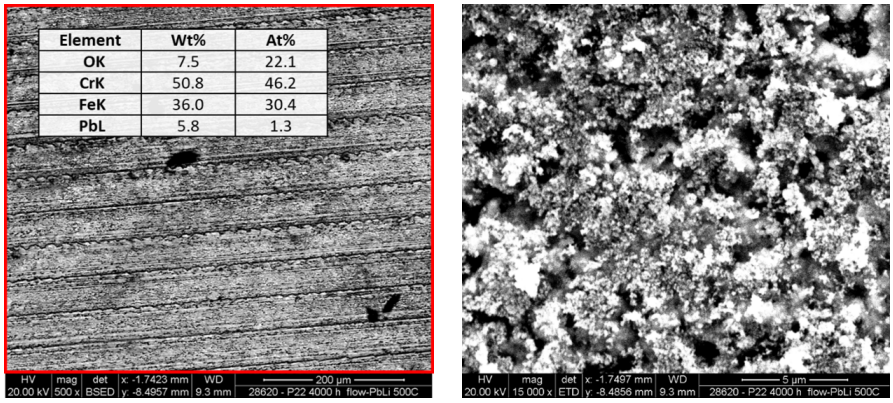

(a) **(b)**

Figure 8.17. Surface SEM images at different magnification of P22 exposed to 4000 h in flowing LiPb, with indication of the surface composition by EDX

8.4 Coatings

Alumina coatings will be likely adopted to minimize corrosion of structural materials and tritium permeation towards the environment. Several production processes are under investigation and require dedicated testing [62] [21]. Among them, Atomic Layer Deposition (ALD) and Pulsed Laser Deposition (PLD), described in detail in Chapter 3 are promising processes but the behavior of coatings made with these techniques in flowing LiPb was still unknown, before the experimental campaign described in Section 8.2 (testing of the coatings made by PLD in static LiPb demonstrated that they maintain their protective characteristics also after long-term exposure [62] [21]). EUROFER samples coated with alumina by PLD and ALD techniques were exposed to LiPb in IELLLO loop and this section descibes their behavior. The PLD coated samples were exposed up to 4000 h, while the ALD coated ones only up to 3000 h, as the samples were supplied in delay. All the samples

were examined by means of a high resolution SEM, that was able to clearly detect also the thin alumina layer deposited by ALD on EUROFER (300 nm of thickness).

Some samples exposed in IELLLO have been analysed at CIEMAT and, later on, at IIT by SIMS (Secondary-Ion Mass Spectrometry), Atomic probe and XPS (X-ray Photoelectron Spectroscopy). The results, obviously not described in this thesis, proved to be quite interesting, showing lithium diffusion into the alumina matrix. The extent of this phenomenon and its consequences on the coating durability are still under discussion, but the scheduled activities on PLD and ALD coatings have been partially stopped waiting for a better understanding of the phenomenon to be reached. For those who are interested, the analyses performed at CIEMAT are partially described in [118].

8.4.1 General discussion on the behavior of PLD and ALD coatings

Exposures of PLD and ALD alumina coatings in flowing LiPb have been performed up to 4000 h for the first one and up to 3000 h for the second one. From the point of view of the chemical interaction and corrosion behavior, both alumina coatings deposited with the two technologies macroscopically resist corrosion by LiPb and the EUROFER below was protected by LiPb corrosion when coating is adherent to the surface. No significant evidences of degradation were found on the coatings both in cross and surface view by EDX, but, as EDX is not able to detect Li elements, it was not possible to exclude the formation of LiAl oxides.

According to thermodynamic stability of Al_2O_3 is stable in LiPb environment due to low activity of Li compared to pure Li. However, alumina may interact with Li to form LiAl oxides which have higher thermodynamic stability compared to Al_2O_3 (see Ellingham diagram of Figure 8.18).

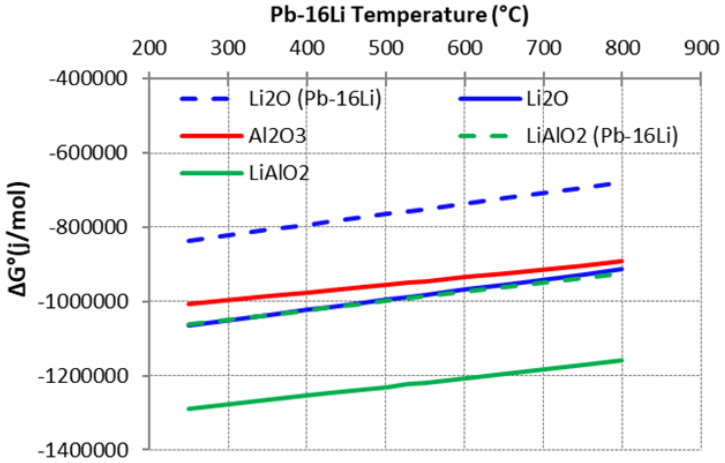

Figure 8.18. Ellingham diagram of Al_2O_3 and $LiAlO_2$ oxides in LiPb eutectic. Thermodynamic data were taken from [103]

Some authors reported about the formation of $LiAlO_2$ oxide at 800 and 550 °C [112] [119]. Specifically, related to alumina coatings, the formation of LiAl-oxides was already detected on PLD coating samples exposed in static LiPb at 550 °C [120].

$LiAl_5O_8$ and $LiAlO_2$ were found in traces in XRD spectrum on PLD coating samples after 4000 h and their formation is supposed to explain the grainy appearance exhibited by the surface of alumina coatings after the exposure in LiPb (detected by surface examination).

About the quality of the coating, PLD alumina layer presents high quality and only few defects were detected by the examination in surface view. For ALD coating, several pit defects and detachments were detected on the surface. These defects appear related to a non-correct preparation of the steel substrate below: bubbles and pits characterizing the substrate are frequently detected. More optimization should be required to minimize the presence of these defects, which may also affect the tritium permeability.

8.4.2 PLD

Alumina coating by PLD was deposited by IIT on EUROFER cylindrical samples with a thickness of 3 μm. Samples exposed for 1000 and 2000 h were examined with a SEM in cross-section and also longitudinally after cleaning with a chemical solution to remove residual LiPb on the surface. Only a selection of the analyses at 1000 and 2000 h is reported in this thesis for the sake of brevity. Instead, the sample exposed for 4000 h was used for examination with HR-SEM (High Resolution SEM), both in cross-section and surface view. For examination in surface view, also in this case a portion of the sample was cleaned with a soft solution of hydrogen peroxide, acetic acid and ethanol (ratio 1:1:1 diluted up to 10% *vol.*).

Cross-section SEM images of virgin coated sample with PLD are reported in Figure 8.19. The coating is uniform and thick about 3 μm above EUROFER substrate. Some detachments were detected during the examination. These detachments can be related to the mechanical preparation of the sample for the SEM examination (cutting and polishing). For 1000 h of exposure in flowing LiPb, the cross-section SEM images

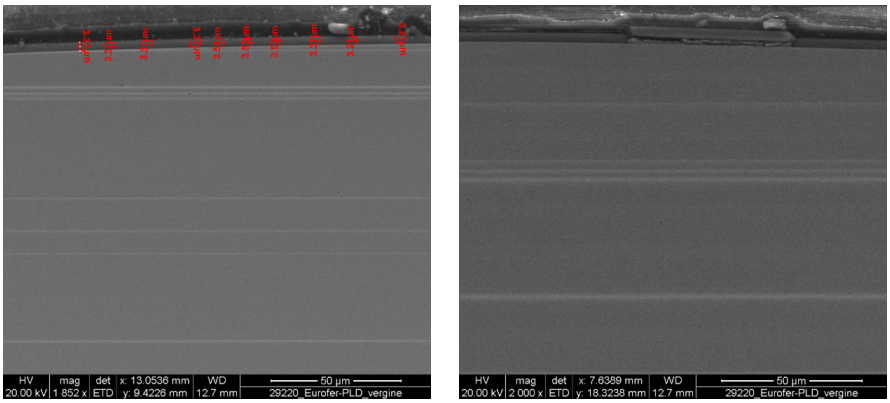

(a) **(b)**

Figure 8.19. Cross-section SEM images of virgin EUROFER sample coated with PLD alumina 3 μm

show that the coating remained adherent to the surface of EUROFER protecting the substrate from corrosion. The thickness of the coating was globally conserved. Only some detachments were observed, but they are probably related to the mechanical

preparation of the sample (cutting, polishing) for SEM examination. Indeed, no sign of corrosion of the EUROFER was detected underneath these detachments. By performing compositional analysis with EDX, it is possible to observe that no chemical variation of the coating has occurred after the exposure. Point analysis was performed on the length of the thickness to investigate possible superficial formation of lithium aluminide compounds (e.g. $LiAlO_2$), but no significant variation in the Al/O ratio was detected along the thickness. Some traces of Cr and Fe were found on the surface of the coating, as already observed for Nb, V and P22. Also in this case, the presence of these elements is likely due to an initial contamination of the LiPb inside IELLLO loop, and related to the corrosion of the piping of the loop.

Line-scan of Al, O, Fe, Cr elements (8.20) shows no significant chemical variation of the coating and no significant chemical interaction with LiPb alloy and dissolved impurities (Fe and Cr).

Longitudinal SEM images of the portion of cleaned sample are reported in Figure 8.21. The surface of the coating does not show significant point defects and no corrosion pits on EUROFER substrate below are visible. Again, traces of LiPb were found on the surface of the coating, mainly enriched with Cr element, which were not fully removed from the surface as a consequence of the soft chemical cleaning.

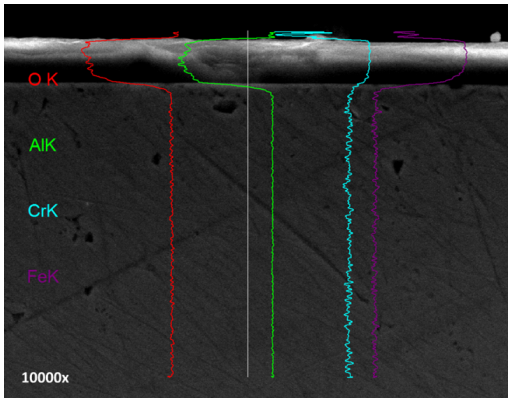

Figure 8.20. Line-scan of O, Al, Cr, Fe elements along the thickness of the coating after 1000h

Cross-section SEM images after 2000 h are reported in Figure 8.22 for low and high magnification. Again, the coating remained globally well adherent to the substrate and protected the EUROFER below. The thickness of the coating was conserved. Also the line-scan by EDX (not reported here) shows no appreciable chemical variation in the coating and chemical interaction with LiPb alloy and dissolved impurities.

Damaged coating was observed only in a portion of the sample. However, the substrate below was not corroded, so this damaging could be related to a starting defect in this area. Indeed, the surface of the EUROFER close to the defect seems highly inhomogeneous and rough and probably the coating was not deposited correctly in this point.

Longitudinal SEM analyses after cleaning confirm that the surface of the coating does not show significant defects and no corrosion pits on EUROFER substrate. Traces of LiPb with Fe and Cr contamination were found on the surface of the

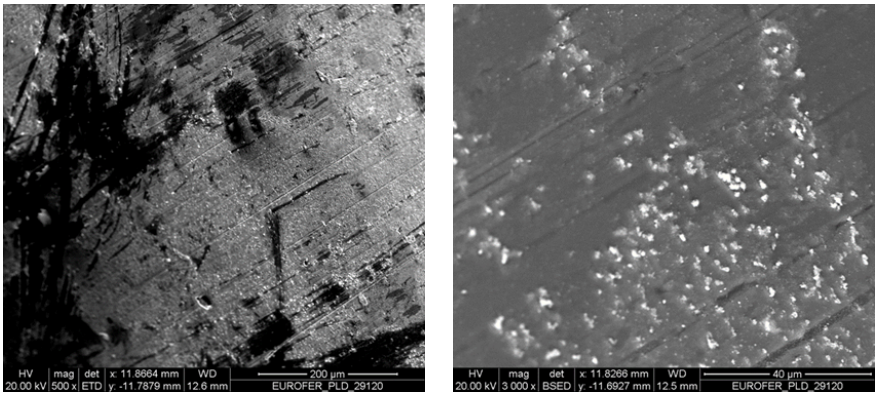

(a) **(b)**

Figure 8.21. Longitudinal SEM images of PLD coating sample after exposure for 1000 h

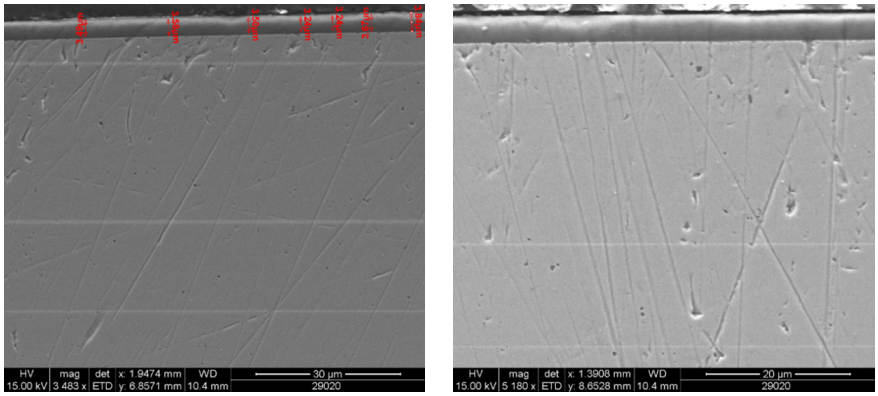

(a) **(b)**

Figure 8.22. Cross-section SEM images at different magnification of PLD coating after 2000 h

coating. Interestingly, also traces of V contamination was found, likely coming from the release of corrosion products from V samples in the test section.

Cross-section and surface SEM images of the PLD coating exposed for 4000 h are reported in Figure 8.23 at low and high magnification and compared to cross-sections of virgin sample. The coating remained adherent to the EUROFER surface protecting the substrate from corrosion by LiPb, and the thickness of the coating was conserved (around 3 μm). After cleaning with chemical solution, the surface exhibits basically flat and homogeneous appearance. Only very few small isolated defects were detected above the entire surface of the sample (see Figure 8.24), in accordance with previous analysis for 1000 and 2000 h exposure.

Observing at high magnification the surface of the coatings after the exposure, it is possible to note the grainy appearance of the surface after the exposure (see Figure 8.25), in contrast with the smooth, flat and bright surface of the as-deposited coatings. The grainy appearance is likely related to some kind of interaction and maybe due to the potential formation of LiAl-oxide compounds which cannot be identified with EDX analysis.

In summary, PLD alumina deposited on EUROFER conserves the thickness after the exposure in LiPb (3 μm) and remains adherent to the substrate. The quality of the coating is high and very few defects were detected along the various exposures. No significant/appreciable chemical variation was found by EDX but grainy appearance was detected on the surface, likely due to LiAl-oxide formation. The formation of these compounds is under investigation with other techniques (SIMS, XPS, atomic probe).

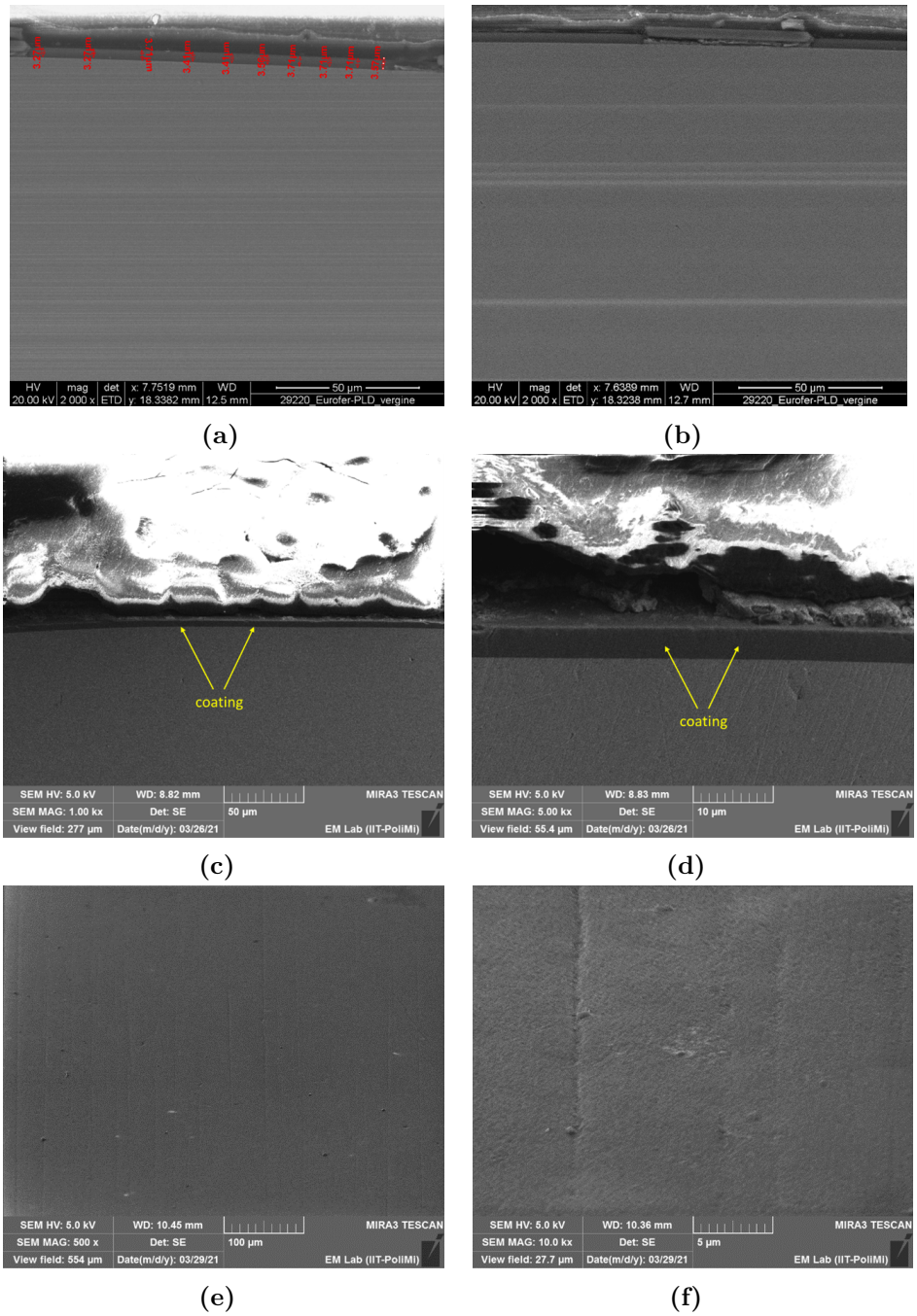

Figure 8.23. Surface HR-SEM images of the surface of the PLD alumina coatings (3 μm) as-deposited (a and b) and after 4000 h in flowing LiPb (c to f)

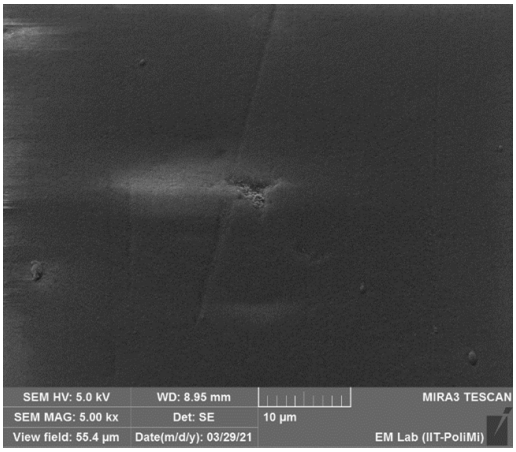

Figure 8.24. Isolated defect in PLD alumina coating after 4000 h

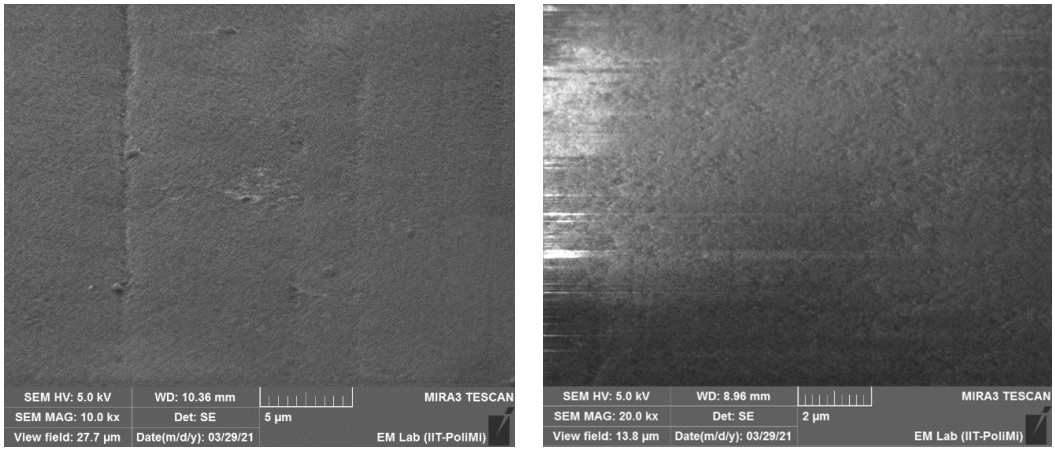

(a) **(b)**

Figure 8.25. Grainy appearance of the surface of the PLD alumina coating after 4000 h in LiPb

8.4.3 ALD

Alumina coating by ALD was deposited on EUROFER cylindrical samples with a thickness of 300 nm. The sample was then annealed for 75 h at 550 °C in air. The examination of the ALD coating with HR-SEM is reported in this section for virgin and 1000, 2000 and 3000 h exposed samples, both in cross-section and surface view. For the examination in surface view, a portion of the sample was cleaned with a soft solution of hydrogen peroxide, acetic acid and ethanol (ratio 1:1:1 diluted up to 10% *vol.*).

Surface view of the virgin ALD alumina coating is reported in Figure 8.26. The appearance of the coating is flat when perfectly deposited and the lines of the preparation of the EUROFER substrate are also visible. However, after annealing of the sample at 550 °C for 72 h in air, several deposition defects in the form of holes/pits are detected and highlighted by the circular oxidation of the substrate underneath.

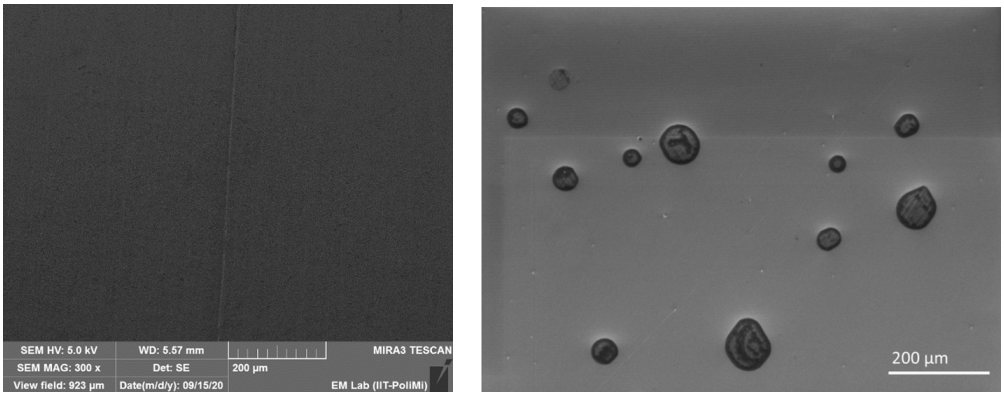

(a) **(b)**

Figure 8.26. Surface HR-SEM images of an as-deposited ALD alumina coating (a) and after annealing in hot air at 550 °C for 72 h (b)

By observing HR-SEM images on surface view for the sample exposed to 1000 h, it is possible to observe that the coating is mostly present on the EUROFER substrate (see Figure 8.27), but there are pit defects and detachments in several areas of the sample. When the coating is adherent to the surface, it conserves its thickness after the exposure and the substrate is protected from corrosion. Pit defects at 1000 h have often chemical composition similar to that of EUROFER, or also with Cr surface enrichment (due to Cr accumulation on the surface).

Cross-section SEM images after 1000 h are reported in Figure 8.28a for high magnification. The surface of the sample is homogeneous and with low degree of rugosity, meaning that no corrosion occurred on the EUROFER substrate below. Observing the EDX analysis in Table 8.5, the elemental composition in proximity of the interface was the same of the bulk material, confirming that no chemical modification has occurred in the EUROFER below as a consequence of LiPb corrosion.

Some defects, located within an area of about 2 mm, were detected on the EUROFER substrate sample (Figure 8.28b). These defects consist in sort of "bubbles" and they are likely related to polishing defects on the starting EUROFER cylindrical

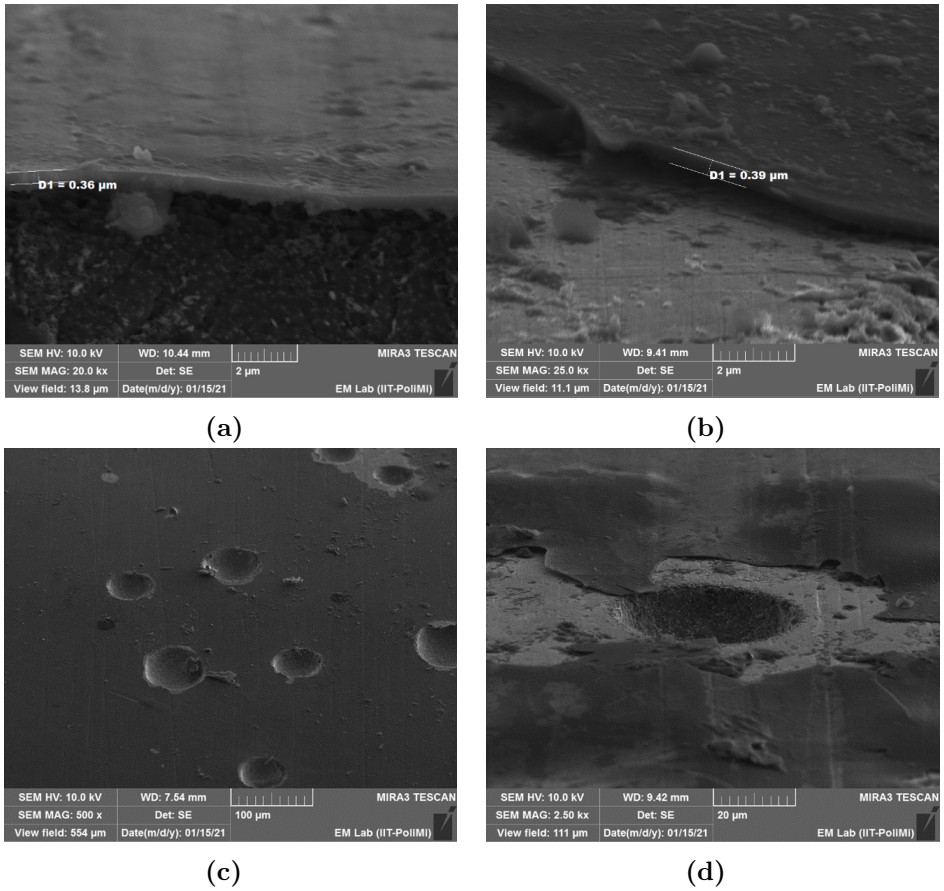

Figure 8.27. Surface HR-SEM images of the surface of the ALD coating after 1000 h in flowing LiPb

samples (before the deposition of the coating). Although it is not possible to investigate the effective presence and quality of the coating in this "bubbled areas", here the EUROFER does not show the typical signs of corrosion by LiPb (e.g. variation of the chemical composition and Cr leaching, cf. Table 8.6) and it is reasonable to argue that even in these bad areas the coating exists and protect in some way the EUROFER underneath.

Table 8.5. Elemental analysis by EDX of ALD coating after 1000h

Element		SiK	WM	CrK	MnK	FeK
Area 1 of Figure 8.28a	Wt.%	0.18	1.61	8.46	1.12	88.63
	At.%	0.35	0.49	9.12	1.14	88.90
Area 2 of Figure 8.28a	Wt.%	0.22	1.61	9.21	0.65	88.31
	At.%	0.45	0.49	9.91	0.67	88.49

HR-SEM images (surface and cross view) on the sample exposed to 2000 h confirms the behaviour of the 1000 h exposed sample. The coating is mostly presents on the EUROFER substrate (see Figure 8.29), but with pit defects and detachments. Surface examination was performed also with low resolution SEM (FEI, Inspect

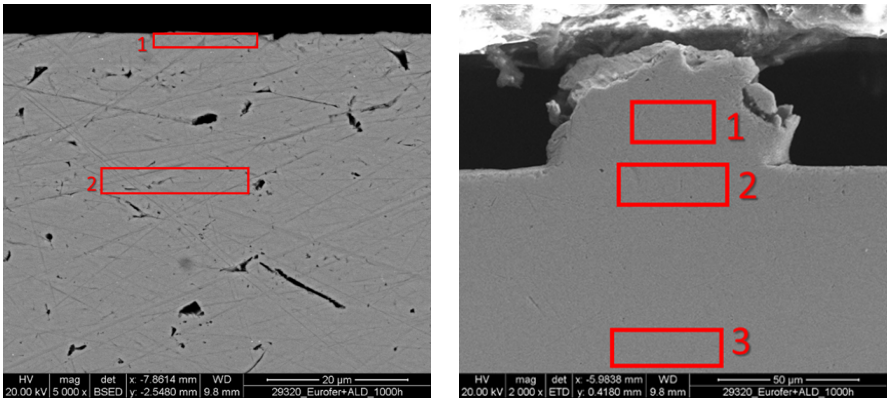

(a) **(b)**

Figure 8.28. Cross-section SEM images of ALD coating after 1000h in a general zone (a) and in a zone of defects (b)

Table 8.6. Elemental analysis by EDX of ALD coating after 1000h in a zone of defects

Element		WM	CrK	MnK	FeK
Area 1 of Figure 8.28b	Wt.%	2.5	8.8	0.8	87.9
	At.%	0.8	9.6	0.8	88.8
Area 2 of Figure 8.28b	Wt.%	2.4	8.9	0.8	87.9
	At.%	0.7	9.7	0.8	88.8
Area 3 of Figure 8.28b	Wt.%	2.5	9.2	0.8	87.6
	At.%	0.8	0.0	0.8	88.5

Table 8.7. Elemental analysis by EDX of ALD coating after 1000h in a zone of defects

Element		OM	AlK	PbM	CrK	FeK
Area 1 of Figure 8.31	Wt.%	19.3	22.7	1.3	6.6	50.1
	At.%	39.2	27.3	0.2	4.1	29.2
Area 2 of Figure 8.31	Wt.%	15.6	16.7	2.3	31.7	33.7
	At.%	34.6	21.9	0.4	21.6	21.5
Area 3 of Figure 8.31	Wt.%	16.4	16.9	7.0	28.2	31.5
	At.%	36.7	22.5	1.2	19.4	20.2
Area 4 of Figure 8.31	Wt.%	20.4	22.1	1.2	6.6	49.7
	At.%	41.0	26.2	0.2	4.1	28.5

S, W filament). In the pit defects, the coating is often collapsed or also partially suspended (Figure 8.30). Crystal deposits were found in significant amounts in the areas where the coating is flat and adherent. The deposits are strongly enriched with Cr (up to 30% *wt.*), as shown in point EDX analysis in Figure 8.31 and Table 8.7. Where the surface is free from the deposits, Al and O are detected by EDX, together with Fe and Cr with composition typical of the substrate underneath.

A high content of Cr was found also inside the pits cavity and may depend, as similar to P22 steel, on Cr contamination of the LiPb and re-deposition above the steel surface (enrichment detected up to 40% *wt.*).

After 3000 h of exposure, the appearance of the coated samples is the same as after 1000 and 2000 h of exposure (see Figure 8.32): where the coating is flat and

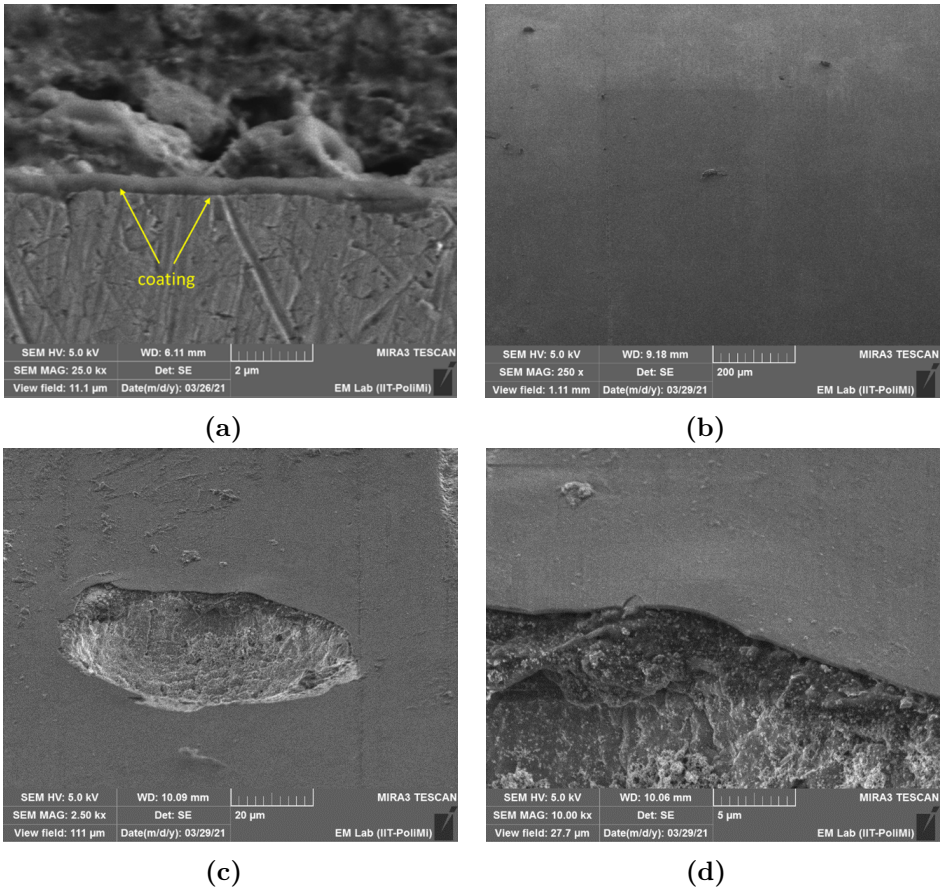

Figure 8.29. Cross and surface HR-SEM images of the surface of the ALD coating after 2000 h

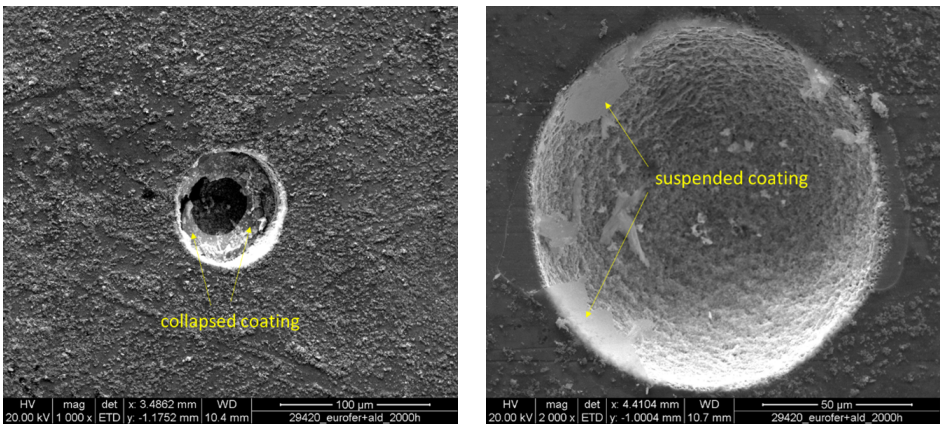

Figure 8.30. SE-SEM images of the surface of ALD coating after 2000h in flowing LiPb, showing hole defects with collapsed (a) and suspended coating (b)

adherent to the surface, the EUROFER below is protected by LiPb corrosion attack. By surface examination after cleaning, it is possible to observe, also for ALD coating,

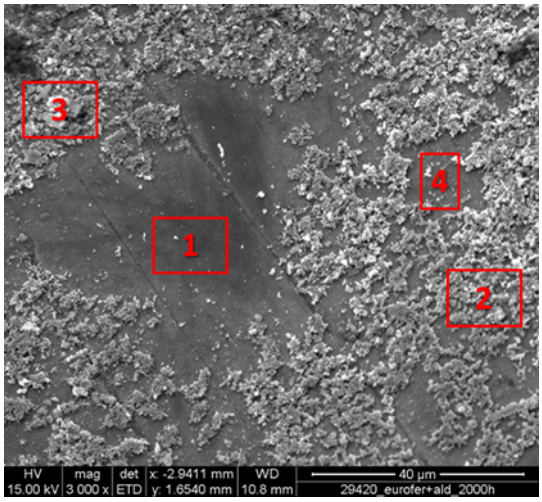

Figure 8.31. Surface appearance of the ALD coating after 2000h in flowing LiPb and after chemical cleaning

the grainy appearance of the surface, in contrast with the flat and smooth surface of the coating before the exposure (cf. 8.26). Pit defects are detected and spread above the surface. Moreover, bubbles protrusion are visible in the EUROFER substrate. In these areas, the coating is not present or detected. Considering that some pit defects did not show sign of corrosion attack inside, these bubbles/protrusions are likely to be spalled off from the substrate under the effect of flowing LiPb, creating the pit hole defects spread above the surface.

In summary, ALD alumina deposited on EUROFER presents a bad starting quality compared to PLD coating. When the coating is still adherent to the surface, the substrate below is protected by LiPb attack. From surface analyses several pit defects and detachments were detected, likely related to a bad starting finishing state of the substrate below. Grainy appearance was found also for ALD samples, likely related to the formation of LiAl-oxides. The formation of these compounds is under investigation with other techniques (XPS, SIMS, atom probe) at the time of writing.

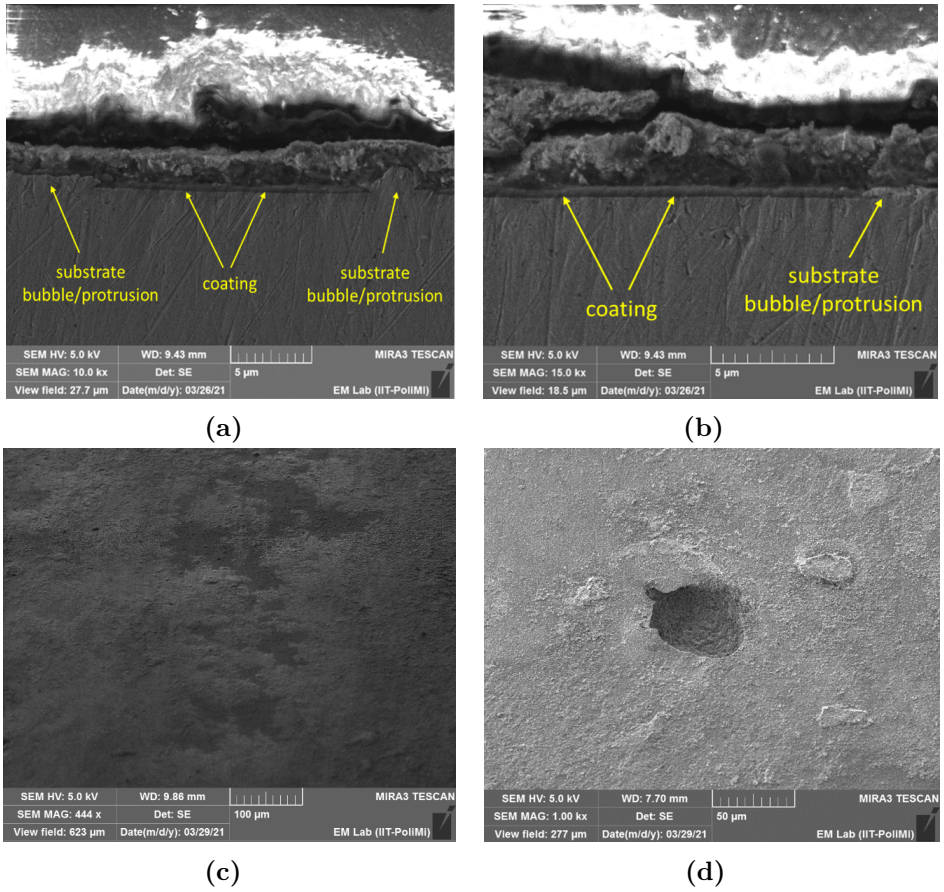

Figure 8.32. Cross and surface HR-SEM images of the surface of the ALD coating after 3000 h

8.5 Main outcomes on the materials compatibility with LiPb

This section summarizes the observed behavior of each material, trying to find similarities between niobium and vanadium and between the coatings made with the two techniques, PLD and ALD.

- Niobium samples did not show relevant weight loss after 4000 h, but a slight increase of weight was detected, related to the formation of a thin layer made of iron and nickel. The latter reacted with niobium forming $NbNi_3$ on the surface. Also in the case of vanadium, a compound of nickel was found on the surface of the samples, which was indeed smoother than before the exposure. The formation of these compounds should be better investigated, as their potential effect on tritium permeation is currently unknown. However, nickel is not expected to be present in the LiPb flowing in the WCLL BB, as nickel-rich materials will be carefully avoided by the design team.

- Portions of P22 samples were detached from the bulk and LiPb penetrated onto the interface, where also a strong chromium enrichment was found. This is likely related to re-deposition phenomena of LiPb contaminants on the surface. For this reason, tests in controlled environment are suggested to deepen the investigation of the corrosion behavior of this material.

- EUROFER samples coated by PLD conserved the thickness after the exposure in PbLi (3 µm) and remained adherent to the substrate, while the chemical composition detected by EDX remained the same throughout the various exposures. Instead, the grainy appearance of the surface induced to think about the formation of LiAl-oxides, which has been later demonstrated by further analyses performed at IIT and CIEMAT. Also the coatings deposited by ALD presented this grainy appearance of the surface, but in addition they had a bad quality compared to the ones made by PLD. Where the coating was still adherent to the surface, the substrate below was protected by the corrosive attack, but several pit defects and detachments were detected on the surface, likely related to a bad starting finishing state of the substrate.

Part IV

Final remarks

Chapter 9

Conclusions and future perspectives

The objective of this PhD thesis was twofold with the two parts linked by tritium transport, which has been the guiding light of the entire research.

On the one hand, in a tokamak reactor, tritium is the fuel of the reaction and it has to be extracted from LiPb where it is generated from the lithium transmutation. Therefore, the characterization of the main tritium extraction technologies, the Gas-Liquid Contactor and the Permeator Against Vacuum, one of the objectives of this thesis, is becoming a crucial point in the R&D on the WCLL BB. Part II starts with a chapter aimed at briefly describing TRIEX-II facility with the aim of helping the comprehension of the experimental activities depicted in Chapter 5 and Chapter 6. Moreover, the refurbishment and the commissioning of the facility constitute a big effort and a good achievement of this research work and, as such, they are worth being described in this thesis.

On the other hand, tritium has to be confined in LiPb, with the obvious exception of the path through components devoted to tritium extraction, to avoid contamination of the water or of the tokamak building. This issue is being faced by developing anti-permeation coatings. Although these two technological fields are conflicting in their aim, they share many aspects, starting with the theoretical background, that makes possible, or even advantageous, to work on both.

While the former issue is specific to the fusion field, the latter is a challenge also for the so-called fourth generation fission reactors and, especially, for the Lead-cooled Fast Reactors, such as ALFRED. Moreover, coatings are expected not only to prevent tritium permeation, but also to minimize corrosion of the structural materials. Among many possible coating materials, alumina has been selected as the most promising one in the past decades, but open questions are still waiting to be answered. This thesis tried to give a contribution to address two of these: the characterization of the Permeation Reduction Factor in relevant operative conditions and with water on the secondary side of the coated pipe, thanks to the use of APRIL facility, and the characterization of the alumina compatibility with LiPb flowing at relevant speed and temperature, in IELLLO facility. These activities are described in details in Chapter 7 and in Chapter 8, respectively.

Chapter 8 also includes the description of the corrosion resistance of niobium,

vanadium and P22 steel (ASTM A335 Gr. P22), which were exposed to LiPb in the same experimental campaign devoted to test the compatibility of the coatings. In particular, P22 steel has been often considered as the main candidate material for the pipework of the WCLL TER, but its resistance to the corrosive attack of LiPb has never been tested before the campaign in IELLLO. Instead, niobium and vanadium are the two main materials which are under consideration as membranes for the Permeator Against Vacuum. Their behavior in LiPb has already been studied in the past (e.g. [94] for vanadium and [92] for niobium), but mainly in static LiPb. Starting an investigation on the impact of dynamic conditions seemed to be a necessary step of this thesis to complement the characterization of the Permeator Against Vacuum technology.

A summary of the main outcomes of each activity is described in the following, divided into "Tritium extraction technologies" and "Coatings".

9.1 Tritium extraction technologies

The main line of research was devoted to the Permeator Against Vacuum: a conceptual design of a mock-up had already been performed at the start of the PhD, but several steps were necessary to achieve an effective engineering design before the start of the manufacturing. The manufacturing itself was a challenge on its own, as there were several pioneering applications on materials and instrumentation. Likewise, the integration of the test section in TRIEX-II facility was performed, followed by a set of commissioning tests and calibration procedures. Finally, the mock-up performances were characterized at different hydrogen partial pressures, 1.2 kg/s and 350 or 450 °C.

As far as the manufacturing is concerned, the most innovative result of this thesis is the solution adopted to join the niobium pipe with the F22 plate. The idea, developed together with experts from RINA CSM, was to use a vacuum brazing based on a nickel-based brazing alloy (capable of withstanding up to 1100 °C). The vacuum brazing avoids the oxidation of niobium, while, to prevent nickel from solubilizing in LiPb, the brazings were carried out in such a way that avoids the contact between the filler material and the LiPb. The brazing was performed on almost the entire depth of the plate in order to create a strong joint between the two materials. Each brazing was later inspected with not destructive testing (radiography) and checked for potential leakages with helium.

In the meanwhile, a selection of the most suitable instruments and pieces of equipment was performed, in parallel with the refurbishment of TRIEX-II facility to host the PAV mock-up. In particular, four heating lamps were selected as heating system for the niobium tubes, instead of using heating cables that would have limited the permeation surface. Indeed, the lamps are made of quartz, a material that is not permeable to hydrogen, so that their presence did not affect the measurement of the permeated flux. Vacuum connectors were selected through a careful market survey to ensure the best vacuum sealing, while being able to install more than 50 thermocouples on the tubes, to power the lamps and to install a quartz porthole, which was useful to visually monitor the conditions of the tubes during operation.

The manufacturing of the first PAV mock-up for LiPb to ever be completed,

and its successful commissioning, constitutes an important milestone towards the development of the WCLL TER, also as the possibility to manufacture a PAV was questioned at the end of the EUROfusion FP8. The activities on engineering design have been published in [49] and those on and manufacturing have been presented at the 32nd Symposium on Fusion Technology (SOFT), together with the first experimental results, and are currently under review.

After the installation of the PAV mock-up in TRIEX-II, a first experimental campaign was carried out with the aim of characterizing the mock-up performances. The experimental campaign demonstrated that the manufaturing techniques can withstand the harsh conditions of a LiPb flow, but, most importantly, that the PAV technology can be used to extract hydrogen isotopes from LiPb. The tests highlighted that the higher the temperature the higher the permeated flux, with approximately one order of magnitude between the tests at 350 °C (in the order of 10^{-9} mol/s) and those at 450 °C (in the order of 10^{-8} mol/s). These results are also confirmed by the pressurization tests, which indicate similar orders of magnitude for the permeated flux, and by the signals of the Hydrogen Pemeation Sensors, which show a partial pressure drop across the mock-up that is repeatable within each test and that increases with the inlet partial pressure. The right operation of the Hydrogen Pemeation Sensors in TRIEX-II is an important achievement of this thesis, as the previous configurations were subjected to leakages.

These results are the first experimental assessment of the performances of the PAV technology and mark a milestone for the development of this concept. The measured permeated fluxes, and the associated drops in the hydrogen partial pressure in LiPb, are deemed to be encouraging, also considering that no treatments were performed on the niobium before its installation in TRIEX-II (e.g. no cleaning of the external surface to remove oxides, which are known to reduce tritium permeation [80]). However, further activities will be needed to improve the knowledge on this technology and the assessment on its performances. First, testing tubes with different lengths and inner diameters would be interesting to start understanding the impact of hydrogen transport in LiPb on the extraction, thus moving towards a bigger awareness of the scaling laws. Furthermore, the possibility to increase the permeability by depositing a palladium-silver coating on the niobium surface has been known since several years [121] and recently tested at ENEA Casaccia on small niobium disks with gaseous hydrogen on one side and vacuum on the other [122]. It would be very important to test this technique in a LiPb facility to assess if it has the same impact also on a more complex system, even though, at the time of writing, no activities are planned on this aspect of the research. Currently, the already-scheduled activity on PAV is related with the manufacturing of a vanadium mock-up at CIEMAT to be later tested in CLIPPER facility. However, thanks to the results obtained within this thesis on the PAV mock-up new activities will be proposed to be funded within EUROfusion FP9.

In parallel to these activities on the PAV mock-up, niobium compatibility with LiPb was investigated with IELLLO facility by exposing 12 cylindrical samples in LiPb flowing at 0.5 m/s at 500 °C. This step complements the performance assessment by advancing the knowledge on niobium compatibility. The experimental campaign in IELLLO also studied the corrosion resistance of vanadium, the other candidate material for membranes. Niobium samples do not show relevant weight

loss after 4000 h. A slight increase of weight was detected, very likely related to the formation of a thin layer made of Fe and Ni contaminants, already present in the LiPb. After 4000h of exposure, the interaction with Ni is remarkable and $NbNi_3$ was detected on the surface. This point needs more clarification, as the possible interaction of niobium with contaminants may affect its performances in terms of tritium transport. However, nickel is not expected to be present in large amounts in the WCLL BB and TER, as LiPb will be constantly purified in the Cold Traps and the adopted structural materials will not contain much nickel in the first place.

Regarding vanadium compatibility with LiPb, exposed vanadium samples exhibited a smoother surface after the exposure and the original surface finishing was no longer identified at the end of the 4000 h. In addition, also in this case, corrosion was identified due to an interaction with Fe and Ni contaminants. The formation of this compound needs to be deeper investigated but XRD analysis indicates formation of Ni-V intermetallics. As in the case of niobium, the interaction with nickel may affect the properties of the material, but no data are available on this issue.

An interesting future line of research would be precisely on this topic: preparing samples of niobium and/or vanadium with shapes suitable for permeation experiments (e.g. pipes or disks), exposing them to LiPb enriched with corrosion products from fusion relevant steels and finally comparing their performances in terms of tritium transport with those of the virgin materials. However, due to the fact that similar activities are not scheduled at the moment within EUROfusion, these proposals will be presented in the next years.

The main results on the P22 behavior in LiPb are also described in this section, as this material is currently considered for the WCLL TER and its components, including the Tritium Extraction Unit. The exposed P22 samples underwent detachments of portions/fragments and LiPb penetration at the interface. Strong Cr enrichment was found in the near interface, likely related to re-deposition phenomena of contaminants on the surface. However, tests in a controlled environment should be performed in the future, to investigate exhaustively the corrosion behavior of this material.

The results on the compatibility of niobium, vanadium and P22 in LiPb have been published in [123].

Finally, the other activity on tritium extraction systems was related to GLC technology. An experimental campaign was carried out but two issues prevented the success of the experiments. First, a P22 pipe failed, causing a stop of several months due to the necessity of removing the thermal insulation, cleaning the pipes from LiPb and replacing the failed pipe. Then, after that the experimental campaign showed an average low efficiency (about 6% in 32 hours of extraction), it was discovered that the packings that constitute the core of the GLC mock-up were corroded and completely lost their integrity. The samples of Mellapak foil and net, observed both to the naked eye and under SEM analysis, revealed the presence of a deposit on the original AISI 316 steel, while EDX analyses showed a depletion of nickel and chromium which gave rise to a porous microstructure and to a reduction of the thickness from the 89 to 40 microns, on average. This behavior has motivated an on-going market survey to find packings of different materials with a better compatibility with LiPb (e.g. ferritic steels). Even though the experimental campaign did not provide relevant data on the GLC performances, the lessons learned on P22 and packing behavior are

considered useful for the future design of experimental facilities and also of real-size components and, in the context of the thesis, nicely fit in the compatibility section, together with the data from the corrosion campaign.

These lessons learned already demonstrated their usefulness in the preparation of the 2022 experimental campaign, which is about to start at the time of writing. This campaign has two main objectives: the first one is to check the repeatability of the tests performed on the GLC mock-up in 2019 in terms of efficiencies and extracted hydrogen fluxes [124]; the second one is to further investigate the impact on the extraction efficiency of the addition to the stripping gas of some tenths of percentage point of a different hydrogen isotope with respect to that solubilised in LiPb (e.g. if deuterium is solubilised in LiPb to simulate tritium, some protium can be added to the helium stripping flow). Theoretically, this addition should increase the extraction efficiency by taking advantage of the isotopic exchange. This effect has been already noted in the 2019 campaign, but it requires further experimentation to be completely understood and for its impact to be quantitatively assessed.

Besides this incoming experimental campaign, there are many possible future activities on GLC. For instance, more experiments could be needed to start delving into the scaling factors or the impact of packings of different geometry or size. Then, the experimental data can be used to evaluate mass transport coefficients in the different scenarios, but also to calibrate or partially validate the modelling tools that are under development at Politecnico di Torino and CIEMAT. Finally, activities are on-going and will proceed towards the design of a GLC for the WCLL TER aiming at allowing a proper comparison with the PAV and with the LVC in view of the selection process of the reference extraction technology for DEMO.

9.2 Coatings

The research on coatings was split into two activities: the corrosion resistance of EUROFER samples coated with alumina with two different techniques, the PLD (Pulsed Laser Deposition) and the ALD (Atomic Layer Deposition), were tested in flowing LiPb in IELLLO facility and the Permeation Reduction Factor of a PLD-coated AISI 316 tube was measured in APRIL facility with water.

Starting with the second point, the activities were firstly focused on the design of APRIL facility, a new device which will allow to study the hydrogen isotope permeation in a more relevant environment. Indeed, the capabilities of the facility already allow to investigate the permeation from gas phase to water at operative conditions which are relevant for the WCLL BB or for the lead-cooled ALFRED reactor. Future upgrades could also add the possibility to perform tests in an even more relevant situation by adding LiPb or pure lead on the main chamber of the facility, thus exactly reproducing the conditions under which the permeation will occur in the reactors. After the design was completed, the following steps were the manufacturing, performed by S.R.S., the choice of the instrumentation and the conceptualization of the experimental procedures, which were parts of this work. Finally, the first experiment at ALFRED operative conditions (water at 480 °C, deuterium concentration in the gas phase of 0.5%) was carried out. This experiment was devoted to study the Permeation Reduction Factor of a PLD-coated AISI 316

tube, by comparing the amount of deuterium in the water contained in the tube without coating (bare AISI 316) with that in the coated tube (3 µm of coating). The experiment lasted about 81 hours, following some considerations based on the results of pre-test simulations with COMSOL. The water samples extracted from the facility were analyzed by IR spectrometry and, after subtracting the natural deuterium abundance in water, a deuterium concentration of 379 ppm was found in the water contained in the bare pipe, while 28 ppm were found in the coated pipe. The calculated PRF is of about 13.5.

The design and the results of APRIL have been presented at the 13th International Conference on Tritium Science and Technology and contributed to [125].

More experiments will be performed in the next months in the same conditions to verify the repeatability of this result. Moreover, APRIL facility will be involved in a new activity within the TITANS project, which was officially launched in September 2022. This activity will be performed with water at WCLL Primary Heat Transfer System operative conditions and will be devoted to characterize hydrogen isotopes permeation through bare EUROFER. The data obtained in TRANSAT and TITANS projects will also be used to validate the simulations of a numerical tool developed with COMSOL Multiphysics.

Regarding the first point mentioned at the beginning of this section, the behavior of the coatings made by ALD and PLD was quite different. Indeed, PLD alumina deposited on EUROFER conserved the thickness after the exposure in LiPb (3 µm) and remained adherent to the substrate. The quality of the coating is high and very few defects were detected along the various exposures. No significant/appreciable chemical variation was found by EDX, but a grainy appearance was observed on the surface, likely due to LiAl-oxide formation.

Instead, the ALD alumina coatings were deposited on EUROFER samples at IIT with a new scaled-up device and presented a worse quality compared to the ALD coatings manufactured with the old system [126] and also compared to PLD coating. A further optimization of the manufacturing procedure will be likely required in order to achieve higher quality coating standard. Where the coating was still adherent to the surface, the substrate below was protected by LiPb attack, but several pit defects and detachments were detected from surface analyses, likely related to a bad starting finishing state of the substrate below. The same grainy appearance observed on the PLD-coated samples was found also for ALD-coated samples and also in this case this is likely related to the formation of LiAl-oxides.

The grainy appearance of the samples exposed in IELLLO, together with a similar behavior observed on samples exposed in static LiPb outside of the context of this thesis, constituted the first step towards the discovery of an issue that is currently under investigation within EUROfusion. Analyses performed at CIEMAT and at IIT by SIMS (Secondary-Ion Mass Spectrometry), Atomic probe and XPS (X-ray Photoelectron Spectroscopy) revealed that lithium tends to form compounds with aluminum and to diffuse though the coating. The extent of this phenomenon and its consequences on the coating durability are still under discussion, but the scheduled activities on PLD and ALD coatings have been partially stopped waiting for a better understanding of the phenomenon to be reached. For those who are interested, the analyses performed at CIEMAT are partially described in [118], while the IIT analyses are still unpublished.

The future activities on coatings are obviously connected with the outcomes of the current discussion within EUROfusion. However, in the author's opinion, it could be useful to check if this lithium diffusion has an impact on how the coatings reduce the tritium permeation, as the tests in IELLLO already demonstrated that the coatings retain their anti-corrosion properties (at least the ones made by PLD). To this end, a new corrosion campaign could provide samples of adequate shape (e.g. disks or tubes) to perform permeation tests whose results could contribute to a better assessment of the impact of lithium diffusion on the coatings performances and, perhaps, to form a consensus on the future of alumina coatings.

Bibliography

[1] U. D. of Energy, 'Doe handbook: Tritium handling and safe storage', 1999.

[2] U. D. of Energy, '10 cfr part 835 - occupational radiation protection', 2015.

[3] F4E, *Fusion for energy website*.

[4] GIF, *Gen iv international forum website*.

[5] G. Caruso, *La fusione termonucleare controllata*, 1998.

[6] B. Bornschein, C. Day, D. Demange, and T. Pinna, 'Tritium management and safety issues in iter and demo breeding blankets', vol. 88, 2013, pp. 466–471. DOI: 10.1016/j.fusengdes.2013.03.032.

[7] T. Giegerich, K. Battes, J. C. Schwenzer, and C. Day, 'Development of a viable route for lithium-6 supply of demo and future fusion power plants', *Fusion Engineering and Design*, vol. 149, Dec. 2019, ISSN: 09203796. DOI: 10.1016/j.fusengdes.2019.111339.

[8] A. D. Nevo, P. Arena, G. Caruso, *et al.*, 'Recent progress in developing a feasible and integrated conceptual design of the wcll bb in eurofusion project', *Fusion Engineering and Design*, vol. 146, pp. 1805–1809, Sep. 2019, ISSN: 09203796. DOI: 10.1016/j.fusengdes.2019.03.040.

[9] P. Hubberstey, T. Sample, and M. G. Barker, 'Is pb-17li really the eutectic alloy? a redetermination of the lead-rich section of the pb-li phase diagram ($0.0 < xLi(at\%) < 22.1$)', *Journal of Nuclear Materials*, vol. 191-194, pp. 283–287, 1992, ISSN: 00223115. DOI: 10.1016/S0022-3115(09)80051-2.

[10] D. Martelli, A. Venturini, and M. Utili, 'Literature review of lead-lithium thermophysical properties', *Fusion Engineering and Design*, vol. 138, pp. 183–195, Jan. 2019, ISSN: 09203796. DOI: 10.1016/j.fusengdes.2018.11.028.

[11] M. Kordac and L. Kosek, 'Helium bubble formation in pb-16li within the breeding blanket', *Fusion Engineering and Design*, vol. 124, pp. 700–704, 2017.

[12] A. Deoghar and et al., 'Design, development and testing of prototype cold trap for pb-16li purification', *Fusion Engineering and Design*, vol. 137, pp. 289–294, 2018.

[13] M. Utili, 'R&d tritium extraction from lipb', $TER.WCLL-JUS-2-CD1$, $EFDA\_2MN888$, 2019.

[14] EUROfusion, *Eurofusion consortium website*.

[15] N. Alpy, A. Terlain, and V. Lorentz, 'Hydrogen extraction from pb-17li: Results with a 800 mm high packed column', *Fusion Engineering and Design*, vol. 49, pp. 775–780, 2000. [Online]. Available: www.elsevier.com/locate/fusengdes.

[16] D. Demange, R. Antunes, O. Borisevich, *et al.*, 'Tritium extraction technologies and demo requirements', *Fusion Engineering and Design*, vol. 109-111, pp. 912–916, Nov. 2016, ISSN: 09203796. DOI: 10.1016/j.fusengdes.2016.01.053.

[17] F. Okino, P. Calderoni, R. Kasada, and S. Konishi, 'Feasibility analysis of vacuum sieve tray for tritium extraction in the hcll test blanket system', *Fusion Engineering and Design*, vol. 109-111, pp. 1748–1753, Part B 2016, ISSN: 09203796. DOI: 10.1016/j.fusengdes.2015.10.004.

[18] A. Tahara and Y. Hayashi, 'Measurements of permeation of hydrogen isotopes through α-iron by pressure modulation and ion bombarding', 1985, pp. 869–875.

[19] M. Malo, B. Garcinuño, and D. Rapisarda, 'Experimental refutation of the deuterium permeability in vanadium, niobium and tantalum', *Fusion Engineering and Design*, vol. 146, pp. 224–227, Sep. 2019, ISSN: 09203796. DOI: 10.1016/j.fusengdes.2018.12.025.

[20] F. Cismondi, G. A. Spagnuolo, L. V. Boccaccini, *et al.*, 'Progress of the conceptual design of the european demo breeding blanket, tritium extraction and coolant purification systems', *Fusion Engineering and Design*, vol. 157, Aug. 2020, ISSN: 09203796. DOI: 10.1016/j.fusengdes.2020.111640.

[21] M. Utili, S. Bassini, S. Cataldo, *et al.*, 'Development of anti-permeation and corrosion barrier coatings for the wcll breeding blanket of the european demo', *Fusion Engineering and Design*, vol. 170, Sep. 2021.

[22] GIF, 'Technology roadmap update for generation iv nuclear energy systems', 2014.

[23] I. Pioro, *Handbook of Generation IV Nuclear Reactors*, Second edition. Woodhead Publishing, 2022.

[24] A. Waltar, D. Todd, and P. Tsvetkov, *Fast Spectrum Reactors*. Springer US, 2012, ISBN: 978-1-4419-9571-1. DOI: 10.1007/978-1-4419-9572-8.

[25] J. E. Tanner, 'An overview of tritium fast fission yields', 1981.

[26] G. Hollenberg, 'Tritium release from fast neutron irradiated boron carbide', HEDL-SA-1T64-FP, 1977.

[27] A. Alemberti, M. Caramello, M. Frignani, *et al.*, 'Alfred reactor coolant system design', *Nuclear Engineering and Design*, vol. 370, p. 110 884, 2020, ISSN: 00295493. DOI: 10.1016/j.nucengdes.2020.110884.

[28] TRANSAT, *Transat project website*.

[29] F. G. Ferré, A. Mairov, D. Iadicicco, *et al.*, 'Corrosion and radiation resistant nanoceramic coatings for lead fast reactors', *Corrosion Science*, vol. 124, pp. 80–92, 2017, ISSN: 0010938X. DOI: 10.1016/j.corsci.2017.05.011.

[30] A. M. Polcaro, P. F. Ricci, and A Viola, 'The kinetics of hydrogen absorption in molten pb-li alloy', *Journal of Nuclear Materials*, vol. 119, pp. 291–295, 1983.

[31] V. D'Auria, S. Dulla, P. Ravetto, L. Savoldi, M. Utili, and R. Zanino, 'Design of a permeator-against-vacuum mock-up for the tritium extraction from pbli at low speed', *Fusion Engineering and Design*, vol. 121, pp. 198–203, Oct. 2017, ISSN: 09203796. DOI: 10.1016/j.fusengdes.2017.07.006.

[32] J. Qin, C. Hao, D. Wang, *et al.*, 'Investigation of adsorption, dissociation, and diffusion properties of hydrogen on the v (1 0 0) surface and in the bulk: A first-principles calculation', *Journal of Advanced Research*, vol. 21, pp. 25–34, Mar. 2020, ISSN: 20901232. DOI: 10.1016/j.jare.2019.09.003.

[33] P. Silvestroni, *Fondamenti di chimica*. Casa Editrice Ambrosiana, 1964.

[34] Atkins, *Atkins Physical Chemistry*. 2006.

[35] E. Serra, 'Hydrogen and tritium kinetics in fusion reactor materials', 1996.

[36] J. Crank, *The Mathematics of Diffusion*, C. Press, Ed. Oxford science publications, 1979.

[37] O. Richardson, J. Nicol, and T. Parnell, 'The diffusion of hydrogen through hot platinum', *The London, Edinburgh, and Dublin Philosophical Magazine and Journal of Science*, vol. 8, pp. 1–29, 43 1904, ISSN: 1941-5982. DOI: 10.1080/14786440409463168.

[38] I. Ali-Khan, K. Dietz, F. Waelbroeck, and P. Wienhold, 'The rate of hydrogen release out of clean metallic surfaces', *Journal of Nuclear Materials*, vol. 76-77, pp. 337–343, 1978, ISSN: 00223115. DOI: 10.1016/0022-3115(78)90167-8.

[39] P. W. Humrickhouse and B. J. Merrill, 'Vacuum permeator analysis for extraction of tritium from dcll blankets', *Fusion Science and Technology*, vol. 68, pp. 295–302, 2 2015, ISSN: 1536-1055. DOI: 10.13182/FST14-941.

[40] C. Alberghi, L. Candido, M. Utili, and M. Zucchetti, 'Development of new analytical tools for tritium transport modelling', *Fusion Engineering and Design*, vol. 177, p. 113 083, 2022, ISSN: 09203796. DOI: 10.1016/j.fusengdes.2022.113083.

[41] N Alpy, T Dufrenoy, and A Terlain, 'Hydrogen extraction from pb-17li: Tests with a packed column', 1998, pp. 787–792.

[42] A. Aiello, A. Ciampichetti, M. Utili, and G. Benamati, 'Triex facility: An experimental loop to test tritium extraction systems from lead lithium', *Fusion Engineering and Design*, vol. 82, pp. 2294–2302, 15-24 2007, ISSN: 09203796. DOI: 10.1016/j.fusengdes.2007.07.037.

[43] M. Utili, C. Alberghi, L. Candido, F. Papa, M. Tarantino, and A. Venturini, 'Triex-ii: An experimental facility for the characterization of the tritium extraction unit of the wcll blanket of iter and demo fusion reactors', *Nuclear Fusion*, vol. 62, 6 2022, ISSN: 17414326. DOI: 10.1088/1741-4326/ac5c74.

[44] M. Kinjo, S. Fukada, K. Katayama, Y. Edao, and T. Hayashi, 'Experiment on recovery of hydrogen isotopes from li17pb83 blanket by liquid-gas contact', *Fusion Science and Technology*, vol. 71, pp. 520–526, 4 2017, ISSN: 1536-1055. DOI: 10.1080/15361055.2017.1293426.

[45] I. Cristescu and M. Draghia, 'Developments on the tritium extraction and recovery system for hcpb', *Fusion Engineering and Design*, vol. 158, p. 111 558, 2020, ISSN: 09203796. DOI: 10.1016/j.fusengdes.2020.111558.

[46] R. Sherman and H. Birnbaum, 'Hydrogen permeation and diffusion in niobium', *METALLURGICAL TRANSACTIONS A*, vol. 14A, pp. 203–210, 1983.

[47] M. Yamawaki and et al., 'Surface effects on hydrogen permeation through niobium', *Journal of Nuclear Materials*, vol. 122-123, pp. 1573–1578, 1984.

[48] B. Garcinuño, D. Rapisarda, I. Fernández-Berceruelo, *et al.*, 'Design and fabrication of a permeator against vacuum prototype for small scale testing at lead-lithium facility', *Fusion Engineering and Design*, vol. 124, pp. 871–875, Nov. 2017, ISSN: 09203796. DOI: 10.1016/j.fusengdes.2017.02.060.

[49] F. Papa, M. Utili, A. Venturini, *et al.*, 'Engineering design of a permeator against vacuum mock-up with niobium membrane', *Fusion Engineering and Design*, vol. 166, p. 112 313, May 2021, ISSN: 09203796. DOI: 10.1016/j.fusengdes.2021.112313.

[50] T. F. Fuerst, C. N. Taylor, and P. W. Humrickhouse, 'The source permeator system and tritium transport in the tex pbli loop', *Fusion Science and Technology*, pp. 1–18, 2022, ISSN: 1536-1055. DOI: 10.1080/15361055.2022.2090784.

[51] B. Garcinuño and et al., 'Report of additional activities necessary to complete the commissioning phase of the pav and lipb loop', EUROfusion Internal Report BB-6.3.6-T006-D001, 2019.

[52] F. Reiter, 'Solubility and diffusivity of hydrogen isotopes in liquid pb-17li', *Fusion Engineering and Design*, vol. 14, pp. 207–211, 1991.

[53] A. Aiello, A. Ciampichetti, and G. Benamati, 'Determination of hydrogen solubility in lead lithium using sole device', *Fusion Engineering and Design*, vol. 81, pp. 639–644, 1-7 2006, ISSN: 09203796. DOI: 10.1016/j.fusengdes.2005.06.364.

[54] B. Garcinuño and D. Rapisarda, 'Report for ter technology assessment and selection in bb wcll', EUROfusion Internal Report BB-6.9-T007-D002, 2019.

[55] R. Antunes and B. Garcinuno, 'Vacuum systems for the dcll permeator against vacuum', EUROfusion Internal Report, 2N4SVT, 2016.

[56] F. Okino, J. Yagi, T. Tanaka, A. Sagara, and S. Konishi, 'Current status of the continuous tritium recovery test campaign using pbli droplets in vacuum', *Fusion Engineering and Design*, vol. 146, pp. 898–901, 2019, ISSN: 09203796. DOI: 10.1016/j.fusengdes.2019.01.108.

[57] M. Mertens, D. Demange, and L. Frances, 'Model and simulation of a vacuum sieve tray for t extraction from liquid pbli breeding blankets', *Fusion Engineering and Design*, vol. 112, pp. 541–547, 2016, ISSN: 09203796. DOI: 10.1016/j.fusengdes.2016.05.038.

[58] E. Diaz-Alvarez and L. Frances, 'Accuracy evaluation and experimental plan of the multi-nozzle vacuum sieve tray facility at the tritium laboratory karlsruhe', *Fusion Engineering and Design*, vol. 146, pp. 1954–1958, 2019, ISSN: 09203796. DOI: 10.1016/j.fusengdes.2019.03.074.

[59] B. Garcinuño, D. Rapisarda, I. Fernández-Berceruelo, E. Carella, and J. Sanz, 'The ciemat lipb loop permeation experiment', *Fusion Engineering and Design*, vol. 146, pp. 1228–1232, 2019, ISSN: 09203796. DOI: 10.1016/j.fusengdes.2019.02.045.

[60] B. Garcinuño and et al., 'Deuterium extraction from pbli on flowing free surface and through a permeation membrane – design of the test sections and adaptation of clipper', EUROfusion Internal Report BB-T.02.02-T001-D003, 2021.

[61] J.-C. Yang, T.-Y. Qi, D.-W. Ren, B.-Q. Liu, and M.-J. Ni, 'Surface waves of liquid metal film flow under the influence of spanwise magnetic field', *Fusion Engineering and Design*, vol. 130, pp. 42–47, 2018, ISSN: 09203796. DOI: 10.1016/j.fusengdes.2018.03.021.

[62] M. Utili and et al., 'Barriers vs. pbli steel corrosion and tritium permeation for wcll', $BB.WCLL - JUS - 2 - CD1 - R\&D$, $EFDA\_D\_2P46JB$, May 2020.

[63] S.-E. Wulf, N. Holstein, W. Krauss, and J. Konys, 'Influence of deposition conditions on the microstructure of al-based coatings for applications as corrosion and anti-permeation barrier', *Fusion Engineering and Design*, vol. 88, pp. 2530–2534, 9-10 2013, ISSN: 09203796. DOI: 10.1016/j.fusengdes.2013.05.060.

[64] C. Schroer and et al., 'Report on ecx development and sample qualification in 2019 and contribution to the executive summary', EUROfusion Internal Report BB-5.3.2-T003-D001, 2020.

[65] S.-E. Wulf, W. Krauss, and J. Konys, 'Long-term corrosion behavior of al-based coatings in flowing pb–15.7li, produced by electrochemical ecx process', *Nuclear Materials and Energy*, vol. 16, pp. 158–162, 2018, ISSN: 23521791. DOI: 10.1016/j.nme.2018.06.019.

[66] F. G. Ferré, M. Ormellese, F. D. Fonzo, and M. Beghi, 'Advanced al2o3 coatings for high temperature operation of steels in heavy liquid metals: A preliminary study', *Corrosion Science*, vol. 77, pp. 375–378, 2013, ISSN: 0010938X. DOI: 10.1016/j.corsci.2013.07.039.

[67] D. Iadicicco, M. Vanazzi, F. G. Ferré, *et al.*, 'Multifunctional nanoceramic coatings for future generation nuclear systems', *Fusion Engineering and Design*, vol. 146, pp. 1628–1632, 2019, ISSN: 09203796. DOI: 10.1016/j.fusengdes.2019.03.004.

[68] A. Zaborowska, Kurpaska, M. Clozel, *et al.*, 'Absolute radiation tolerance of amorphous alumina coatings at room temperature', *Ceramics International*, vol. 47, pp. 34 740–34 750, 24 2021, ISSN: 02728842. DOI: 10.1016/j.ceramint.2021.09.013.

[69] P. Muñoz, T. Hernández, I. García-Cortés, *et al.*, 'Radiation effects on deuterium permeation for pld alumina coated eurofer steel measured during 1.8mev electron irradiation', *Journal of Nuclear Materials*, vol. 512, pp. 118–125, 2018, ISSN: 00223115. DOI: 10.1016/j.jnucmat.2018.10.008.

[70] A. Venturini, F. Papa, M. Utili, and N. Forgione, 'Experimental qualification of new instrumentation for lead-lithium eutectic in ielllo facility', *Fusion Engineering and Design*, vol. 156, 2020, ISSN: 09203796. DOI: 10.1016/j.fusengdes.2020.111683.

[71] M. Utili, A. Aiello, L. Laffi, A. Malavasi, and I. Ricapito, 'Investigation on efficiency of gas liquid contactor used as tritium extraction unit for hcll-tbm pb-16li loop', *Fusion Engineering and Design*, vol. 109-111, pp. 1–6, Nov. 2016, ISSN: 09203796. DOI: 10.1016/j.fusengdes.2016.03.067.

[72] L. Candido, C. Alberghi, F. Papa, *et al.*, 'Experiments on the mhd effect on the drainage of a lipb channel and supporting numerical computations with the level set method', *Fusion Science and Technology*, vol. 77, 7-8 2021, ISSN: 19437641. DOI: 10.1080/15361055.2021.1893574.

[73] A. Ciampichetti, M. Zucchetti, I. Ricapito, M. Utili, A. Aiello, and G. Benamati, 'Performance of a hydrogen sensor in pb-16li', *Journal of Nuclear Materials*, vol. 367-370, pp. 1090–1095, 2007.

[74] L. Candido, M. Utili, M. Zucchetti, A. Ciampichetti, and P. Calderoni, 'Development of advanced hydrogen permeation sensors to measure q2 concentration in lead-lithium eutectic alloy', *Fusion Engineering and Design*, vol. 124, pp. 735–739, 2017.

[75] S. A. Steward, 'Review of hydrogen isotope permeability through materials', LAWRENCE LIVERMORE NATIONAL LABORATORY, 1983.

[76] L. Darken, *Physical Chemistry of Metals*, M. G. Hill, Ed. 1953.

[77] R. Strehlow and S. H.C., 'The permeation of hydrogen isotopes through structural metals at low pressures and through metals with oxide film barriers', *Nuclear Technology*, pp. 127–137, 1974.

[78] R. Bonifetto, M. Utili, D. Valerio, and R. Zanino, 'Conceptual design of a pav-based tritium extractor for the wcll breeding blanket of the eu demo: Effects of surface-limited vs. diffusion-limited modeling', *Fusion Engineering and Design*, vol. 167, Jun. 2021, ISSN: 09203796. DOI: 10.1016/j.fusengdes.2021.112363.

[79] J. E. Shelby, 'Molecular diffusion and solubility of hydrogen isotopes in vitreous silica', 1977, pp. 3387–3394.

[80] Y. Guo and et al., 'The effect of surface oxides and grain sizes on the deuterium permeation behavior of niobium membranes', *Fusion Engineering and Design*, vol. 149, p. 111 340, 2019.

[81] M. Pick and K. Sonnenberg, 'A model for atomic hydrogen-metal interactions - application to recycling, recombination and permeation', *Journal of Nuclear Materials*, vol. 131, pp. 208–220, 1985.

[82] A. Venturini and M. Utili, *Private communication*, 2022.

[83] R. Perry, *Perry's Chemical Engineers' Handbook*, Eight edition, D. Green, Ed. McGraw-Hill Professional Pub, 2007. DOI: 10.1021/ed019p449.2.

[84] O. Chopra and D. Smith, 'Compatibility of ferrous alloys in a forced circulation pb-17li system', *Journal of Nuclear Materials*, vol. 141-143, pp. 566–570, B 1986.

[85] R. J. Moffat, 'Describing the uncertainties in experimental results', *Experimental Thermal and Fluid Science*, vol. 1, pp. 3–17, 1988.

[86] C. Schroer, O. Wedemeyer, J. Novotny, A. Skrypnik, and J. Konys, 'Selective leaching of nickel and chromium from *Type*316 austenitic steel in oxygen-containing lead–bismuth eutectic (*LBE*)', *Corrosion Science*, vol. 84, pp. 113–124, 2014.

[87] X. Huang, B. Pang, X. Zhou, and Y. Yin, 'Experimental investigation on the cleaning effect and influence rule of hydrogen peroxide–acetic acid on lead–bismuth eutectic alloy', *Frontiers in Energy Research*, vol. 9, 2021, ISSN: 2296-598X. DOI: 10.3389/fenrg.2021.735199.

[88] C. Palomo, L.Serrano, S. Duran, *et al.*, 'Quality assurance of li-pb eutectic alloy as nuclear material qualification of commercial and r&d material ingots', *Fusion Engineering and Design*, vol. 86, pp. 2620–2623, 9-11 2011, ISSN: 09203796. DOI: 10.1016/j.fusengdes.2011.03.098.

[89] M. Utili and et al., 'Deliverable 1.6 transat project', 2022.

[90] Y. Çengel and J. Cimbala, *Fluid mechanics : fundamentals and applications*, McGraw-Hill. 2006.

[91] M. Utili, A. Tincani, L. Candido, *et al.*, 'Tritium extraction from hcll/wcll/dcll pbli bbs of demo and hcll tbs of iter', *IEEE Transactions on Plasma Science*, vol. 47, pp. 1464–1471, 2 Feb. 2019.

[92] H Feuerstein, H Grabner, J Oschinski, and S Hom, 'Compatibility of refractory metals and beryllium with molten pb-17li', 1996, pp. 1383–1386.

[93] H. Grabner, H Feuerstein, and J Oschinski, 'Compatibility of metals and alloys in liquid pb-17li at temperatures up to 650°c', *Journal of Nuclear Materials*, vol. 155-157, pp. 702–704, 1988.

[94] C. Adelhelm, D. Kempf, and E. Nold, 'Analysis of v3ti1si alloy after exposure to pb17li', *Journal of Nuclear Materials*, vol. 155-157, pp. 698–701, PART 2 Jul. 1988.

[95] H. U. Borgstedt, M. Grundmann, J. Konys, and Z. Perić, 'A vanadium alloy for the application in a liquid metal blanket of a fusion reactor', *Journal of Nuclear Materials*, vol. 155-157, pp. 690–693, PART 2 Jul. 1988, ISSN: 00223115. DOI: 10.1016/0022-3115(88)90396-0.

[96] A. Venturini, M. Utili, A. Gabriele, I. Ricapito, A. Malavasi, and N. Forgione, 'Experimental and relap5-3d results on ielllo (integrated european lead lithium loop) operation', *Fusion Engineering and Design*, vol. 123, pp. 143–147, Nov. 2017.

[97] A. Venturini, M. Utili, D. Martelli, A. Malavasi, I. Ricapito, and M. Tarantino, 'Experimental investigation on hcll-tbs in-box loca', *Fusion Engineering and Design*, vol. 146, pp. 173–177, Sep. 2019.

[98] O. I. Eliseeva, 'Formation of intermetallic layers on the surface of refractory metals in a lead melt under conditions of mass transfer', *Materials Science*, vol. 35, pp. 252–258, 2 1999.

[99] E. Paul and L. J. Swartzendruber, 'The fe-nb (iron-niobium) system', *Bulletin of Alloy Phase Diagrams*, vol. 7, pp. 248–253, 3 1986.

[100] A. Nash and P. Nash, 'The nb-ni (niobium-nickel) system', *Bulletin of Alloy Phase Diagrams*, vol. 7, pp. 124–129, 2 1986.

[101] V. Raghavan, 'Fe-nb-ni (iron-niobium-nickel)', *Journal of Phase Equilibria and Diffusion*, vol. 31, pp. 180–183, 2 2010.

[102] M. Mathon and et al., 'Calphad-type assessment of the fe-nb-ni ternary system', *CALPHAD: Computer Coupling of Phase Diagrams and Thermochemistry*, vol. 33, pp. 136–161, 2009.

[103] I. Barin and G. Platzki, *Thermochemical Data of Pure Substances*, Third ed., W. VCH, Ed. 1995.

[104] S. Mukherjee and et al., 'Thermodynamic studies on $LiNbO_3$(s) and Li_3NbO_4(s) using knudsen effusion quadrupole mass spectrometry and differential scanning calorimetry', *Journal of Alloys and Compounds*, vol. 714, pp. 681–686, 2017.

[105] R. Subasri and O. M. Sreedharan, 'Thermodynamic stability of Li_3NbO_4 by emf measurements using a novel composite electrolyte', *Solid State Ionics*, vol. 93, pp. 341–346, 1997.

[106] D. D. Wagman and et al., 'The nbs table of chemical thermodynamic properties', *Journal of Physical and Chemical Reference Data*, vol. 11, 2 1992.

[107] M. Takeyama and et al., *Phase equilibria among γ, Ni3Nb-δ and Fe2Nb-ϵ phases in Ni-Nb-Fe and Ni-Nb-Fe-Cr systems at elevated temperatures, Superalloys 718, 625, 706 and Various Derivatives*, T. T. M. M. M. S. E. A. Loria, Ed. 2001.

[108] H. Okamoto, 'Fe-v (iron-vanadium)', *Journal of Phase Equilibria and Diffusion*, vol. 27, p. 542, 2006.

[109] J. F. Smith and et al., 'The ni-v (nickel-vanadium) system', *Bulletin of Alloy Phase Diagrams*, vol. 3, pp. 342–348, 3 1982.

[110] V. Raghavan, 'Fe-ni-v (iron-nickel-vanadium)', *Journal of Phase Equilibria*, vol. 15, p. 630, 6 1994.

[111] H. Okamoto, 'Al-v (aluminum-vanadium)', *Journal of Phase Equilibria and Diffusion*, vol. 33, p. 491, 6 2012.

[112] J. F. Smith, 'The pb-v (lead-vanadium) system', *Bulletin of Alloy Phase Diagrams*, vol. 2, pp. 209–210, 2 1981.

[113] J. Konys, W. Krauss, H. Steiner, J. Novotny, and A. Skrypnik, 'Flow rate dependent corrosion behavior of eurofer steel in pb-15.7li', vol. 417, Oct. 2011, pp. 1191–1194. DOI: 10.1016/j.jnucmat.2010.12.277.

[114] H. U. Borgstedt, G. Frees, and G. Drechsler, 'Corrosion of stainless steel in flowing-pbli eutectic', *Journal of Nuclear Materials*, vol. 141-143, pp. 561–565, 1986.

[115] J. Konys and W. Krauss, 'Corrosion and precipitation effects in a forced-convection pb-15.7li loop', *Journal of Nuclear Materials*, vol. 442, 1-3 SUPPL.1 2013, ISSN: 00223115. DOI: 10.1016/j.jnucmat.2013.04.016.

[116] G. Benamati, C. Fazio, and I. Ricapito, 'Mechanical and corrosion behaviour of eurofer 97 steel exposed to pb-17li', *Journal of Nuclear Materials*, vol. 307–311, pp. 1391–1395, 2002. [Online]. Available: www.elsevier.com/locate/jnucmat.

[117] R. Mozzillo, M. Utili, A. Venturini, A. Tincani, and C. Gliss, 'Integration of lipb loops for wcll bb of european demo', *Fusion Engineering and Design*, vol. 167, p. 112 379, Jun. 2021, ISSN: 09203796. DOI: 10.1016/j.fusengdes.2021.112379.

[118] E. Carella, 'Pld/ald coating characterization in flowing pbli - ciclo – report 2021', $BB-TBM-T-02.03-T002-D002$, $EFDA\_D\_2PHBAR$, 2021.

[119] B. A. Pint and K. L. More, 'Transformation of Al_2O_3 to $LiAlO_2$ in pb-17li at 800°c', *Journal of Nuclear Materials*, vol. 376, pp. 108–113, 2008.

[120] U. Jain, A. Mukherjee, S. Sonak, S. Kumar, R. Mishra, and N. Krishnamurthy, 'Interaction of alumina with liquid $Pb83Li17$ alloy', *Fusion Engineering and Design*, vol. 89, pp. 2554–2558, 2014.

[121] H. Yukawa, G. Zhang, N. Watanabe, M. Morinaga, T. Nambu, and Y. Matsumoto, 'Analysis of hydrogen diffusion coefficient during hydrogen permeation through niobium and its alloys', *Journal of Alloys and Compounds*, vol. 476, pp. 102–106, 1-2 2009, ISSN: 09258388. DOI: 10.1016/j.jallcom.2008.08.054.

[122] E. Serra and S. Scaglione, *Private communication*, 2022.

[123] A. Venturini, S. Bassini, C. Ciantelli, *et al.*, 'Compatibility of niobium, vanadium and p22 steel in high temperature flowing lipb', *Journal of Nuclear Materials*, vol. 571, p. 153 985, 2022, ISSN: 00223115. DOI: 10.1016/j.jnucmat.2022.153985.

[124] M. Utili and et al., 'Final technical report fpa 372 sg04', 2019.

[125] M. Tarantino, M. Angiolini, S. Bassini, *et al.*, 'Overview on lead-cooled fast reactor design and related technologies development in enea', *Energies*, vol. 14, p. 5157, 16 2021, ISSN: 1996-1073. DOI: 10.3390/en14165157.

[126] B. Paladino and et al., 'Optimisation of antipermeation and anticorrosion barrier – final report', EUROfusion Internal Deliverable BB-5.3.1 -T003-D002, 2020.

[127] J. R. Taylor, *An Introduction to Error Analysis - The study of uncertainties in phisical measurements*, Second Edition. 1939.

Appendix

Error Analysis

The error analysis evaluates the uncertainty in measurement and performing it is crucially important to have a reliable estimate of physical quantities needed to characterize components and technologies.

In this thesis, the error analysis follows the rules reported in [127].

In general, the errors are divided in fixed errors and variable errors. The fixed errors are constant during the acquisition, while the variable errors oscillate. In the experimental campaigns performed in this thesis, it was decided to consider the errors related to:

- the accuracy of the instrument (taken from the manufacturer's specifications – fixed error);
- the error of the signal chain (evaluated before the experiments during the quality control – fixed error);
- the oscillations of the value measured by the instrument (due to the precision of the instrument – variable error);
- the small physical variations of the measured quantities (e.g., the temperatures were not perfectly constant during each experiment – variable error).

The standard deviation accounts for the last two errors together. This procedure has been performed on every instrument and for each test.

The standard deviation of the data collected in each test was calculated as:

$$S = \sqrt{\frac{1}{N-1}\sum_{i=1}^{N}|x_i - \bar{x}_{exp}|^2} \tag{9.1}$$

where x_i is the measured value, N is the number of data collected during one test and $\bar{x}_{exp}$ is

$$\bar{x}_{exp} = \frac{1}{N}\sum_{i=1}^{N} x_i \tag{9.2}$$

Then, following the error propagation theory, the total measuring system error was calculated as:

$$\epsilon = \sqrt{\epsilon_{ch}^2 + \epsilon_{acc}^2 + S^2} \tag{9.3}$$

where ϵ_{ch}^2 is the error of the signal chain and ϵ_{acc}^2 is the error related to the accuracy of the instrument, which was evaluated as:

- the product of the accuracy and of the FSO (Full Scale Output) for those instruments with the accuracy expressed as a percentage of the FSO;
- the product of the accuracy and of the measured value (divided by 100) when the accuracy was expressed as a percentage of the reading;
- just the accuracy (only in the case of the Thermal Mass Flow Meter).

The measuring error of thermocouples is separately discussed, as their accuracy varies with temperature and an additional source of error has to be taken into account: the error associated to the calibration instrument (GE DPI 620 Genii). Type K thermocouples have a declared accuracy of:

- $\pm 1.5\,^{\circ}\mathrm{C}$ from $-40\,^{\circ}\mathrm{C}$ a $375\,^{\circ}\mathrm{C}$;
- $\pm 0.004 \cdot T$ [°C] above $375\,^{\circ}\mathrm{C}$.